Robots with a Twist: Torque Responsive Metamaterials Enable Efficient Energy and Force Transduction

Ian Good

A dissertation
submitted in partial fulfillment of the
requirements for the degree of

Doctor of Philosophy

University of Washington

2024

Reading Committee:
Aniruddh Vashisth, Chair
Jeffery Ian Lipton, Chair
Xu Chen

Program Authorized to Offer Degree:
Mechanical Engineering

University of Washington

Abstract

Robots with a Twist: Torque Responsive Metamaterials Enable Efficient Energy and Force Transduction

Ian Good

Co-Chairs of the Supervisory Committee:
Aniruddh Vashisth
Mechanical Engineering

Jeffery Ian Lipton
Industrial and Mechanical Engineering, Northeastern University

This thesis demonstrates how the use of Torque Responsive Metamaterials mapped from design space to realized performance spaces allows us to overcome large challenges in legged robots, soft grasping, and soft robotic arms. We first establish and dramatically expand a mapping from design space to a realized performance space for our HSA actuators. Then use multi-modal properties enabled by HSAs to create multi-functionality in a robot leg through capstan breaking and the visco-dynamic properties of the HSA. In grasping, we design a complimentary Torsionally Rigid Strain Limiting Layer (TR-SLL) to dramatically increase payloads of soft grasps to over 5kg. When then combine the TR-SLL with a HSA based gripper, enabling HSAs gripers to be created as a single finger. By adding the HSA, We further enhance grasp performance by using the torque responsive nature to increase payload capacity. Finally, we combine HSAs with Bendable Extendable Torsionally Rigid Shafts (BETRs) to create a soft robot arm capable of lifting a YCB mustard bottle at more than half a meter and push over 2kg vertically while supporting its own weight under gravity.

TABLE OF CONTENTS

LIST OF FIGURES

ACKNOWLEDGMENTS

My sincere appreciation to Applied Physics Laboratory - University of Washington and my team for funding, support, and community. Steve Kahle, thank you for your mentorship, advice, and dedication. You are an exceptional boss and leader. The world would be well served to have more people like you. I'd also like to thank the Office of Naval Research, specifically Dr. Daniel Deitz, for finding, supporting, and investing in tomorrow's leaders.

I'd like to thank my advisors for their continued support, mentorship, and guidance. I'd like to thank the amazing members of the Transformative Robotics Lab and Vashisth Research Lab for their shoulders to lean on when challenges arose, and for their cheers in victory as we celebrated success. Many thanks to the chair of the department, Alberto Aliseda, for deeply caring about student outcomes and for his help in my journey. I'd also like to thank the many wonderful staff in the department, Wanwisa, Kendra, Bill, Corey, and Lily, thank you for all your help over the years.

Outside of work, I'd like to thank my parents, Jan and John Good, for their infinite support and encouragement. My partner, Angela Straccia, for lifting me up when I am down and making this journey a whole lot easier. And my family for their encouragement, support, and confidence. Finally, I'd like to thank my friends for their support, fun birthday BBQs, and the community they have provided. You all provide the meaning for my journey.

DEDICATION

To building community, for it is the most powerful thing a mechanical engineer can create.

Chapter 1
INTRODUCTION

1.1 Overview

The mapping of design space to realized energy landscapes is critical for performant robots. This thesis maps this concept to three key areas of robotics: Legged robots, soft grasping, and soft robot arms. Legged robots have a power problem.Biological systems are far more multi-functional and efficient than COTS hardware. Soft grasping struggles to support payloads beyond a strawberry when not lifting parallel to gravity. Soft robotic arms have similar challenges. Soft arms struggle to support their own weight and are fixed to a top-down configuration. To solve these large challenges, we look to the field of torque responsive metamaterials. Here, Handed Shearing Auxetics (HSA) have cemented themselves as an extremely useful actuator. They couple rotation with extension in a distributed compliant body. This allows them to leverage the development in electric motor technology and controls while still providing the distributed compliance and safety of a soft robot.

1.2 Materials Define Robots

Materials play a crucial role in the performance and functionality of robots, influencing their structural integrity, durability, and adaptability to various environments. In traditional robotics, materials such as metals and rigid plastics are often used due to their strength and reliability. These materials ensure that robots can perform repetitive tasks with high precision and withstand significant wear and tear, making them suitable for industrial applications. For instance, in the design of robotic arms used in manufacturing, materials like steel and aluminum provide the necessary rigidity and load-bearing capacity to handle heavy objects and execute precise movements [166].

The advent of soft robotics has shifted the focus towards more flexible and compliant materials, which offer advantages in applications requiring delicate interactions and adaptability. Soft materials, such as silicone, hydrogels, and shape-memory alloys, enable robots to mimic the properties of biological tissues, allowing them to safely interact with humans and manipulate fragile objects [79, 103, 124]. The ability to conform to complex shapes and absorb impacts is critical. For example, researchers have demonstrated that soft robotic grippers can handle a wide variety of objects with different shapes and textures without causing damage [56, 98, 140].

Moreover, the choice of materials directly impacts the energy efficiency and operational range of robots. Lightweight and flexible materials can reduce the energy consumption of robotic systems by minimizing the force required for movement and actuation. This is particularly important in mobile and wearable robotics, where battery life and portability are key concerns. Advances in material science, such as the development of conductive polymers and lightweight composites, have opened new avenues for creating energy-efficient and highly functional robotic systems. [50, 153, 156] Additionally, much work has been done on embodied intelligence and mechanical intelligence where the physical structure of the robot is incorporated into its controls and logic [121, 163, 192].

1.2.1 Grasp Modes from Hard to Soft

In this section we will cover the benefits of grasping modes based on the underlying material the gripper is made from. While grasping in and of itself is not the whole of this thesis, insights from grasping maps well into the spaces of legged robotics and robotic arms. Direct drive robotic grasping systems are characterized by the direct connection of actuators to the end effectors, eliminating the need for transmission mechanisms such as gears or belts. This setup allows for high precision and responsiveness, making it ideal for applications requiring fine manipulation and high-speed operations. Direct drive systems benefit from reduced backlash and increased control accuracy, which are crucial for tasks involving precision. Research by Ma and Dollar [117] explores how direct drive designs enable improved

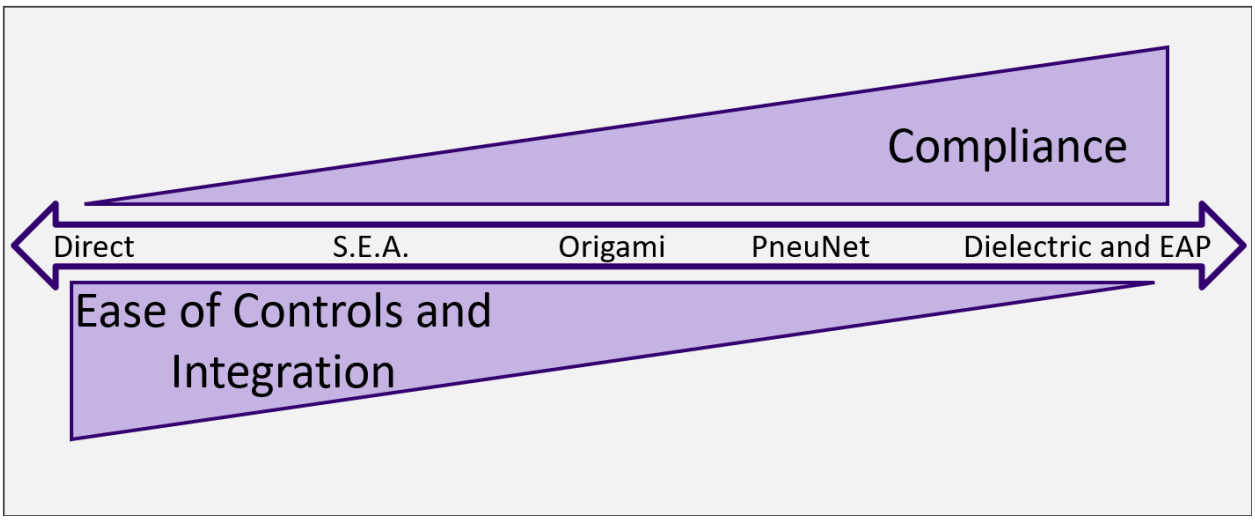

Figure 1.1: Here we broadly characterize the effects of the underlying material's impact on grasping. Direct drive gripper are well understood, have robust controls, and are easy to integrate into existing robotic systems. On the other end of the spectrum, DEA or chemical based grippers offer significant compliance benefits but come with non-trivial controls and integration overhead.

grasping performance in robotic hands. Similarly, Bhatia et al. [12] highlight the efficiency and precision of direct drive actuators in robotic manipulators, emphasizing their capability in tasks that demand quick and accurate responses. Series elastic actuators (SEAs) incorporate elastic components between the motor and the load, which allows for better force control and shock absorption, enhancing the robot's ability to interact safely with its environment. SEAs are particularly useful in applications that require compliance and adaptability, such as human-robot interaction and unstructured environments. Pratt and Williamson's work on SEAs demonstrated their potential in achieving high-fidelity force control while maintaining safety during physical interactions [141]. Another important contribution by Robinson et al. discusses the implementation of SEAs in robotic arms, highlighting their benefits in reducing the impact forces during collisions [148]. Vanderborght et al. [186] reviewed various applications of SEAs, underlining their significance in enhancing the adaptability and resilience of robotic systems in dynamic and uncertain environments.

Origami-inspired robotic grasping systems leverage the principles of folding structures to create compliant and adaptive grippers. These systems can change shape and stiffness, allowing for versatile and efficient grasping of objects with varying geometries and sizes. The work by Onal and Rus illustrates the potential of origami structures in creating flexible and lightweight robotic grippers [134] . Felton et al. developed an origami-inspired robotic hand capable of dexterous manipulation, demonstrating its effectiveness in handling delicate and irregularly shaped objects [60]. Additionally, Hawkes et al. explored the use of origami techniques to design reconfigurable robotic grippers, highlighting their advantages in achieving both precision and adaptability in grasping tasks [71].

Pneumatic network actuators (Pneunets) employ interconnected air chambers that can be inflated or deflated to produce motion, providing soft and adaptive grasping capabilities. Pneunets are particularly advantageous in applications requiring gentle handling and adaptability to various object shapes. Polygerinos et al. [139] demonstrated the use of Pneunets in soft robotic grippers, showcasing their ability to grasp and manipulate a wide range of objects without causing damage. Another significant study by Ilievski et al. developed a soft

robotic hand using Pneunets, highlighting its capability in performing complex manipulation tasks [83]. Additionally, Mosadegh et al. [124] introduced advanced designs of Pneunets for robotic grippers, emphasizing their potential in achieving precise and adaptive grasping through simple and scalable fabrication techniques. Usevitch also demonstrated pneumatic grasping in the form of a large scale untethered robot, showing significant compliance and safety [185].

Dielectric elastomer actuators (DEAs) are a type of electroactive polymer that can deform in response to an electric field, offering lightweight and compliant actuation for robotic grasping. DEAs provide advantages in terms of high energy density and fast response times, making them suitable for applications requiring dynamic and adaptable grasping. Keplinger et al. [96] explored the use of DEAs in soft robotic hands, demonstrating their effectiveness in achieving flexible and efficient grasping. Another key contribution by Rosset and Shea [151] reviewed the advancements in DEA technology for soft robotics, highlighting their significant role in enhancing the performance and versatility of robotic graspers.

Electroactive polymers (EAPs) can change shape or size when stimulated by an electric field, making them ideal for creating flexible and adaptive robotic grippers. EAP-based systems offer benefits such as low weight, high compliance, and the ability to produce complex motions. Bar-Cohen [8] provided a comprehensive overview of EAP applications in robotics, emphasizing their potential in creating innovative grasping mechanisms. Another important study by Richardson et al. [146] demonstrated the use of ionic polymer-metal composites in robotic grippers, highlighting their ability to achieve precise and adaptive grasping. Moreover, Shintake et al. [164] reviewed the integration of EAPs in soft robotic grippers, showcasing their advantages in terms of adaptability and compliance in various grasping tasks.

Handed Shearing Auxetics (HSA) by Lipton et al. are a chiral structural metamaterial [111]. HSAs are structures characterized by a negative Poisson's ratio, meaning they expand perpendicularly when stretched. This unique property allows these materials to convert rotational motion into linear motion efficiently. HSA unit cells projected onto the plane

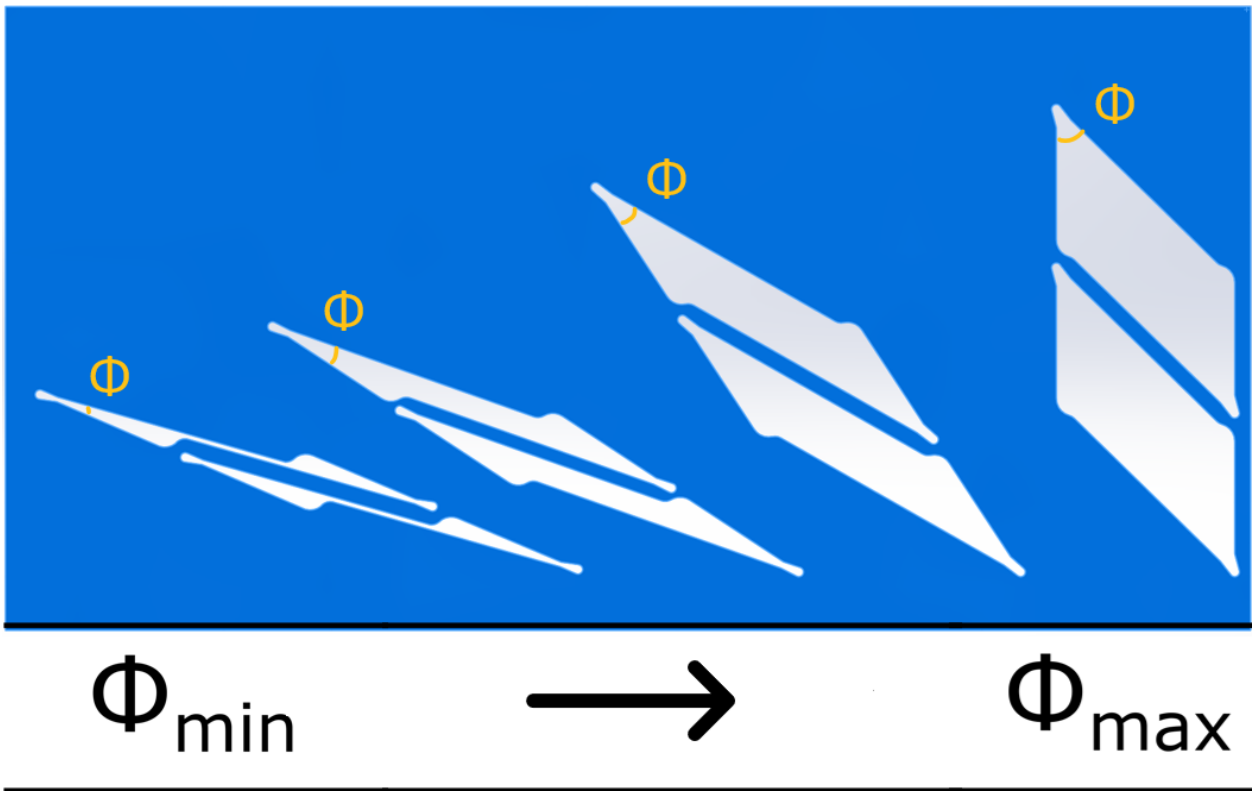

Figure 1.2: Here demonstrate the projected Auxetic Trajectory for a compliant HSA unit cell to the plane. As theta increases, the unit cell expands. Large changes is height are seen given an input shear in the early region of the auxetic trajectory. As the trajectory progresses, there is much less vertical extension, resulting in a much larger force output.

can be seen in Fig.1.2 where ϕ tracks the auxetic trajectory from ϕ_{min} to ϕ_{max} through 0%,15%,50%,100%. Since the seminal work, broader characterization has been done on HSAs. Truby et al. [183] created a method of printing HSAs from a photo and thermal curing polymer while Good et al. [63] expanded the design space by introducing printing HSAs at different points along their auxetic trajectory. Kaarthik et al. and Kim et al. [90] and [99] further expanded the material space by creating small HSAs out of photocure polymers and single HSA extendable systems from TPU respectfully.

The nature of HSAs torque activation makes them functionally similar to direct drive and series elastic actuators [111]. Direct drive systems benefit from precise control due to the lack of intermediary transmission mechanisms, and HSAs achieve similar functionality by directly applying torques to the material to manipulate its deformation. This enables the creation of grippers that can delicately handle objects with high precision, fast response times, and through cheap and efficient methods. It also enables the use of well matured electric motor technology and control algorithms. Furthermore, like series elastic actuators, oragami, and pneunet grippers, HSAs' inherent material properties allow for a controlled response to applied forces, thus combining the best attributes of both compliance and control.

1.2.2 Projecting HSAs to DH Parameters

Kinematic chains in robotic arms are a sequence of rigid bodies connected by joints, allowing the system to achieve complex motion and manipulation tasks. Each link in the chain contributes to the overall movement, and precision in each joint is critical to ensure accurate end-effector positioning. However, tolerance stackup, which refers to the accumulation of small manufacturing errors at each joint, can significantly affect the robot's performance. Even minor deviations in the fabrication or assembly of each joint can lead to large errors in the position and orientation of the end-effector. As a result, maintaining high precision and minimizing tolerance stackup are essential challenges in the design and manufacturing of traditional robotic arms. By designing robots with soft components, we give up some precision in knowing our positioning, but gain compliance, relaxing the constraints on robot

pose, and making certain tasks easier like peg in hole insertions.

Because HSA robotic systems can be driven by traditional motors, it is helpful to think of HSAs in terms of traditional robotic modelling. Denavit-Hartenberg (DH) parameters are a standardized method used to model the kinematics of robotic arms. This approach simplifies the representation of the spatial relationships between adjacent links by defining four parameters: link length, link twist, link offset, and joint angle and two mechanisms: prismatic and revolute joints. By using DH parameters, one can systematically derive the transformation matrices that describe the position and orientation of each link relative to its predecessor [43, 52]. This method is widely used due to its ability to streamline the complex calculations involved in robotic kinematics, making it easier to analyze and design robotic systems. The DH convention has been foundational in the development of many robotic applications, providing a consistent framework for understanding and implementing the movement of robotic arms [5].

HSAs when combined with something to resist torque, can create prismatic joints. That could be another HSA of opposite chirality, a torsionally rigid mechanism, or a metamaterial [30,39,99,180]. In particular, the work by Carton, Thomas, and Kim et al. are all of interest as they can be used to create a revolute joint if a torque is applied to the mechanism. This gives both types of linkage required to create a DH parameter robot. Of these, the work of Thomas in creating the Bendable Extendable Torsionally Rigid Shaft (BETR) is used in this thesis as it is easier to manufacture than the point group auxetics and performs better than the bellows system demonstrated in Kim et al.

1.2.3 Applications of Torque Responsive Metamaterials

In this section we look to the exciting application spaces that torque responsive metamaterials have been used through the rest of the chapters of this thesis.

In chapter two, we look to expand the design space of HSAs. This chapter overcome limitations in previous HSA designs, particularly in terms of actuation range, blocked force, and stiffness. The chapter is concentrated on two key parameters: the preferred manufac-

turing point along an HSA's auxetic trajectory and the number of cells in the HSA. By modeling HSAs as programmable springs,the chapter investigates the impacts of these parameters on the actuators' performance metrics such as blocked force, spring constant, angle range, and holding torque. Since this chapter is about characterization, methodologies play a large role. The chapter presents methodology for fabricating HSAs using advanced 3D printing techniques and conducting mechanical testing to measure performance. Different HSA configurations were created by varying the preferred auxetic trajectory points and the number of cells. We found that changing the auxetic trajectory point allowed them to create actuators capable of pushing, pulling, or both. This chapter significantly expanded the range of forces (from 5 N to 150 N) and stiffness (from 2 N/mm to 89 N/mm) achievable with HSA actuators. The results showed that reducing the length of the HSAs increased the force output but required higher torques and resulted in shorter extension ranges. Additionally, the study highlighted the effects of viscoelasticity, noting that the force a 3D-printed HSA could apply decreases over time due to stress relaxation.

In chapter three, HSAs are used as viscoelastic element to provide multi modality to a robotic leg.

In chapter four, a Torsionally Rigid Strain Limiting Layer (TR-SLL) is presented as a way of improving the payload capacity of anti-podal Pneu-net based grippers. The chapter addresses a significant challenge in the field of soft robotics: the limited ability of Pneu-net actuators to handle large payloads perpendicular to the gravity field due to out-of-plane deformations. These deformations often lead to objects slipping out of grasp and reduced control over object positioning. The TR-SLL enhances the torsional rigidity of Pneu-net actuators without compromising their inherent softness and flexibility. The chapter presents a study, both in simulation and through experimental validation, to map the design space of the TR-SLL. It focused on the impact of varying the number of triangular cells in the TR-SLL as well as the beam thickness. The findings revealed that the TR-SLL significantly reduces out-of-plane bending—up to 97.7% compared to a benchmark Pneu-net gripper from the soft robotics toolkit. This improvement was demonstrated by the TR-SLL gripper's

ability to lift a 5kg payload, far surpassing the capabilities of a traditional Pneu-net gripper. Additionally, the TR-SLL gripper demonstrated a peak grip force of 3N and a stiffness of 1200N/m, compared to 1N and 150N/m for the benchmark Pneu-net. The chapter presents tests on a suite of objects from the YCB object set, which are beyond the payload capacity of traditional Pneu-nets. The TR-SLL gripper successfully lifted five out of six selected objects, showcasing its enhanced capabilities. The improved performance is attributed to the TR-SLL's ability to maintain higher normal forces and increased torsional stiffness, which mitigates the common failure modes of slipping, twisting, and shearing in soft grippers.

In chapter five, TR-SLLs are combined with HSAs to further extend HSA gripper performance. The TR-SLL is able to easily resist torques induced by the HSA while also proving a flat gripping surface. The inclusion of the HSA with the TR-SLL imparts some torque loading into the TR-SLL, resulting in a scooping motion. Through careful design choice, the torque load from the HSA extending to grab the object can be used to increase the payload capacity of the TR-SLL further. The chapter presents a larger study on the design and performance of the TR-SLL. Further characterization is shown through simulation and experimental validation. Triangluar cell count over the span, beam thickness, and HSA property spaces were explored. This chapter expands the suite of YCB objects to 43 objects. The TR-SLL HSA gripper successfully lifted 37 out of the 43 objects, showcasing its enhanced capabilities. The increased performance is attributed to the TR-SLL's ability to maintain higher normal forces and increased torsional stiffness, mitigating common failure modes such as slipping, twisting, and shearing in soft grippers. This chapter demonstrates peak pinch grasp forces of more than 5N and planar caging grasp forces in excess of 14N, far exceeding the state of the art of pure HSA grasping.

In chapter six, the authors present a torque responsive metamaterial robot made from HSAs and BETRs.

Chapter 2

EXPANDING THE DESIGN SPACE FOR ELECTRICALLY-DRIVEN SOFT ROBOTS THROUGH HANDED SHEARING AUXETICS

2.1 Summary

Handed Shearing Auxetics (HSA) are a promising structure for making electrically driven robots with distributed compliance that convert a motors rotation and torque into extension and force. These structures expand and contract by changing an internal angle between links, the evolution of the structure as this angle changes is known as the auxetic trajectory. We seek to expand the design space of HSA actuators and to understand the effects of design parameters on HSA performance. Past work on understanding their design space has focused on variations in a few parameters on the original HSA design but has not provided significantly expanded the range of actuation, blocked force, and stiffness possible or the characterization requirements for motor selection. We overcome past limitations on the range of actuation, blocked force, and stiffness by focusing on two key design parameters: the point of an HSA's auxetic trajectory that is energetically preferred, and the number of cells along the HSAs length. Modeling the HSA as a programmable spring, we characterize the effect of both on blocked force, minimum energy length, spring constant, angle range and holding torque. We also examined the effect viscoelasticity has on actuation forces over time. By varying the preferred auxetic trajectory point, we were able to make actuators that can push, pull, or do both. We expanded the range of forces possible from 5 N to 150 N, and the range of stiffness from 2 N/mm to 89 N/mm. For a fixed point on the auxetic trajectory, we found decreasing length can improve force output, at the expense of needing higher torques, and having a shorter throw. We also found that the viscoelastic effects can

limit the amount of force a 3D printed HSA can apply over time.

2.2 Introduction

For soft robots to find wide-scale utility they must leverage previous and ongoing developments in electrical power sources, compute, and motors. Fluid-flow driven robots have proliferated, but they must be entirely fluid based [54, 80, 192], or rely on slow, rigid, and inefficient hardware to interface with electrical systems [39]. While a significant amount of effort has gone into self healing and puncture resistant fluid-driven robots [120, 178], their nature leaves them susceptible to cascading failure.

Efforts in building electrically-driven soft robots have either focused on novel responsive materials [2, 73, 110, 122] or cable driven systems [4, 11, 167]. Dielectric actuators can quickly, efficiently and directly respond to electrical stimuli but require high voltages, limiting adoption. Thermal responsive materials like liquid crystal elastomers can be programmed to generate complex shape transformations [19, 105] and phase change materials [110] can generate large forces. While promising, these thermoelectric materials are often slow to cycle and inefficient. Another alternative has been to rely on motors in soft robots. The primary method has been twisted pair [4] or cable driven [10, 11, 123, 167] robots. While these have been successfully used as arms [11], grippers [123, 167], and locomotive robots [10], these drives can only pull, and must rely on the structure itself to generate a restorative force.

Recent developments in auxetic metamaterials allows compliant structures to directly convert the rotation and torque from a motor into linear translation [111], bending [39, 41] or volumetric expansion [109]. Handed Shearing Auxetic (HSA) materials have been used to make robot arm sections [111] and grippers [38–41]. They can be lasercut from PTFE tubes [39,41], assembled from spring steel strips [111], or 3D printed out a variety of polymers [183].

HSA actuators consist of shearing auxetic cells tiled onto a cylinder [111]. These cells couple shear with expansion through a change in an angle between links called ϕ. The state of this cell is a function of this internal angle. The evolution of the structure relative to this angle defines a trajectory of cell state call the auxetic trajectory [111]. By tiling the cells

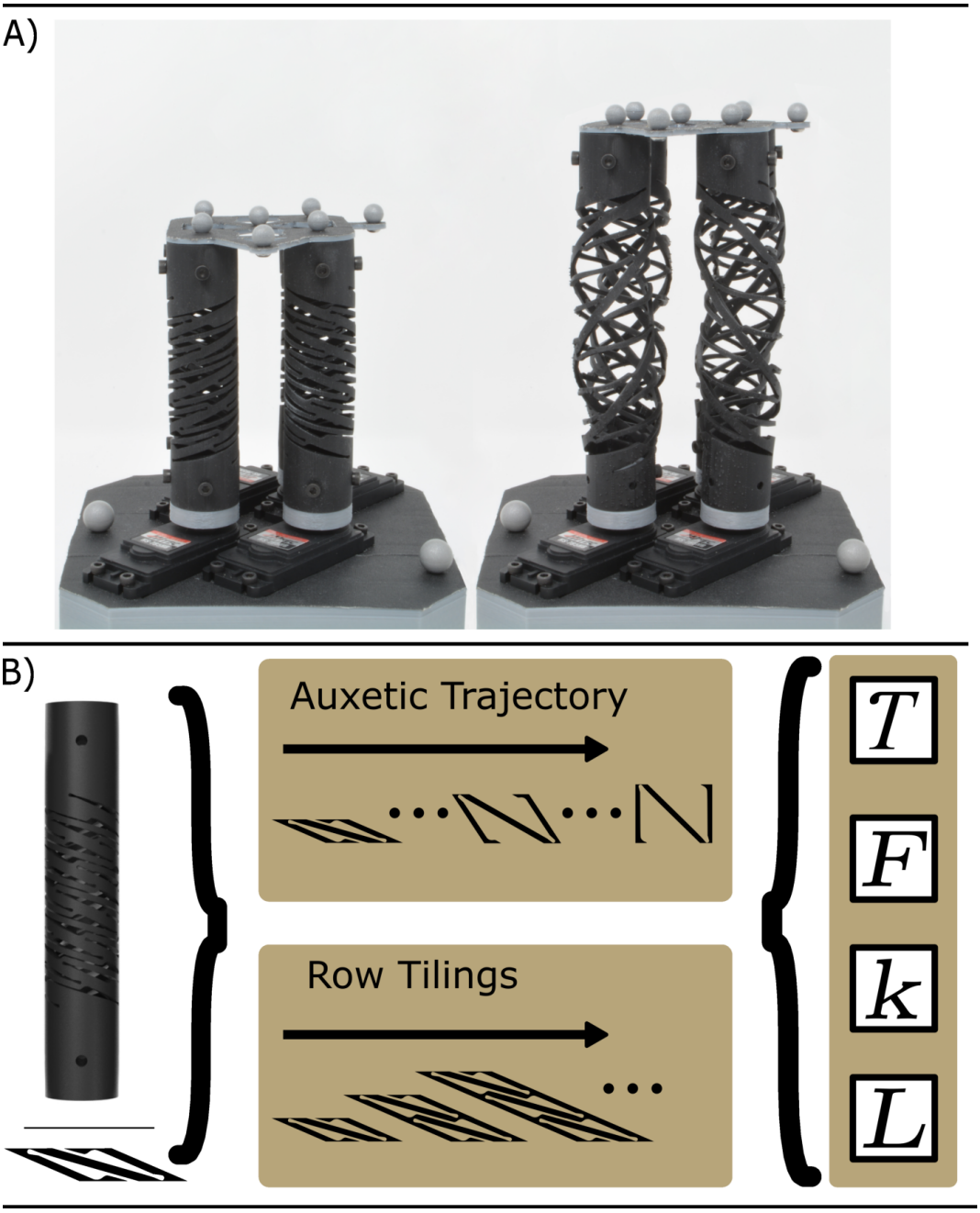

Figure 2.1: HSAs convert rotation into compliant length changes enabling soft robots such as (A) A 4-DoF platform. (B) By varying the structure of the HSA in terms of its cell rest state and the number of cells, we can effect torque (τ), blocked force (F), the spring constant (k) and minimum energy length (L)

on the cylinder, the shear-extension coupling of the cell is converted into a torsion extension coupling in the structure. This can be seen in Fig.B.1A, where motors at the bottom of the HSAs are rotated in unison to lift the platform. Fig. 2.2 shows three different point along the HSAs auextic trajectory at ϕ_{min}, ϕ_j, and ϕ_{max}. When an HSA is made, a point of the trajectory is converted into a structure for fabrication per Fig.2.2C. These are not different states of the same HSA, but rather are three different HSAs designed at unique points along the auxetic trajectory.

All work until today has focused on the initial HSA design, which is at a maximally closed state ϕ_{min} [38–40, 183]. This actuator can be twisted to extend, but due to its closed state design, cannot be twisted to generate pull forces. Characterization of this design has focused on the effect of cell size, base materials, diameter and wall thickness on performance metrics such a blocked force, extension, and grip strength [183]. The upper limit of blocked force and spring constant found by previous work reached 5N and 2N/mm respectfully. While useful, it has not provided enough information to select a motor for an HSA actuator, nor has it solved the fundamental limitations of the original design.

For HSAs to become more widely used in robotics we need to understand how to design an HSA and pair it with a motor to make an actuator and move beyond push-only actuation. To that end we have analyzed the effect of two overlooked design parameters on HSAs. Specifically we focused on the point of the auxetic trajectory used as the base state and the number of rows stacked vertically along the actuator and their effect on key design variables (Fig.B.1B). By varying the point along the auxetic trajectory used to make the structure, we find that we can generate purely contractile actuators, purely expanding actuators, and actuators that expand and contract. We model the HSA as a spring of variable stiffness(K) and minimum energy length(L) that is driven by the twist angle of the base. Because the spring changes stiffness and length as a function of rotation, the HSA can generate a blocked forced (F) through rotation. We determined the holding torque(T) and angle range for an HSA as a function of cell number and trajectory point, enabling servo selection. We found that the materials these structures were made from also contributed significantly to actuator

performance and found that stress-relaxation could limit the time scale of force application.

In this paper we:

- Model to key metrics needed for motor selection with HSA structures
- Expanded the force range of HSA actuators to include contraction
- Characterize the effect of the auxetic trajectory point selection, and vertical cell count on actuator performance
- Evaluate the effect of stress relaxation on force application by HSA actuators

2.3 Methods

Handed Shearing Auxetics were originally designed as an idealized kinematic linkage structure of tessellated cells on a plane or cylinder [111]. In this framework the structure has a zero-energy mode of deformation, meaning it changing state requires no energy and there is no restorative force to return to the original state. The zero energy mode of deformation defines the auxetic trajectory [111] (Fig.2.2A) The idealized model has no preferred point along the trajectory; however, when the model is fabricated using living hinges, the zero-energy mode of deformation is replaced with a deformation mode with a shallow-gradient, where energy is required to transition between states of the cells. The first and all subsequent soft robotic HSA structures were optimized for compactness in order to maximize the expansion of the structure [39, 111, 183]. This biased the device to be at the most closed point possible ϕ_{min} and caused the structure to be a push-only actuator.

To explore the effect of biasing the HSA we selected three points along the auxetic trajectory for testing as seen in Figure 2.2C. The closed state is the same as past HSAs ϕ_{min}. The open state represents the maximum point along the auxetic trajectory ϕ_{max}, further evolution of ϕ beyond this point result in non-auxetic deformations of the cell and is out of scope for this paper. We then chose a point midway between the closed state and the open state and refer to it as the semi-open state.

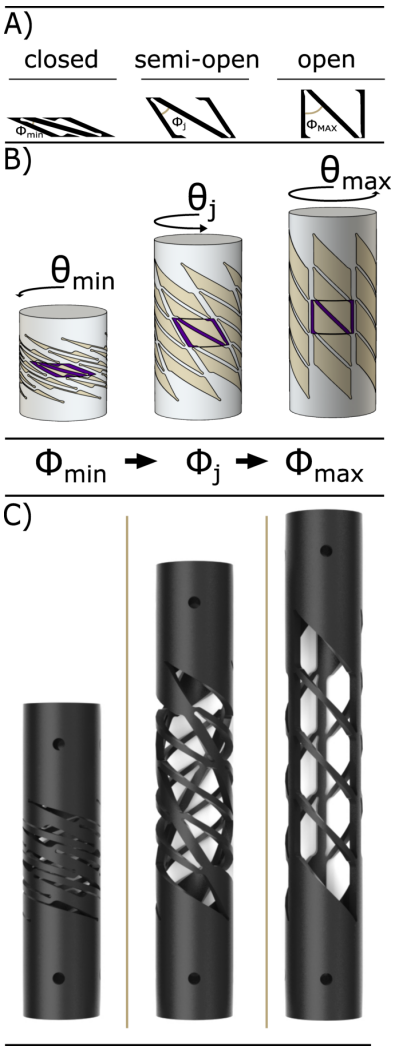

Figure 2.2: The Auxetic Trajectory for an Handed Shearing Auxetic (HSA) pattern. HSAs tile a 2D unit cell (A) around and along a cylinder. Row tilings represent the number of vertically stacked unit cells and collumns represent the number of horizontally stacked unit cells. As an internal angle ϕ between links of the cell increases the cell expands and shears, driving a rotation and expansion of the cylinder (B). A rotation of one end of the cylinder (θ) can also drive an expansion of the cell and cylinder. The evolution of the system with respect to ϕ is the auxetic trajectory. Different instantiations of the auxetic trajectory can then be manufactured and used in soft robotic applications(C).

Past work on characterizing HSAs focused on taking a structure of fixed length and shrinking the size of the cell, to increase the number of cells circumstantially and vertically. What remains unknown is how changing the length with the same size cell effects stiffness. HSAs can be viewed as programmable springs, where the change in angle changes the stiffness of the structures. For regular springs the relationship between length and spring constant is an inverse relationship set by the number of windings. It is unclear how a change in spring constant as a function of θ is effected by the number of stacked unit cells, because the number of windings remains constant.

2.3.1 Mechanical Characterization

HSA Manufacturing

All HSAs tested were rapidly manufactured using digital projection lithography on a Carbon M1 3D Printer using Carbon FPU50. All closed trajectory HSAs were printed horizontally with the semi-open and open HSAs being printed at a 20 degree angle to improve print quality. All parts were handled, cleaned, and cured following the manufacturers specifications. Unless otherwise specified all HSAs in this paper were designed with a 19mm outer diameter and a 2mm wall thickness.

Mechanical Testing Setup

All data was gathered from an Instron 68SC-2 at 50Hz with a combined force and torque cell. The samples were rigidly connected to the Instron by inserting a cap into both ends and placing a metal rod through the HSA and the cap using the holes seen in Fig.2.3.

Auxetic Trajectory Testing

The testing procedures for Auxetic Trajectory HSA configurations were defined by manually observing the practical range of rotation and extension for each configuration. All samples tested are left handed which means that a clockwise rotation will shorten the structure.

Figure 2.3: Five instantiations of closed left-handed HSAs with varying row tilings from four to twelve. These are made by vertically stacking the closed pattern around a unit cell.

Table 2.1: Testing procedures for the Auxetic Trajectory subcategory of HSAs. Positive degree values represent Counter-Clockwise rotation and negative degree values represent Clockwise rotation. All test rates are 20 mm/s

HSA Type	**Starting Angle**	**Ending Angle**	**Angle step size**	**Printed Length**	**Cycling Range**
Closed	0 degrees	90 degrees	30 degrees	75 mm	0 to 20.0 mm
Semi-Open	-90 degrees	90 degrees	30 degrees	109 mm	-3.4 to 6.6 mm
Open	-180 degrees	0 degrees	30 degrees	122.2 mm	-3.4 to 0 mm

For each of the structures, there was a difference between the printed length and the actual resting state of the structure. The difference between the minimum energy length and the printed length we call the zero force displacement. To determine the displacement for the the 4-row closed HSA, we inserted the HSA and manually jogged the Instron to a displacement where the force reading was zero. For this configuration, the zero force displacement was 2.7 mm.

For the semi-open structure we measured the force displacement curve of the HSA. The lower displacement limit for the semi-open configuration was defined as the displacement necessary to have a minimum force reading at a rotation of 90 degrees clockwise. The upper limit is defined as half the resting height of the open HSA configuration (6.6 mm). The relationship between rotation and zero force displacement is linear in this region. We used the interception of the curve with zero to find the zero force displacement and found it was 1.1 mm.

The lower displacement limit for the open configuration was defined as the displacement necessary to have a minimum force reading at a rotation of 180 degrees clockwise. The upper limit was defined as the printed length of the open HSA. For this configuration, the zero force displacement was 0.6mm. The zero force displacement was obtained by dividing the lower displacement limit by the number of rotation steps needed to return to the resting

state.

To determine the spring constant for the semi-open and open HSAs for a given θ, we conducted an extension test of 4.0mm and 0.5mm from the minimum energy length (L). Force and displacement were measured and the slope used to determine the spring constant.

Row Test Parameters

All HSAs in this subcategory vary the number of closed unit cells row tilings from four to twelve. The testing procedures were obtained in the same way as the 4-row closed HSA configuration. The zero-force displacement was found by manually jogging and rotating the HSA to find the minimum force. The average difference in displacement between steps is defined as the zero-force displacement. For future HSAs, the practical cycling range and zero force displacement can be estimated from the trends from this work.

Table 2.2: Testing procedures for HSAs of different row amounts. All test rates are 20 mm/s

Number of Rows	**Printed Length**	**Cycling Range**	**Zero Force Displacement**
4	75 mm	0 to 20.0 mm	2.7 mm
6	89 mm	0 to 19.4 mm	3.6 mm
8	100 mm	0 to 31.7 mm	3.5 mm
10	112 mm	0 to 41.8 mm	3.5 mm
12	124 mm	0 to 60.0 mm	3.8 mm

2.3.2 Measured and Derived Properties

In this paper, we characterize four main properties for the HSAs tested as shown in Fig. B.1B: blocked force (F_b), minimum energy length (L), holding torque (τ_h), and the spring constant (k). Blocked force is defined as the force required to counteract the pulling or pushing force exerted by the HSA when one of its ends is rotated while preventing the

structure from changing length. The minimum energy length (L) is defined as the position where the linear force is minimized for a given θ rotation. Holding torque (τ_h) is then defined as the moment required to hold an HSA at a given θ at L. The spring constant is defined as the slope of the force displacement curve at the minimum energy length for a given θ.

All HSAs were cycled ten times and the median values plotted. Error bars extend from each point representing the minimum and maximum values encountered in the ten cycles. We elected to drop the first cycle of data from the plotted figures, due to hysteresis in HSAs made from FPU50 as described in [183].

An additional dimension to add to testing is that of time, particularly for FPU50. To characterize the HSAs holding force over time, we conducted a force-relaxation test. The test was conducted on a closed 8 row HSA with a 25.4mm diameter. The HSA was extended to 30mm over three seconds where it was then held for 20 minutes at an ambient temperature of approximately 22C (71F) and plotted over 5 seconds and the whole run with a Maxwell model of viscoelasticty fit to the data.

2.4 Results

2.4.1 The Effect of the Number of Row Tilings

The results for row tiling's effect on blocked force(F), spring constant(K), minimum energy length(L), and holding torque(τ) as a function of angle of twist θ can be seen in Figure 2.4. The blocked force trends in Figure 2.4A show blocked force increasing as a function of θ for all patterns. These are best modeled as a quadratic function of θ whose terms can be seen in table 2.3. We found that HSAs of lower row counts generate higher blocked forces for the same angle. We see from Figure 2.4C that row count has no effect on the length change of the actuator as a function of angle, demonstrated by an equal slope for all configurations. Therefore, compression is not driving the blocked force non-linearity; it is driven by the change in spring constant.

One would expect the spring constant for an HSA at rest, like a traditional spring, to

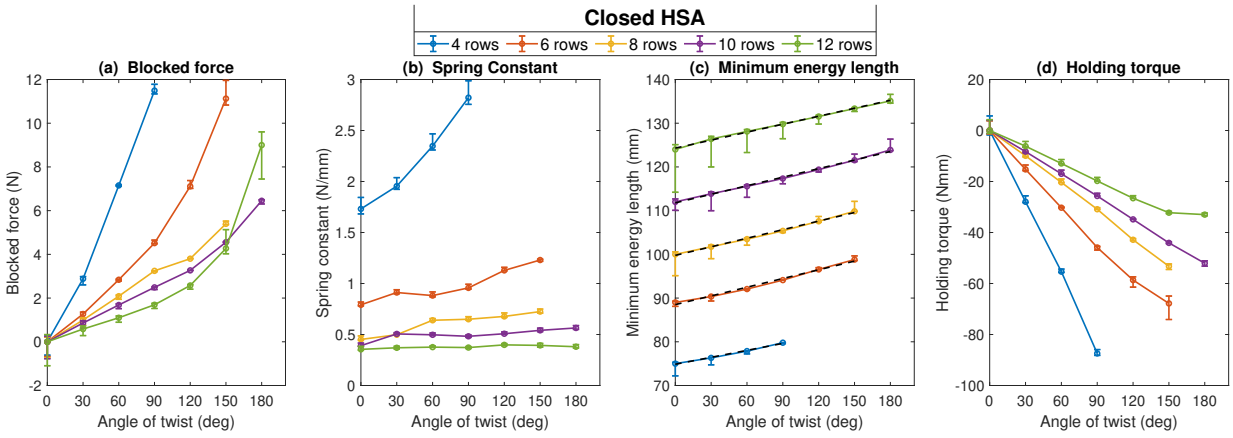

Figure 2.4: HSA properties as a function of number of cells for a traditional closed HSA design.

have an inverse relationship with the number of rows. This is because in the traditional wire springs the spring constant is governed by the equation,

$$k = \frac{Gd^4}{8n_cD^3} \tag{2.1}$$

where n_c is the number of coils, D is the mean coil diameter, G is the shear modulus, and d is the diameter of the winding. While our HSA does not have a circular cross section, the effect of coil count should be unaffected. In a closed HSA, the number of coils is the number of wide beams that wrap around the structure. Our HSA has a 3 way rotational symmetry about its axis so if we ignore the effect of the small beams the number of coils is three times the row count. At zero degrees of rotation, we find that there is an inverse relationship between the number of rows n_r and the rest state spring constant, however the power is -1.4 rather than -1.

What we would not anticipate from traditional models of springs is that that the HSA would stiffen as θ increases. While the pitch and total length changes as θ increases, equation 2.1 predicts that there should be no change in stiffness. In fact since the structure is auxetic, the mean diameter (D) would increase, and we would anticipate a decrease in

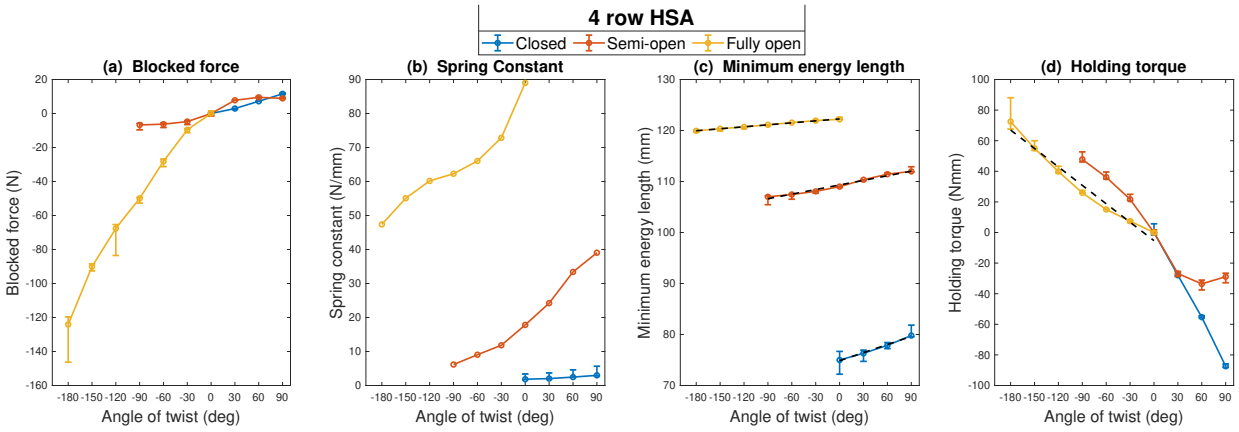

Figure 2.5: Key properties for HSAs printed along the auxetic trajectory with fixed number of cells.

stiffness. This effect is what makes HSAs fundamentally different from a simple spring. We found that the shorter the HSA was, the more quickly the spring constant changed as a function of θ (see spring constant fit values A in table 2.3).

Overall, smaller HSAs are less prone to problems such as buckling especially at higher twist angles. While these smaller HSAs are better suited for carrying force, they sacrifice the higher extension capabilities that come with more rows. The main tradeoff in choosing a row count is between throw (length range) and stiffness/blocked force. The consequence of having a higher blocked force for a closed HSA is an increase to the amount of torque a motor must produce. For the open HSA we found that all have a nearly perfect linear relationship between twist angle and holding torque. The twist-torque constant increases significantly as row tiling decreases. Overall for the same amount of length change in an actuator, the more row tilings there are, the less torque is needed.

Value	Blocked force			Holding torque		Spring constant			Minimum energy length		
Equation	$F_b = A\theta^2 + B\theta$			$\tau_h = C_\tau\theta$		$k = C_k\theta + k_0$			$L = C_l\theta + L_o$		
Constants	A	B	R^2	C_τ	R^2	C_k	k_0	R^2	C_l	L_o	R^2
4 row	-4.2339e-04	-0.0903	0.9988	0.9545	0.999	0.0122	1.6640	0.977	0.0531	74.8555	0.993
6 row	-3.3056e-04	-0.0228	0.9955	0.4770	0.993	0.0028	0.7747	0.902	0.0664	88.5024	0.989
8 row	-1.4010e-05	-0.0329	0.9909	0.3521	0.999	0.0018	0.4700	0.906	0.0653	99.7678	0.996
10 row	-8.4170e-05	-0.0194	0.9917	0.2899	0.999	7.1581e-04	0.4339	0.713	0.0653	111.7795	0.997
12 row	-3.1436-04	0.0115	0.9878	0.2039	0.999	2.6294e-04	0.3576	0.831	0.0608	124.3016	0.997

Table 2.3: Fit functions and their parameters for HSAs with varying rows

2.4.2 Auxetic Trajectory

The effect of changes in the auxetic trajectory point can be seen in Figure 2.5. We see the effect of increasing θ (counterclockwise rotation) decreasing θ (clockwise rotation) on the structure blocked force, spring constant, minimum energy length and holding torque. For all structures the blocked force is 0N when no rotation is applied. As expected, the closed HSA only has a positive theta range and generates a pushing forces as θ increased from 0. The fully open HSA by contrast only has a negative theta range from 0 to -180 degrees. It generates a pulling force that grows with rotation (negative θ). This force peaks at the end of its rotational range of -180 degres, generating a maximum force of 124N. This contractile force is caused by the structures minimum energy length decreasing as θ decreases as seen in Figure 2.5c. The semi-open HSA meanwhile has a rotation range with positive and negative θ. It expands in the positive θ range and contracts in the negative θ range. The result is that the blocked force can be both positive (expanding) and negative (contracting). The expansion force at +90 degree of the semi-open (8.9N) is comparable to that of the closed HSA(11.6N).

We can observe from this that the auxetic trajectory point is a major factor in controlling blocked force, and that it is directly driven by the changing the range of angles that can be achieved and the resulting change in length. For all HSAs, minimum energy length is a

linear function of θ of the form $L_{HSA} = C_l\theta + L_0$ with L_0 being the length at zero rotation and C_l being the rotation-extension coupling constant. It should be noted that the closed HSA has the largest rotation-extension coupling constant of 0.053mm/radian followed by semi-open (0.030mm/radian) then open (0.013mm/radian). This is expected since the HSAs follow the auxetic trajectory as they are twisted. When ϕ is small, minor changes in ϕ result in large translations to the height of the unit cell. As ϕ approaches $\phi_(max)$, large changes in ϕ produce relatively small changes in height.

For all HSAs, the spring constants increased as θ increases as seen in Figure 2.5B. The Open HSA has a significantly higher spring constant that the others which reaches it maximum at zero rotation. This is primarily due to the open HSA having straight connections between the top and bottom, which must be pulled or compressed till buckling to move. It is the combination of high spring constant and low rotation-extension coupling constant that causes the open HSA to have such a large blocked force. Unlike the closed HSA, the spring constants are nonlinear functions of θ for the open and semi-open HSA. It should be noted that the lowest spring constant for the open is higher than the highest of the semi-open. The same is true for the Semi-open and the closed. Therefor the point along the auxetic trajectory that is used should be considered the primary determinant of stiffness in HSA design.

The required holding torque as a function of the angle of rotation for the three different auxetic trajectory states is shown in Figure 2.5D with the torque being 0 Nmm when no rotation is applied. Unlike the closed HSA, the semi-open and open HSAs do not have a linear relationship between angle and torque. For the semi-open there is a small linear region between -30 and 30 degrees. For the open HSA the holding torque can be modeled as a quadratic function of θ of the form $(-1.219\times10^{-4})\theta^2 + 0.1834\theta$ With this data, we can how see how much torque and angle range would be needed to drive the various types of HSA to to their desired stiffness, length or force by examining what twist angle would be needed.

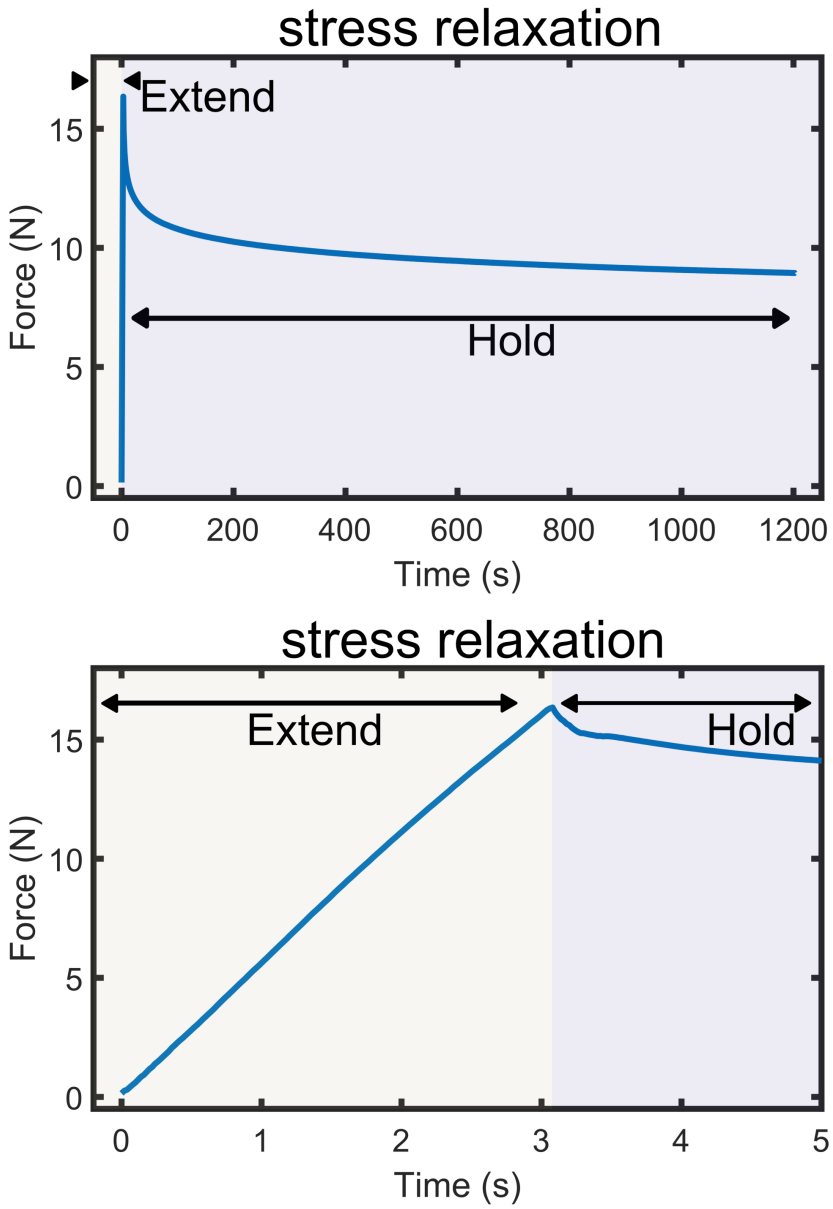

Figure 2.6: Stress relaxation on a closed 8-wrap HSA shows that the structure will ultimately loose half of its holding force over time.

2.4.3 Stress relaxation

The stress relaxation results of a closed 8 wrap FPU50 HSA can be seen in Figure 2.6. It shows severe degradation in holding force over time. This is due to the material's viscoelastic properties. At 30mm of extension we see a peak of 16.3N blocked force on the HSA. after 0.1s of holding, blocked force drops by 0.7N (4.3%). At 0.5s and 1s, blocked force is down 1.3N(8.5%) and 1.7N(11.8%). 5 seconds after peak, blocked force is down 3.1N(23.0%). Ultimately after 1200 seconds the force drops 7.4N(45%).

The response is typical of materials with multiple relaxation modes. We find that by fitting exponential fits from peak force to +0.16 and a second fit of force +0.16 seconds to 1.2 seconds we find a relaxation modes with a time constant of 3 seconds and 18 seconds respectively. Therefor for actuation that is much faster than 3 seconds we can assume elastic performance and can ignore viscoelastic effects. For longer time scales, a more complex model would be needed when using the FPU material. For applications where long term force outputs are required, manufacturing the HSA out of a material with a longer time constant would be suggested.

2.5 Conclusion and Future Work

In this paper we examined two key parameters of HSA design, the point along the auxetic trajectory, and the number of cells vertically that had both been overlooked in past work. We found that the point along the auxetic trajectory that was set as the rest state has a dramatic effect on the actuators performance, far beyond the other parameters that had been studied. Changing the auxetic trajectory point allowed us to expand the range of blocked forces up to 150N, generate stiffness over 80 N/mm, and expand the range of actuation to include contraction and bidirectional actuation. By studying the effect of length on traditional closed HSA actuators, we found that shorter HSAs generated higher forces and stiffer structures at the cost of lower extensions and higher torques. For both parameter sets we studied the coupling between extension, stiffness, angle, and torque. The characterization provides

the information needed for future researchers to select motors, information that is critical to design efforts. While current materials and fabrication methods may limit time scale of force application due to stress relaxation, we believe future manufacturing improvements will overcome this limitation and that the trends we have found will generalize to other materials. There are still several parameters to explore, including cell aspect ratio, ratio of beam widths, and the connection to the mounting point. This work lays a foundation for applications of HSAs as entirely electric and compliant actuation in grippers, arms, exoskeletons, and any other soft robotic application and sets a direction for future improvements to HSAs.

Chapter 3

SPRING BRAKE! SYSTEM IDENTIFICATION OF HANDED SHEARING AUXETIC BASED LEG ENABLES EFFICIENT OPEN LOOP HOPPING AND STANDING BEHAVIOR

3.1 Notice

Please note, this work is a part of a co-first author publication. Certain sections have been removed as they are not contributions towards this thesis. For access to these sub chapters, please wait for the work to be published, or view Joseph Sullivan's Thesis Dissertation after he defends.

3.2 Summary

In this letter, we present a prismatic leg with a metamaterial viscoelastic spring element that enables multi-functional performance in hopping and standing. Legged robots struggle to perform compared to biological systems. This has been theorized to be because due to to a lack of multi-modality in component hardware. This work aids in closing that gap through the incorporation of a metamaterial viscoelastic spring element which also serves as a breaking mechanism to aid in standing or to absorb large loads. This work characterizes the metamaterial's performance through system identification and creates an open loop control policy that demonstrates stability. When operating as a spring element, the metamaterial reduces thermal buildup in the motor by 19% to 31%. When operating as a break, it reduces the energy cost to stand from a quadratic function to sub-linear, resulting in more than a 400% reduction in average power needed to resist a constant load.

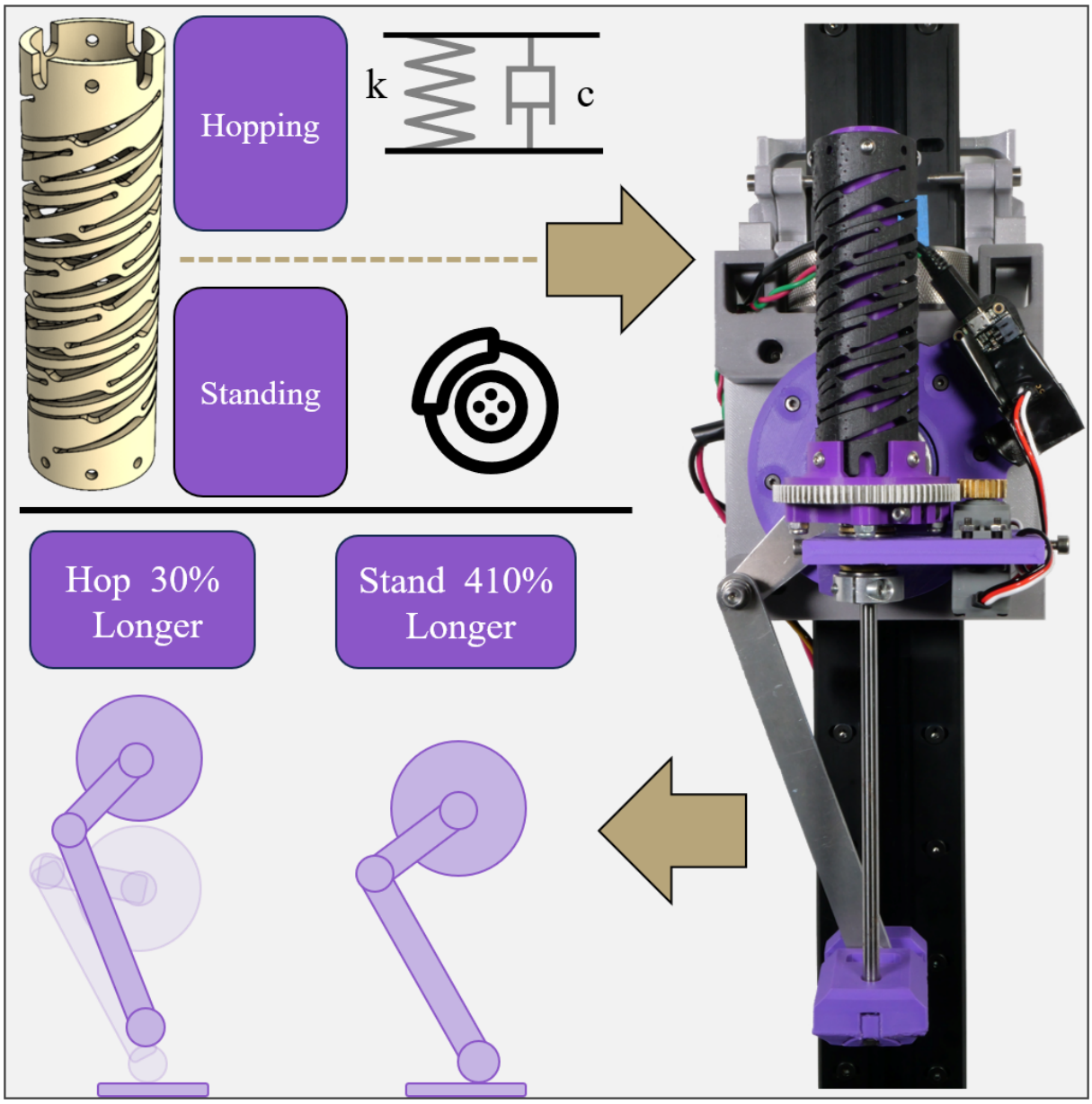

Figure 3.1: Here we demonstrate a parallel elastic actuator using a handed shearing auxetic as its viscoelastic spring element. The HSA works as both a spring element as well as a breaking mechanism to improve the robots ability to both locomote and stand. A system identificaion method was developed to characterize the HSA properties on small time scales. This was fed into a trajectory optimizer and a stable, open-loop hopping behavior was demonstrated.

3.3 Introduction and Related Works

Legged robots have a power problem [196]. Custom off the shelf legged robotic systems have a high cost of transport, limiting their capabilities [20,162]. Efforts have focused on improving the efficiency of robotic legs and have shown great improvements [17, 58, 59, 75, 181]. Yet, a gap still remains between the cost of transport of robots and their equivalents in biology [184]. There is a fundamental trade off in hardware design between size, weight, power, and cost (SWaP-C). There are also efficiency trade offs between the different functionalities expected of robot legs such as locomotion and standing [145]. Multi-modality and multi-functionality in robot design has demonstrated great potential in overcoming some of these limitations [27, 199].

One critical challenge of Legged robots is the ability to both hop and stand. Optimizing wholly for one requirement can come at the detriment of the other due to the inherent tension between a robots needs for hopping, standing, and their energy constraints over time [145, 162]. Most of mobile legged robots use advanced controls to emulate compliance [82, 175, 195] with the robot's motors. This solution requires fast control loops [18, 25], and is energetically expensive compared to a mechanical solution because of the need for actuators to do negative work, as well as thermal losses due to heating of motor windings. Legged locomotion can get around this by instead adding a compliant element [186, 189]. While individually optimized elements improve cost of transport for their specific niche, they add mass and complexity that harm other robot functions. By using multi-functional embodiments, robots can take inspiration from biological systems that are demonstrably more efficient and significantly more multi-functional [7, 27].

In this work, we add a single additional visoelastic spring element in the form of a Handed Shearing Axuetic to a prismatic leg. We show that the HSA acts as both a multi-functional spring and break mechanism. We compare performance against an optimized trajectory without the HSA and demonstrate energy improvements similar to a traditional spring. Including the HSA reduces thermal and energy costs during hopping and adds an efficient

standing mode in a single multi-functional element.

In this paper we:

- Evaluate HSAs as a multi-functional viscoelastic spring element in a robotic leg.
- Develop a system identification method modelling the HSA as a potential energy function.
- Use trajectory optimization to find a stable and efficient open loop hopping behavior.

HSAs have been used to create many robotic systems. Characterizations [63, 111, 183] have enabled human-brain interfaces, turtle robots, grocery picking, etc [33, 91, 171]. However, established HSA characterization can not create a model for the performance we desire. Existing literature operates in quasi-statics and on a much longer time horizon. We accomplish this by dynamically characterizing the HSA using a lagrangian model framework. Then use a System Identification Method to model the effect of the HSA on leg dynamics. We then use the model in an open loop trajectory optimization. This model captures the linear and non-linear stiffening behavior of the HSA. This allows the HSA to contribute during both an active hopping gate and when its standing.

This system identification modelling is required as HSAs have demonstrated hysteric properties [63]. This system demonstrates similar performance to traditional metal spring elements in robotic leg literature and enables significant reductions in standing energy. This work adds to the literature base and understanding of the benefits of multi-functionality in legged robotics.

3.4 Methods

3.4.1 Design Principles for an HSA Hopping Robot

Visco-elasticity is a common design element in legged robots. Visco-elastic dynamics improve dynamic stability by attenuating disturbances. It is often implemented electromechanically

through the application of proportional - derivative (PD) control laws, or through inclusion of mechanical spring-damper elements in series or parallel with the kinematic chain of a leg. Mechanical spring elements can reduce negative work from motors and improve energy efficiency by modulating the flow of energy between kinetic and potential modes during dynamic motions. This is beneficial as negative work in the motor results in thermal buildup in the windings. These mechanical springs can be arranged to support body loads from gravity, reducing the quiescent power required when the robot is standing or sedentary.

The benefits outlined above points towards a novel application of HSAs as parallel elastic actuators for legged locomotion. To this end, we designed an HSA to be incorporated into a prismatic leg actuator for a hopping robot. We derive the specifications for a parallel HSA actuator from the energetics of an ideal spring-mass-oscillator under the affect of gravity. We then use this oscillator model to give the HSA stroke length and stiffness characteristics as a function of robot mass, hopping height, and frequency. A candidate HSA is selected by referencing length and stiffness properties of the oscillator model against prior studies that characterize the affect of HSA design parameters on force, torque, and deflection relationships [63, 183].

In addition to visco-elastic behavior present in the HSA, we observed that the auxetic property of HSAs can be exploited to jam a kinematic mechanism. This allows the HSA to act as a brake that can resist large external loads for long durations. This enables multiple modalities through a single mechanism. Jamming is accomplished by nesting a concentric cylindrical wall inside of the HSA. As the HSA is extended vertically and not allowed to rotate, the inner diameter collapses into the cylinder wall. This results in an exponential increase in the stiffness where the device becomes rigid and approaches properties of the bulk. Jamming is induced on demand by twisting the HSA with a small hobby servomotor (GoBilda 2000-0025-0504).

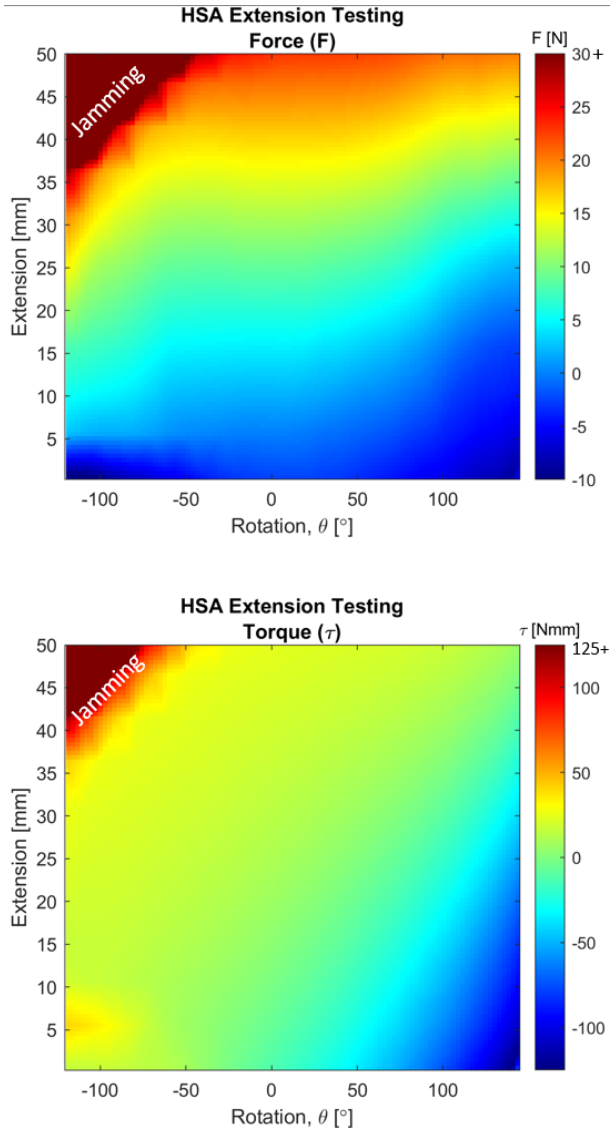

Figure 3.2: Heat maps of force and torque produced by the HSA as a function of linear and angular displacement. Jamming begins occurring around $-45^{c}irc$ rotation and 50mm displacement. Outside of the jamming region, we see relatively constant changes in force as a function of displacement. In Torque, we see relatively constant torque requirements. In the jamming region, both force output and torque requirements are higher.

3.4.2 Quasi-Static HSA Properties

In this section we characterize important properties of the HSA, namely its relationships for force and torque over displacement and rotation, θ. The HSA was tested in the same configuration as shown on the robot, including the smaller cylinder inside the HSA used for jamming. Characterization was recorded on an Instron 68SC-2 at 200Hz. Data points were collected in linear displacement over a range of 0 to 50mm every 5mm. Rotation data was additionally collected from $-145°$ to $120°$ every $10°$. Measurements were taken at a rate of 10mm/s following previous HSA characterization works [63, 183]. Unlike past works that characterized HSA performance solely on minimum energy length, blocked force, or a combination of the two, this work looks at a more complete picture of the linear and rotational displacement landscape. This provides a more accurate validation for the proposed HSA characterization, and is crucial for characterizing the jamming effect described previously.

Force - Torque Characterization

In this section, raw force and torque values from the instron is processed into a surface through linear interpolation and then plotted as a color map. Interpolated data is used as a comparison for the system identification method presented later in this work. Regions above 30N force and 125Nmm torque were capped on the color bar as these were the found to be the maximum values when testing the system without the jamming cylinder present (ie they are the forces produced by the HSA alone).

As shown in Fig. 3.2, the range of force values demonstrated by the HSA ranges from -10 N in compression at $(-120°, 50mm)$ to 300 N in extension at $(-120°, 0mm)$. This extremely large extension force is due to the auxetic nature of the HSA closing down on the jamming cylinder in a Capstan effect. Outside of this region, we find the force values to be relatively linear. As displacement increases, force increases in kind, resulting in a constant spring constant.

Torque is also plotted in in Fig. 3.2 and represents the required torque to hold the

HSA at a given θ. Values range from -125 Nmm to over 500 Nmm at $(140°, 0mm)$ and $(-120°, 50mm)$ respectively. These target values are used to spec the hobby servo to ensure safe functioning.

Braking

Using the raw instron data, a simulated hop is conducted by fixing θ and allowing displacement to vary from 0 to 50 mm. An average spring constant is then calculated for each rotation. This simulated hop occurs at a much slower speed than in the actual robot but serves as a baseline of comparison. As can be seen from Fig. 3.3, the HSA displays relatively constant spring constants through large positive rotation angles around 900N/m. As rotation tends negative, jamming begins at $-50°$ and exponentially increases beyond that to reach a max above 16,000N/m at $-120°$ rotation. This was determined by finding the +3dB point.

3.4.3 Hardware Implementation

The robot consists of a prismatic actuator built from a closed kinematic chain connecting a quasi-direct drive motor (MJ Bots QDD100 Beta 3) to a foot as shown in Fig.3.4. An HSA is integrated into the vertical prismatic link, acting like an extension spring. The HSA is allowed to rotate around the link through a geared down servo motor (4:1, GoBilda 2000-0025-0504). Concentric to the HSA and connected to both ends, a smaller, telescoping cylinder is installed. This allows the HSA to jam against it due to the auxetic nature of the HSA. This allows the HSA to become a multi-functional element in the leg. Because the HSA is installed in parallel, any ground forces that reach the motor must also affect the HSA. Thus, when the HSA is jammed against the cylinder, it serves as an impact absorbing device.

For testing, the QDD motor is mounted to a vertical bearing cart. This confines the motion of the leg to be purely vertical. The leg and bearing cart weigh 1.3kg with the motor and 800g without. Additional weights can be added to the leg, to the tune of 1kg of additional payload.

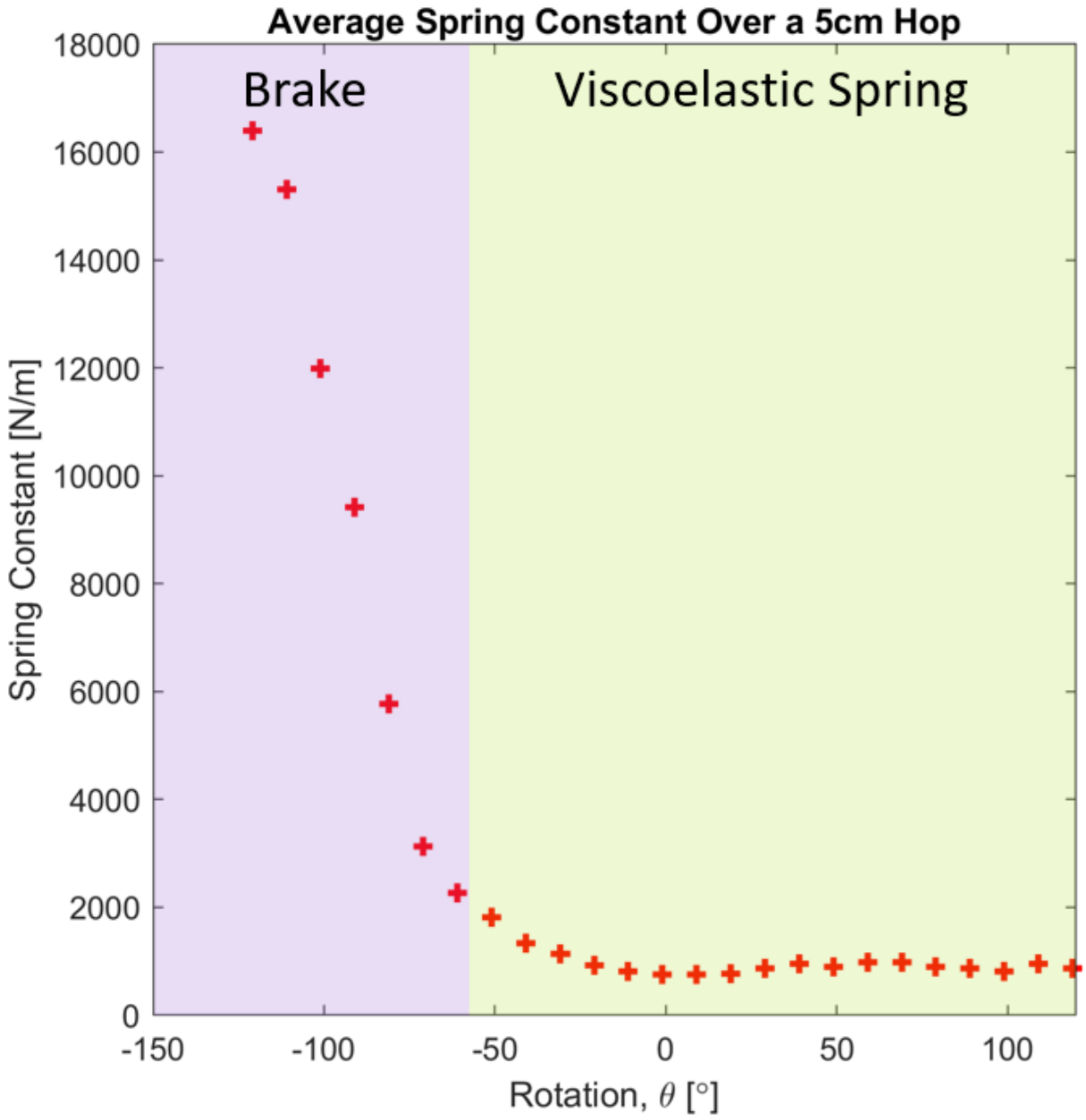

Figure 3.3: Here we present a Simulated Instron Hop and demonstrate the two stiffness regions that the HSA enables: visoelastic hopping and breaking. Breaking for negative θ values greater than -55°. It reaches a stiffness of more than 16,000N/m. In the spring modality, the HSA acts as a spring element with a stiffness around 900N/m.

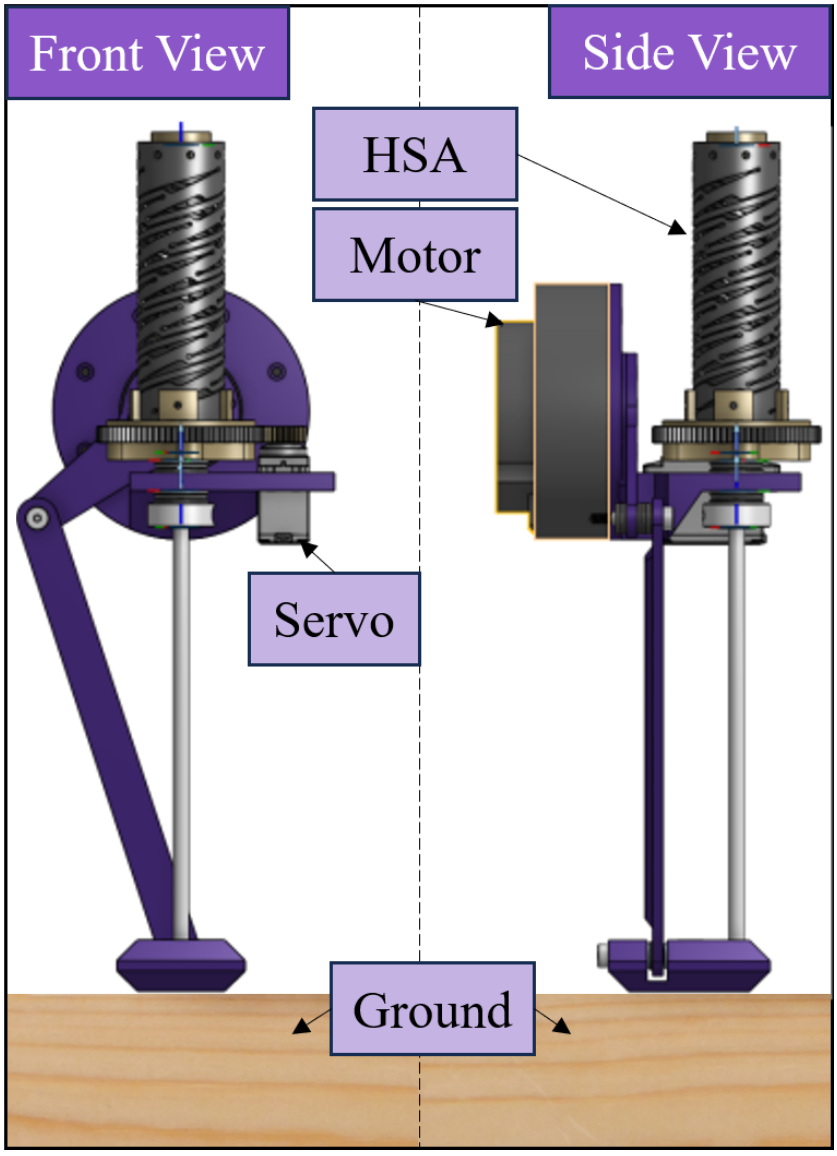

Figure 3.4: A system overview is provided on the robot leg. The leg consists of a prismatic actuator connecting a quasi direct drive motor the the foot. The HSA is incorporated in parallel and the geared down stepper motor is used to set the HSAs rotation, θ. Concentric to the HSA, there is a shaft that the HSA can jam against to produce braking. The leg is mounted to a vertical rail system, constraining motion to vertical hopping.

The electronics interface with and are controlled by an off-leg raspberry pi 4b. All HSAs presented in this work were printed on a Carbon M1, digital projection lithography 3D printer. Parts were handled, cleaned, and cured following the manufacturers instructions.

3.4.4 Dynamic HSA Characterization on the Robot

This section has been removed from this work.

Lagrangian Model Framework

This subsection has been removed from this work.

System Identification Method

This subsection has been removed from this work.

3.4.5 Hopping Trajectory Optimization and Control

This subsection has been removed from this work.

3.5 Results

In this section we demonstrate the stability of our system control law, demonstrating the strong characterization through system identification. We show the height-normalized energy cost of hopping for a case with the HSA and without as a function of robot mass. We show the thermal energy savings of breaking using an HSA compared to the motor.

3.5.1 Dynamic Characterization Captures HSA Hysteresis In Periodic Motions

This section has been removed from this work.

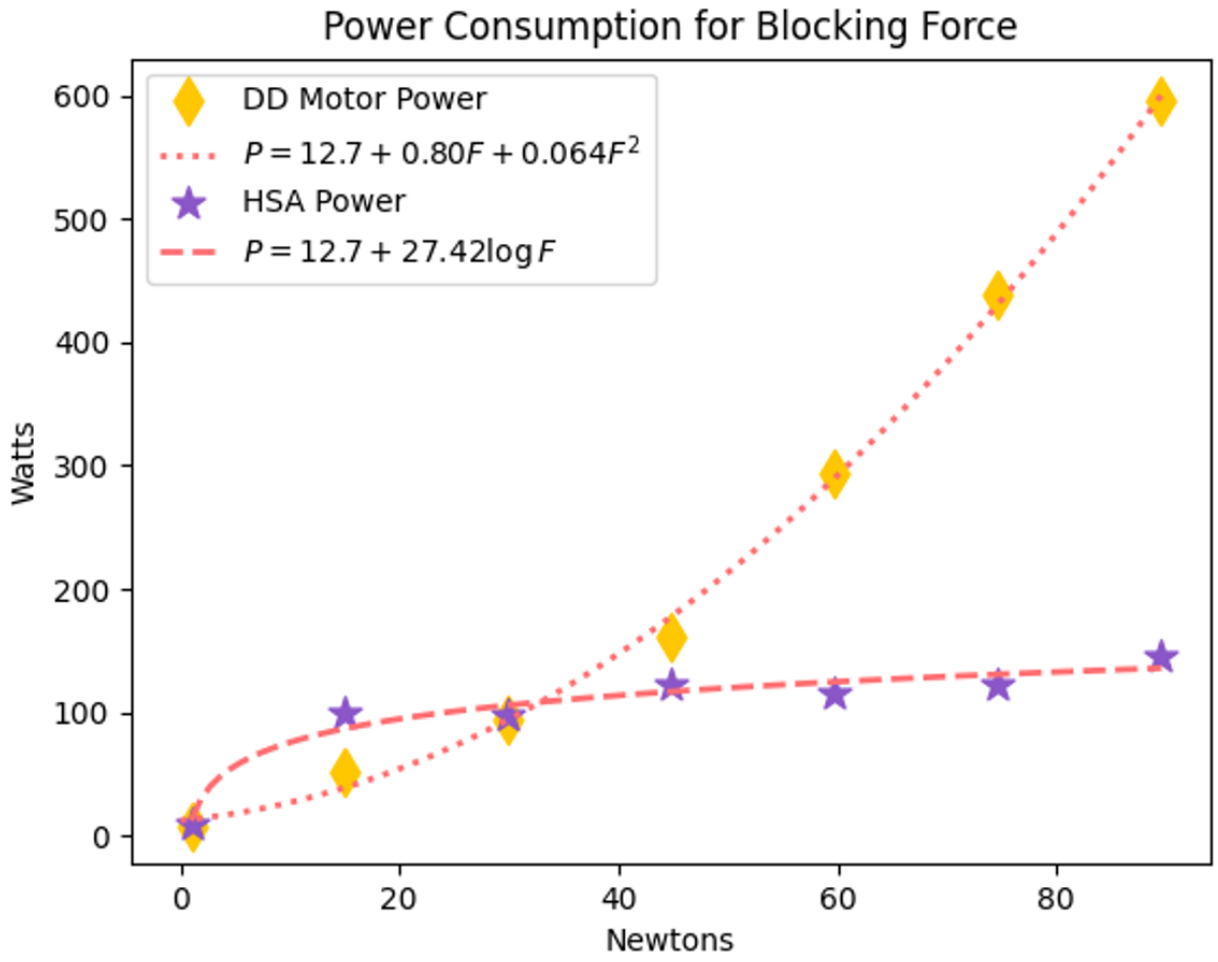

Figure 3.5: Total system power consumption as a function of ground reaction force for both the jammed and unjammed cases. System power is depicted with a purple star (HSA Jammed) and yellow rhombus (HSA Unjammed). For small foot loads, the additional mass and quiescent power consumption from adding the servo system results in additional power draw. Beyond 30N of force on the foot, the addition of the HSA system saves power. The unjammed case follows a quadratic equation while the jammed case follows a sub-linear equation.

3.5.2 Jamming Drastically Reduces Cost of Static Force Transduction

While robots are often on the move, there are times when the ability to stand still is valuable. In Fig. 3.5, we present the total system power required for the robot to resist a force applied to the foot. We test two configurations (HSA jammed, HSA unjammed) for seven different forces applied through the foot. First, the quiescent power was measured (12.7W), and then the force applied to the foot and the average system power usage was recorded. This plot shows the average system power. When Jammed, the HSA was set to an angle of $-157.5°$, resulting in a stiffness beyond the 16,300N/m seen in Fig.3.3. For loads below 30N, the unjammed power consumption was lower, pointing to the additional costs of the servo and HSA mechanisms. Above 30N however, the jammed case dramatically outperforms the unjammed case. The unjammed system sees an average power draw near 600W compared to 140W for the jammed case. When fitting curves to the data, we see a quadratic fit for the unjammed case and a (sublinear) logarithmic fit for the jammed case. This suggests very favorable scaling as the robotic leg grows larger and supports larger payloads. While the energy savings here are important, its also important to consider the thermal and saturation savings as well.

3.5.3 HSA Provides Gains in Hopping Efficiency

This section has been removed from this work.

3.6 Conclusion and Future Work

In this paper we describe a multi-functional jumping robot made from a parallel elastic actuator using handed shearing auxetics for legged locomotion. We use the often unfavorable viscoelastic properties of HSAs to impose beneficial dynamics on the robot leg. We describe a system identification method to fit potential energy functions and hysteresis functions. This model is fed into a trajectory optimizer and a stable, efficient open loop trajectory is demonstrated. We present height normalized energy costs for the leg with different payloads.

The HSA demonstrates efficiency gains similar to that of a traditional mechanical spring. The auxetic nature of the HSA also allows a jamming mode to be integrated into the leg. This reduces constant force energy costs (like from standing) from quadratic equation to a sub-linear relationship. Future works include rigidizing plastic components to further explore the space of realizable impluses, testing the leg over different terrains, and leveraging the non-linear stiffness properties of HSAs [63] to create a variable stiffness, jamming prismatic actuator that can optimize performance over different terrain.

This work lays the foundations for the inclusion of viscoelastic metamaterals to add multi-modality to legged robots. This work also demonstrates system identification as a meaningful way of characterizing HSA dynamics for periodic motions.

Chapter 4

ENHANCING THE PERFORMANCE OF PNEU-NET ACTUATORS USING A TORSION RESISTANT STRAIN LIMITING LAYER

4.1 Summary

Pneunets are the primary form of soft robotic grippers. A key limitation to their wider adoption is their inability to grasp larger payloads due to objects slipping out of grasps. We have overcome this limitation by introducing a torsionally rigid strain limiting layer (TR-SLL). This reduces out-of-plane bending while maintaining the gripper's softness and in-plane flexibility. We characterize the design space of the strain limiting layer for a Pneu-net gripper using simulation and experiment and map bending angle and relative grip strength. We found that the use of our TR-SLL reduced out-of-plane bending by up to 97.7% in testing compared to a benchmark Pneu-net gripper from the Soft Robotics Toolkit. We demonstrate a lifting capacity of 5kg when loading using the TR-SLL. We also see a relative improvement in peak grip force of 3N and stiffness of 1200N/m compared to 1N and 150N/m for a Pneu-net gripper without our TR-SLL at equal pressures. Finally, we test the TR-SLL gripper on a suite of six YCB objects above the demonstrated capability of a traditional Pneu-net gripper. We show success on all but one demonstrating significant increased capabilities.

4.2 Introduction

A key component of human's remarkable grip is that our fingers can simultaneously bend while being resistant to torsion and lateral loading. Soft robotic fingers have focused on emulating the ability of human and other biotas compliance when bending and found great success in the academy and industry as a result [153]. This bending motion defines a plane

of desired movement for the finger or actuator. While in plane bending and compliance are desired, movement normal to this plane, or out-of-plane deformation has been identified as a major limiter in for soft robotic systems.

Out-of-plane deformations limit a soft robotic grippers' ability to grasp and manipulate heavy objects. Soft robotic systems have been able to achieve large payload capacities, able to lift car tires and dumbbells [106–108]. However, this has required the gripper to cage the object or pull directly against gravity. Holding objects perpendicular to gravity or having large movements cause soft robotic grippers to deform and twist and ultimately loose their grasp. A second limitation of soft grippers has been that the out-of-plane deformation in the fingers leads to uncertainty in the positioning of the grasped object. A successful but heavy grasp can cause a gripper to deform in such a way that localizing relative to the arm is difficult. Here we show how a Torsion Resistant layer can increase the out-of-plane payload capacity of Pneu-net grippers to 5kg (FigB.1).

For Pneu-nets [124], this fundamental limitation comes from the use of simple rectangular beams as the strain limiting layer (SLL). Rectangular cross sections have low second moments of inertia in one direction, allowing them to bend in the thin direction. While in theory this would make them able to resist deformations along their thick direction, in practice these structures have a low resistance to torsion. This causes any out-of-plane loading to generate a twist in the SLL.

Several strategies have emerged for improving the out-of-plane performance of soft grippers through the SLL. One approach focuses on changing the material distribution by using multi-material topology optimization [190]. Another approach discritizes the SLL and inserts hinges to allow a thicker material to still bend [114]. The first still experiences large out of plane deformations while demonstrating smaller increases in torsional stiffness. The second requires significantly higher input pressures and the inclusion of hinge based strain limiting layers (SLL) can reduce the structures ability to conform to objects.

We focus on using advancements from the field of compliant mechanisms to change the geometry of the SLL. We use triangulated beams as the torsion resistant strain limiting layer

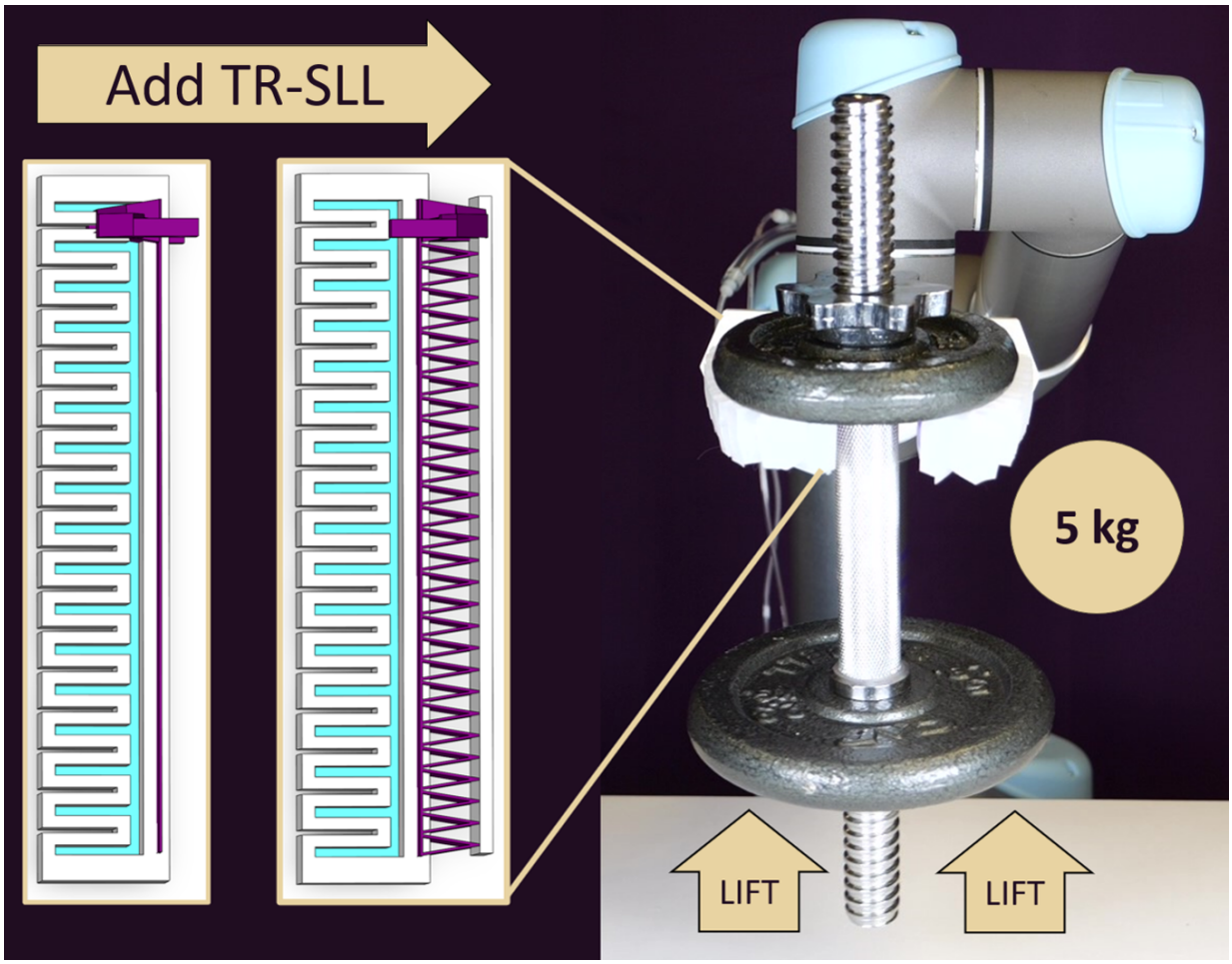

Figure 4.1: We create a new Torsion Resistant Strain Limiting Layer (TR-SLL) that can be added to any existing Pneu-net based gripper. It increases their resistance to torsion, allowing the gripper to lift larger payloads. Additionally, we can load the skeleton of the TR-SLL directly, dramatically increasing lifting capacity. We show the TR-SLL gripper lifting a 5kg dumbbell using the skeleton, the maximum payload capacity of the UR5 robot arm.

(TR-SLL) of Pneu-net. These triangulated beams resist torsion but allow bending on planar and spherical surfaces [132, 150]. While one might expect the triangles along the beam to localize the deformation to interfaces between triangles, the structures deform over their entire length, with all sides of the triangle deforming when bent. The triangularized beams act as a continuum structure with enhanced stiffness to out of plane bending and torsion.

We integrate the TR-SLLs into standard Pneu-net grippers and provide a step-by-step guide for integrating the TR-SLLs. Next, we perform a parametric sweep on the TR-SLLs to provide a design guide. We found that there was minimal difference between triangle designs for in-plane bending compared to flat SLLs. We found a trade-off between torsional stiffness and stress concentrations in the TR-SLL. We tested the integrated gripper on a cylindrical pull test and found that the addition of the TR-SLL increased the gripping force by 3x and increase the stiffness in the grip by 7.8x. Finally, we tested the gripper by picking up a weighted structure entirely using the sides of the gripper. As seen in Figure 1, the TR-SLL gripper can pick up a 5kg weight (the max capacity of our UR5) using lateral loading.

In this paper we:

- Model key parameters for understanding a Torsion Resistant Strain Limiting Layer
- Characterize in and out-of-plane bending performance against a benchmark Pneu-net gripper
- Demonstrate the increased payload and lifting capacity of the Torsion Resistant Strain Limiting Layer

4.3 Background

Soft robotics researchers have attempted to improve the out-of-plane performance of Pneu-nets using several techniques. One method is to redesign the gripper as a whole. This can involve putting a skeleton around the entire gripper [155]. However, this requires significantly more input pressure to reach the same normal force output and demonstrates smaller lifting

capacity. Another method involves optimizing the design of individual cells to improve torsion resistance [173].

Active strain limiting layers are another area of active research. Many of these change their SLL stiffness through phase change [201], jamming chain, [87] or through the thermoelectric properties of Field's metal [26,65] or by heating hydrogels, causing them to swell [188]. Additionally, work has been done to use jamming to increase a grippers ability to grasp objects and increase out of plane grip strength [45]. Many of these require significant infrastructure to support their use relative to a passive Pneu-net actuator, and are more challenging to manufacture.

Our solution allows a simple passive SLL made from a single material to be easily integrated into existing Pneu-net designs. It demonstrates a large torsional spring constant and high normal force output for a comparatively low input pressure. It can be made with a low cost 3D printer and uses no additional infrastructure beyond a benchmark Pneu-net.

4.4 Derivation of the effect of Torsion on Antipodal Gripping for Soft Bodies

Antipodal gripping is a widespread application for soft robotic grippers. It involves picking up an object through two opposite points. There are three common limits to a soft grippers ability to perform an antipodal grasp; insufficient normal force, slippage due to torsional deformation, and shearing of the soft layer. All three of these modes as well as an example antipodal grasp can be seen in Fig. 5.2. The minimum of these three modes govern the payload capacity for a simply lifted object. If the payload minimum is governed by insufficent normal force, the force a gripper can lift is shown in Eq. 5.1.

$$F_{static} = \mu F_n \tag{4.1}$$

where F_{static} is the maximum force a gripper can lift, μ is the coefficient of static friction, and F_n is the normal force the gripper applies as shown in Fig. 5.2. If instead the gripper is just at the limit of slip from twisting, we get:

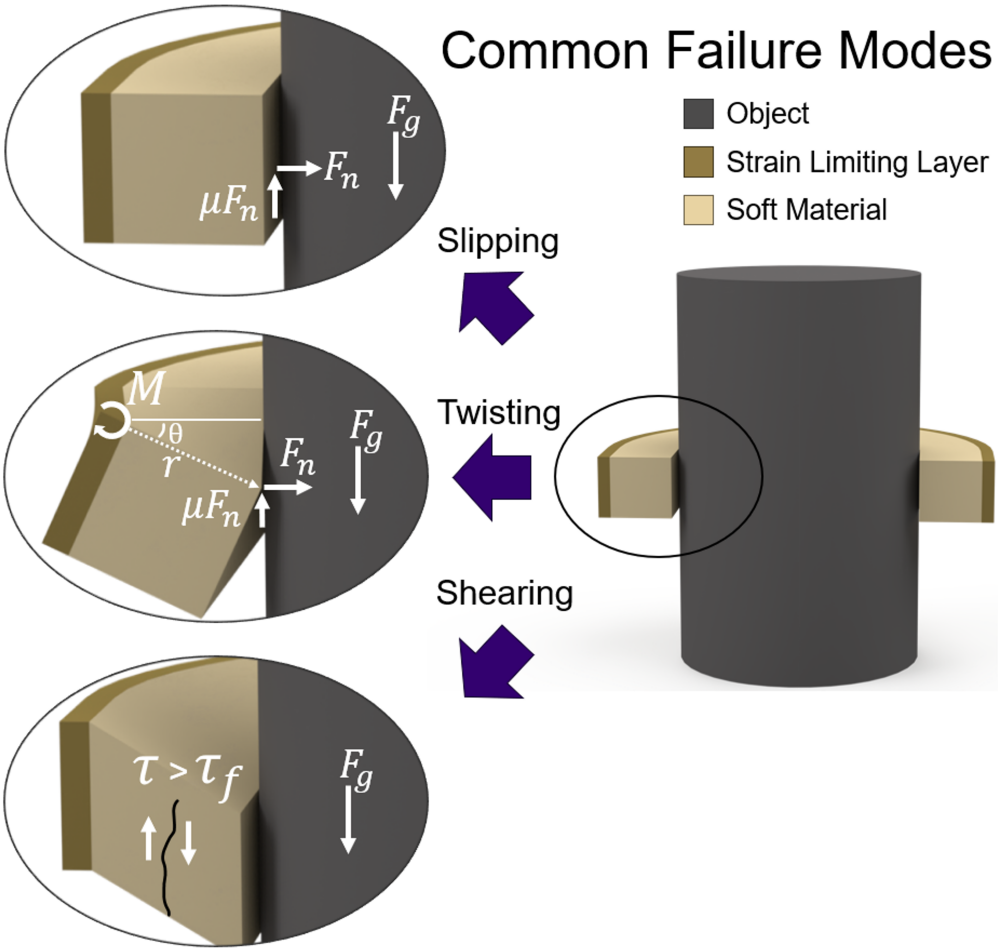

Figure 4.2: We demonstrate the common failure modes for Pneu-net grasping. On the right we can see a simplified gripper grabbing a cylinder using an antipodal grasp. Only the Strain Limiting Layer and soft gripping material between the SLL and object is shown (not to scale). On the left, three common failure modes are shown; slipping due to low normal forces, twisting due to torsional deformation in the SLL, and shearing of the soft material. The maximum payload capacity for a Pneu-net gripper is governed by the minimum of the set of these. Our gripper increases the torsional resistance and normal force applied compared to a standard Pneu-net gripper. This allows our gripper to lift larger payloads while having a better understanding of where the object is in our grasp.

$$M = F_g r \tag{4.2}$$

$$M = \kappa\theta \tag{4.3}$$

where M is the Torque on the SLL, F_g is the gravitational force from the object, r is the distance from the neutral axis of the gripper to the object, κ is the torsional spring constant from twisting failure (Fig.5.2, and θ is the angle of twist relative to the normal force. These can be seen labeled in the twisting failure mode in Fig. 5.2. If we assume there is some small vertical deformation x as the gripper is loaded but no slip or rolling occur, we get Eq. 5.4.

$$x = r\theta \tag{4.4}$$

Combining Eq. 5.2, Eq. 5.3, and Eq. 5.4 we can solve for F_g as a function of x:

$$F_g = \frac{\kappa}{r^2}x \tag{4.5}$$

Where $\frac{\kappa}{r^2}$ is the effective stiffness of the system.

Shearing of the soft gripping material can be another concern and is defined when:

$$\tau > \tau_f \tag{4.6}$$

Where τ is the length of the shear vector in the material and τ_f is the shear fracture of the material. For this study τ was never found to be greater than τ_f. If reached, changing the geometry or material selection could increase payload capacity further.

Together the minimum force value from Eq. 5.1, Eq. 5.5, and Eq. 5.8 govern the payload capacity of a soft gripper performing an anti-podal pick on a simple object. Since Pneu-nets grippers often demonstrate out of plane deformation as the most common failure mode, this work looks to Eq. 5.5 as a way to increase the payload capacity of Pneu-net grippers.

4.5 Design of Torsion Resistant Strain Limiting Layer

This section establishes a benchmark of comparison for our TR-SLL. It explores the design space for Strain Limiting Layers and evaluates them based on their in-plane and angular displacement as a function of thickness. We explore the design space of the TR-SLL gripper in simulation by varying the number of triangles present over the length from two to thirty. Finally, we use the simulation results to inform which gripper to instantiate in the real world. We present the fabrication process and test methods for comparison for the TR-SLL compared to the SLL. Based on the analysis in section A, a strong torsional spring constant will be critical for a high payload capacity. Additionally, strong in-plane bending performance will allow the gripper to lift a larger range of objects for a given antipodal mounting distance.

4.5.1 Benchmark Design

We used the Pneu-net from the Soft Robotics Toolkit as our benchmark design. [76]. We create our TR-SLL gripper by replacing the benchmark SLL with a 3D-printed TR-SLL and adding a thin layer of Ecoflex 00-30 to the tips of the triangles to maintain the same gripping surface. Both the benchmark and TR-SLL gripper can be seen in cross section in Fig. B.1 with the air pockets highlighted in blue, and the Strain Limiting Layers highlighted in purple.

4.5.2 Traditional Strain Limiting Layers

We need to establish a baseline of comparison for our TR-SLL compared to a traditional SLL. We chose a rectangular beam with a fixed length of 100 mm and a width of 20 mm was used as the base of the SLL as this matched the 2-D projection of the elastomer pockets in a Pneu-net. We chose PA-6 as the base material because it is significantly stiffer than Ecoflex 00-30, has favorable elasticity properties, is easy to manufacture into complex shapes, and had similar properties as PLA which was used to fabricate the TR-SLL.

To understand the in-plane and torsional performance of a standard SLL, we analyzed the design using finite element analysis (FEA). We varied the thickness of the SLL and compared the in-plane bending and angular displacement. In-plane deformations are important as they allow a large range of objects to be grasped and can be used to show the energy efficiency of a design. For a given pressure, a design that bends more in the plane will use less energy to deform the structure, resulting in larger normal forces applied. Torsional deflection is important because a major failure mode for soft gripper not being able to lift an object is due to twisting of the grasp. Additionally, reduced torsional deflection allows for a better reasoning over where objects are in the grasp.

The data from the FEA can see seen in Table 5.1. We can see increases in in-plane and angular displacement as the SLL thickness is decreased. The performance ratio of in-plane displacement over angular displacement also improves as thickness decreases. We apply a moment that is an order of magnitude smaller than the moment applied to the TR-SLL due to its reduced torsional stiffness.

4.5.3 Simulation of Torsion Resistant Layer (TR-SLL)

Our next step was to analyze the design space of the TR-SLL. The main design parameter for the TR-SLL was the angle α between the base and the side of the triangle. We fixed the length of the TR-SLL to be the length of the SLL (100mm) from the reference design. Because our design relies on having complete triangles, this discritizes our search space to be angles that result in integer numbers of triangles along the length of the TR-SLL. The number of triangles varied from two to eighty. The thirty triangle configuration can be seen in Fig. 5.3. We fixed the height of each triangle to be 10% the major dimension (100mm), plus 2mm for bonding a gripping layer to the end of the TR-SLL (total 12mm). This was chosen as a reasonable value to search the design space without significantly increasing the volume of the gripper. By keeping this value small, we enable easy retrofitting onto grippers already using Pneu-nets.

In-plane and torsional bending conditions were simulated using Ansys Mechanical 2022.

Table 4.1: Simulated In-Plane Deformation and Angular Displacement for Simple Strain Limiting Layer (SLL).

Thickness [mm]	In-Plane Displacement (F = 0.01 N) [mm]	Angular Displacement (M = 0.5 N mm) [degrees]
0.3	64.85	32.89
0.4	27.38	15.36
0.5	14.02	8.02
0.6	8.11	4.70
0.7	5.11	2.98
0.8	3.42	2.01
0.9	2.41	1.43
1.0	1.75	1.03

PA-6 was used as the model material as its properties are similar to the PLA used in the printed TR-SLL. For the bending test, one end of the skeleton was fixed and an in-plane bending force of 0.01N was applied to the other edge of the beam. This roughly simulates the condition that occurs when the air chambers are pressurized.

The in-plane deformation starts high at two triangles and then drops to a minimum at seven triangles before rising as triangle count increases. Around thirty triangles, the slope of the curve flattens considerably. The seven triangle design is close to an equilateral triangle and as suggested by statics, is best able to resist deformations. A similar trend holds for the angular displacement plot. The two triangle design results in a local maxima that drops to a minima with the five triangle design before continuing to rise as triangle count increases. Again, as predicted by statics, designs around the equilateral triangle best resist deformations.

Using linear elastic strain energy theory, we can compare the rotational stiffness of each

of the beams following:

$$\kappa = \frac{M}{\theta} \tag{4.7}$$

where κ is the rotational stiffness, M is the applied moment, and θ is the angular displacement. The values for the 0.4mm SLL in Table 5.1 result in a stiffness of 1.9Nmm while the values from Fig. 5.4 result in 265.5Nmm for the thirty triangle TR-SLL and 366.6Nmm for the two triangle TR-SLL. The inclusion of triangles to the SLL has a dramatic impact on torsional resistance. The difference between number of triangles is marginal on bending stiffness relative to the performance improvement without triangles. We choose to design a gripper using the maximal number of triangles to reduce stress concentration within the structure. However due to manufacturing limitations, the greatest number of triangles that could be manufactured over the span was the thirty triangle design. For systems that require the maximum in-plane deformations, the two-triangle design would be better. If maximal resistance to twisting is required, the five-triangle design is the best configuration. However, the large stress concentrations of the low triangle designs would likely limit their life due to fatigue.

The in-plane deformation value for each configuration was plotted against the corresponding number of triangles (T_n) that were present in the SLL, and the results are shown in Fig. 5.4 (a). The same setup was used for simulating torsion, and a bending moment of 5Nmm was applied to the free end of the TR-SLL as shown in Fig. 5.3, and the corresponding results are shown in Fig. 5.4 (b). The angle (β) between line A and line C was calculated using Eq. 5.10 as shown below.

$$\beta = \sin^{-1}\left(\frac{BC}{\sqrt{(AB)^2 + (BC)^2}}\right) \tag{4.8}$$

where, AB is the distance from the center to the edge, BC is the linear displacement in vertical direction, β is the angle between line AB and AC.

In-plane deformations reach 20.7mm and 15.6mm for the two and thirty triangles, with

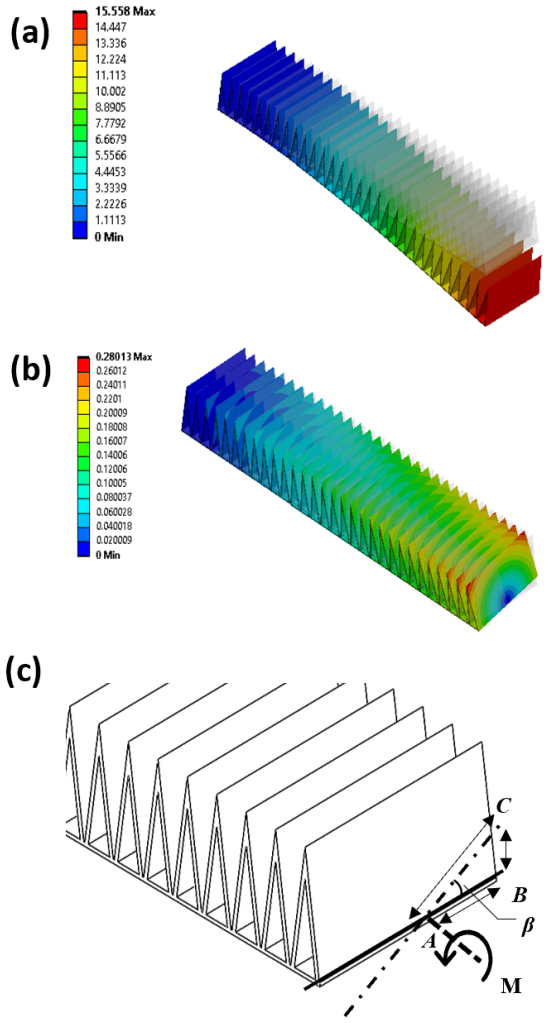

Figure 4.3: FEA results showing the displacement contour of (a) in-plane bending simulation & (b) torsion test, and (c) torsional bending setup for simulated angle measurement. A moment M is applied along the longitudinal axis of the TR-SLL. Line AB is deformed to line AC forming the angle, β, which is calculated using Eq. 5.10. The number of triangles was varied across a span of 100mm resulting in different triangle widths.

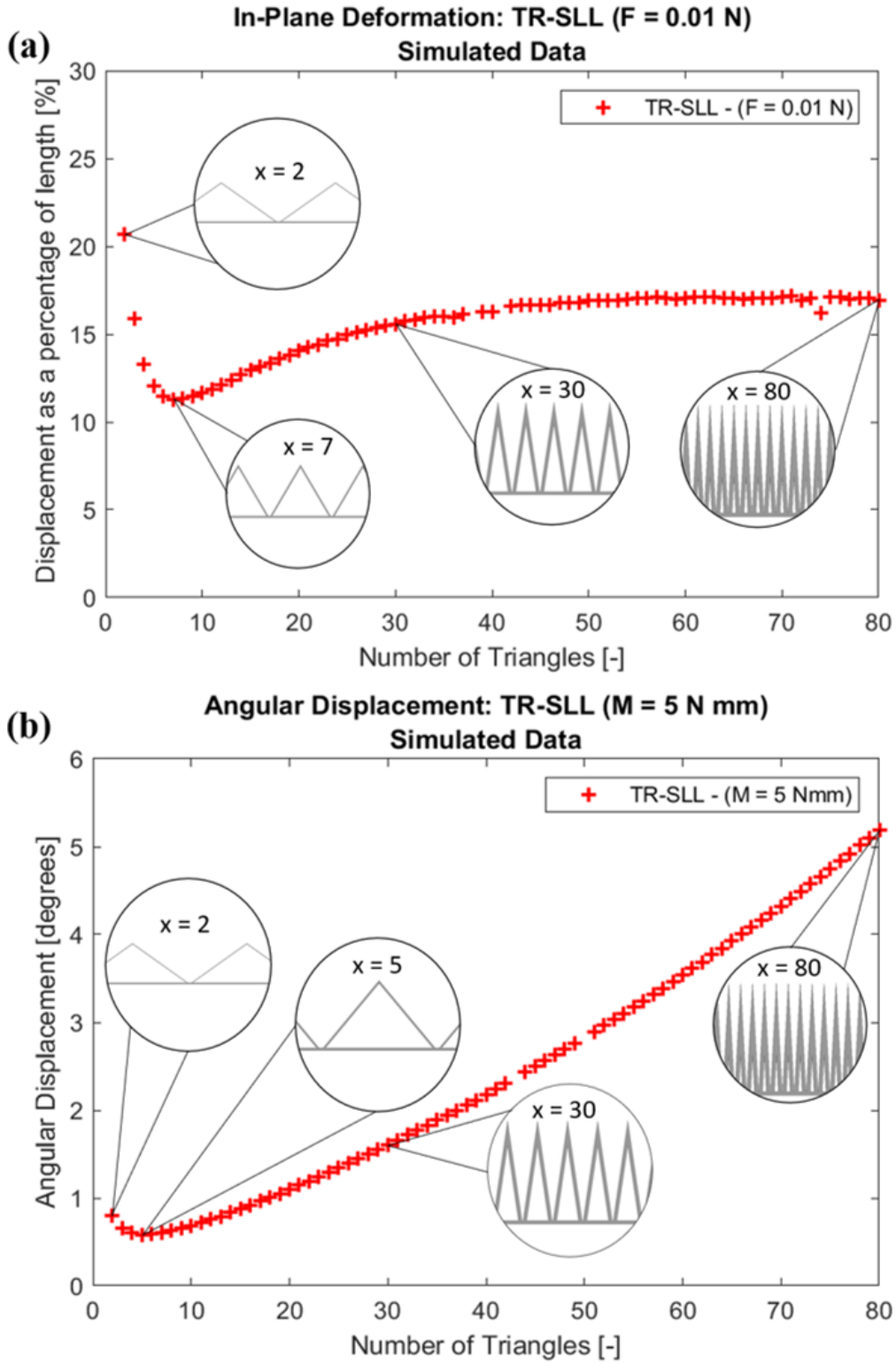

Figure 4.4: Plot of In-plane displacement (a) and Angular displacement (b) as a function of number of triangles in the Strain Limiting Layer. In (a), we see in-plane deformations from an applied load of 0.01N and in (b), we see the angular displacement from a 5Nmm torque. Both plots follow a swoosh pattern with local maxima at the extreme ends of the range (two

a minimum at 11.3mm for the seven triangle case. The torsion test sees values of 0.8° and 1.6° for two and thirty triangles, with a minimum of 0.58° for the five triangle design. The best ratio of in-plane to out-of-plane performance is the two triangle TR-SLL. However, this results in a large stress concentration, limiting cycle life. If a low cycle count is being considered, the two triangle design is the best performing. However for repeated cycles the thirty triangle design is superior. For our gripper we chose the thirty triangle design because it had strong performance while distributing stresses well. It was also the maximal number of triangles on a SLL that could be repeatably manufactured using a standard 3D printer.

4.5.4 Fabrication of TR-SLL Gripper

The process for the TR-SLL gripper can be seen in Fig. 4.5. The casting process for the TR-SLL gripper and the benchmark gripper follow the process detailed in the Soft Robotics Toolkit [76] with the following modifications made. Mixing was done manually following manufacturer instructions. For both grippers, we perform an additional degassing phase after mixing the two Ecoflex 00-30 components until bubble transport stops visually. For the insertion of the TR-SLL, we allow the ecoflex to set for 30 minutes before adding the TR-SLL to ensure the proper set height of 2mm for the TR-SLL.

4.6 Results - Experimental Comparison of TR-SLL and Standard Pneu-net

In this section, we compare our TR-SLL gripper against the benchmark Pneu-net gripper from the Soft Robotics Toolkit [76]. We test both grippers in a bending characterization test. They are tested in plane and out of plane unloaded and with a weight at the distal tip. This simulates the performance of the grippers grabbing an object. We also conduct an extension test on both sets of grippers. They grab a cylinder, which is then pulled out of their grasp. This demonstrates the maximum payload capacity for the grippers and can be used to find the effective stiffness of the grippers and their torsional spring constant. Finally, the TR-SLL gripper is tested on a subset of the YCB dataset. The subset only features objects larger than the maximum payload capacity of a standard Pneu-net gripper. We show success on

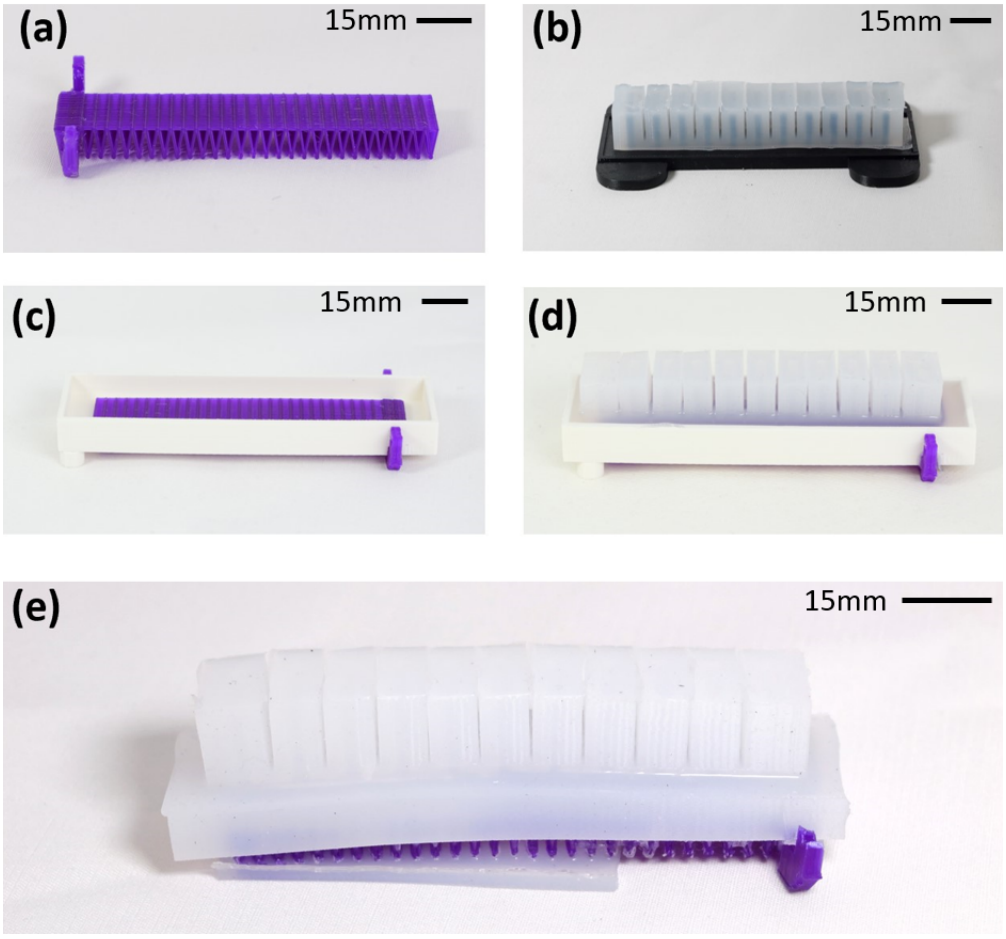

Figure 4.5: This figure shows the casting process for a TR-SLL gripper. First, (a), we print the 100mm long torsionally resistant Layer (TR-SLL), then in (b), we cast the Pneu-net chambers out of Ecoflex 00-30 following instructions from the Soft Robotics Toolkit. In (c), we insert the TR-SLL into the sacrificial mold and mix Ecoflex. After 25 minutes, we pour until 2mm above the TR-SLL. In (d), we add the Pneu-net chambers and seal them with a thin layer of Ecoflex. Finally in (e), we remove the TR-SLL gripper from the mold, place it spikes side down in a 1mm thick layer of Ecoflex in the Pneu-nets Strain Limiting Layer mold, cure it, and remove.

the test set and only fail on one object within the theoretical payload capacity predicted in Eq. 5.5.

4.6.1 Bend Characterization

We evaluate in-plane bending and resistance to torsional deformations for our gripper. Better in-plane performance means that more actuation energy goes into conforming to the object being gripped as less energy is used to deform the structure. Resistance to torsional deformations determines one of the main failure modes for soft grippers. Additionally, smaller torsional deformations can allow a more precise understanding of where grasped objects are. We compare our TR-SLL gripper to the benchmark Pneu-net in terms of bending characterization for both unloaded and loaded tests.

A series of optical tracking tests were done to determine the tip bending angle of our TR-SLL gripper and the benchmark Pneu-net gripper, as shown in Fig. 4.7. The XY plane was defined as normal to the robot flange frame, in-plane deformations occurred in the YZ plane, and out-of-plane deformations occurred in the XZ plane. The grippers are evaluated with no load, and with a 50.5g mass positioned between the furthest two air chambers. Pressures ranged from 4kPa to 10kPa and the data can be seen in Fig. 4.6.

We determined bend angles using optical tracking data from markers on the distal tip of the gripper as shown in Fig. 4.7. In-plane bending was computed in the Y-Z plane, while out of plane bending was computed in the X-Z plane using the inverse tangent function. We recorded data using an OptiTrack motion capture system using Flex 13 cameras. The system was allowed to come to steady state before the data was recorded. The last 120 data points were averaged and a standard deviation determined.

Here we look at the performance of each gripper during testing. The benchmark gripper begins slightly open when no pressure is applied. It curves until the tip reaches the base of the robot flange as pressure is increased to 10 kPa. There is a controlled change in gripper position until 7kPa when the gripper begins rapidly bending, reaching a maximum bend angle of $99.4 \pm 0.50°$. When the 50.5g mass is added to the gripper, it bends outwards in

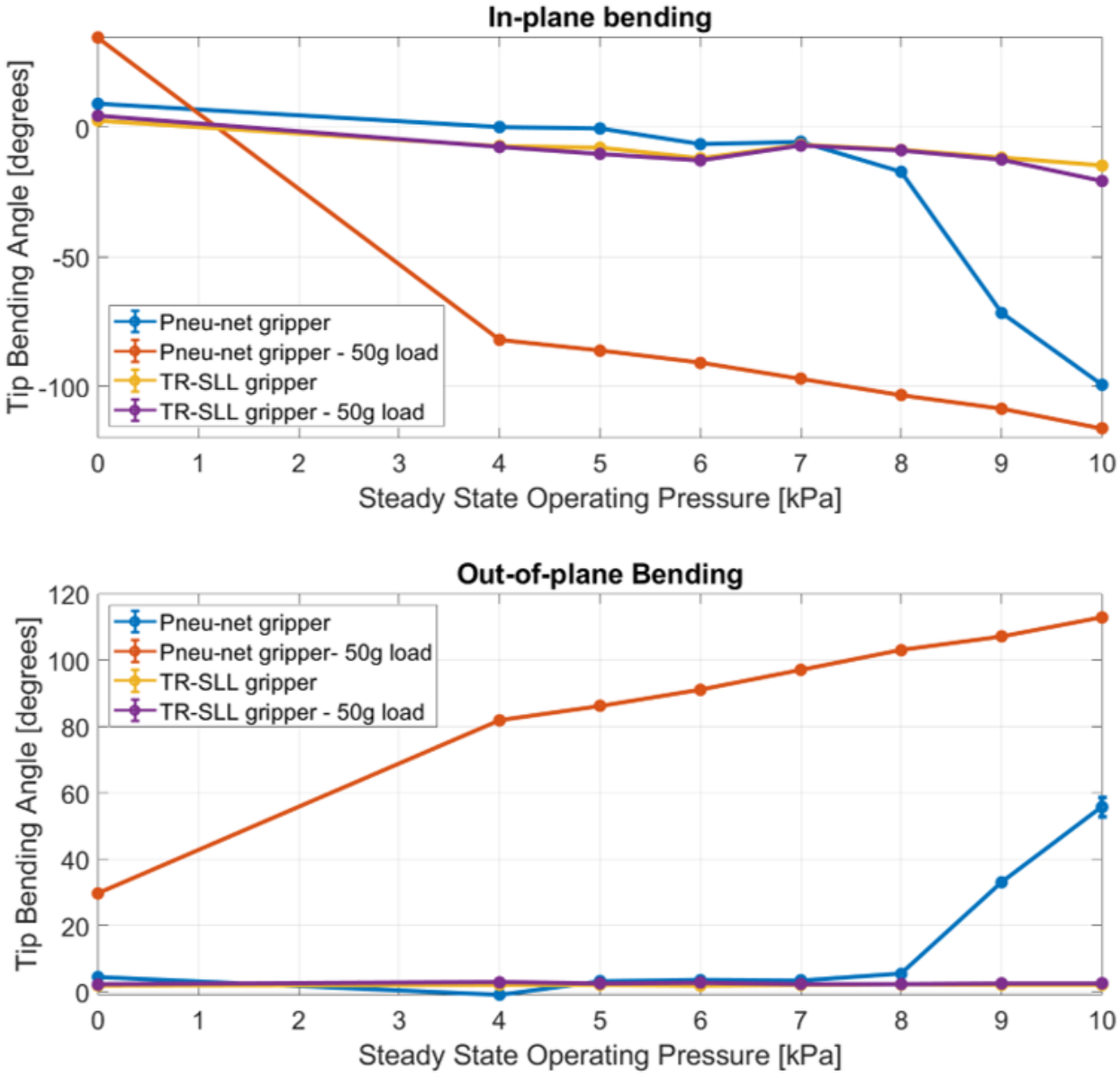

Figure 4.6: Tip bending angle for the TR-SLL and benchmark Pneu-net grippers are shown. Data are presented with and without the addition of a point load. The TR-SLL does an excellent job of reducing out-of-plane deformations. The benchmark gripper showed much larger deformations both in- and out-of-plane. The higher torsional stiffness of the TR-SLL gripper results in better understanding of where picked objects are and in a larger payload capacity.

negative Y by $34.6 \pm 0.12°$. Once the gripper was pressurized to 4kPa, it closed completely to $82.1 \pm 0.12°$ where it finally reached a distal tip bend angle of $116.1 \pm 0.13°$. In contrast, the TR-SLL gripper maintained strong positional control at the cost of large tip bending angles. The unloaded TR-SLL gripper started at $-2.59 \pm 0.12°$ and bent in to $14.8 \pm 0.13°$. When loaded, in-plane behavior changes little but a larger range of tip bend angles are observed. The loaded gripper starts at $-4.45 \pm 0.12°$ and increases to $20.8 \pm 0.12°$ at 10kPa.

Looking at relative in-plane performance of the grippers, we see the TR-SLL gripper do a better job of maintaining its position at rest. This is especially true when the gripper is loaded as the TR-SLL does not meaningfully change tip angle, whereas the benchmark Pneu-net gripper moves more than 30° when the weight is added to the distal tip.

When looking at out-of-plane performance, the TR-SLL gripper is dramatically more stable than the benchmark gripper. When unloaded, the benchmark gripper starts pointing $4.48 \pm .13°$ downwards and maintains small out-of-plane deformations until an internal pressure of 8kPa is achieved. After that point, out-of-plane performance degrades rapidly, resulting in a maximum out-of-plane tip deflection of $55.7 \pm 2.9°$. When loaded however, the benchmark Pneu-net gripper performed even worse. It started off with a bend of $29.7 \pm .12°$. Once pressure was applied, the out-of-plane deformations got worse, resulting in $81.8 \pm .12°$ at 4kPa. At maximum pressure, the out-of-plane tip angle reached a staggering angle of $112.8 \pm .23°$.

The TR-SLL gripper held up well to out-of-plane deformations. At rest, we see a deformation of $1.89 \pm .12°$. As pressure is applied, deformations hover between 1.8° and 2.2°, reaching a maximum at 8kPa of $2.21 \pm .13°$. Once the 50.5g point mass is added to the gripper, out of plane displacements grow but only slightly. The TR-SLL gripper starts at $2.21 \pm .13°$, and reaches a maximum deformation at 4kPa with a bend of $2.86 \pm .12°$. At 10kPa, the out of plane deformations drop to $2.58 \pm .12°$.

The unloaded TR-SLL reduced deformations by 57.8% at rest. When maximally pressurized, the TR-SLL reduced out-of-plane deformations by 96.1%. When loaded with the 50.5g point mass, the TR-SLL reduces deformations by 92.5% at rest and by 97.7% at maximal

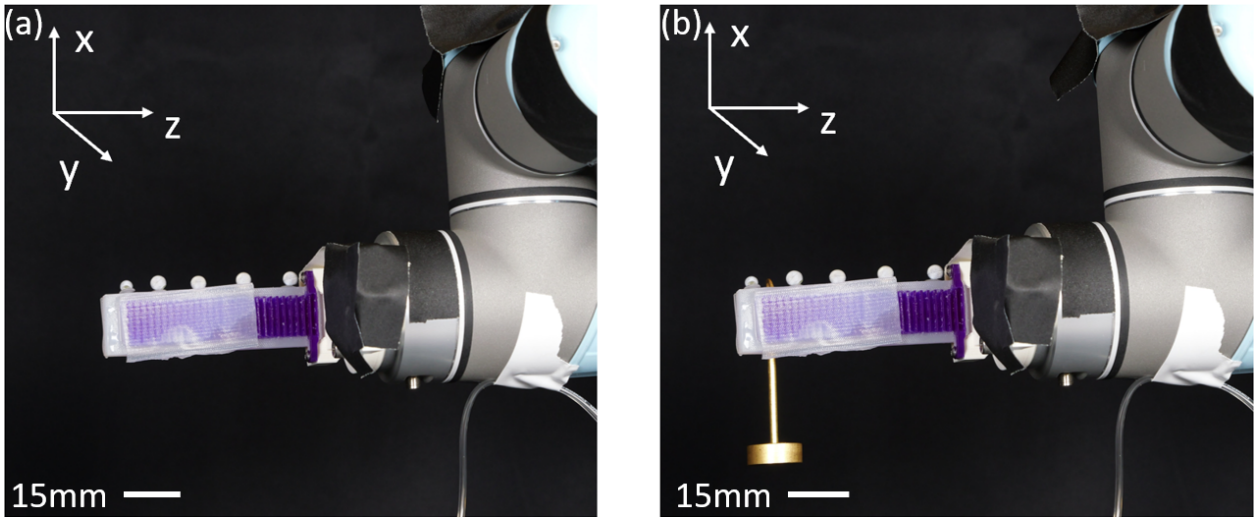

Figure 4.7: Test setup for Optitrack tip characterization. The TR-SLL gripper is mounted to the robot arm in a) and shown with TR-SLL a weight of 50 grams in b). The weight was placed between the furthest air chambers, with the mass resting on the silicone forming the SLL. The weight shows how the gripper behaves under loading. We track the deformation of the gripper as steady state pressure is changed using Optitrack markers. This characterization can be used to model the deformation of the TR-SLL gripper as a function of pressure and to understand how lifting an object near the tip of the gripper effects performance. Positive in-plane tip bending is defined in z direction and positive out-of-plane bending is defined in negative Y direction.

actuation. This matches closely with our simulated out of plane bending reduction of 94.7% for the rigid Strain Limiting Layers.

4.6.2 Grip Slip Force Characterization

We compared the grip strength for a TR-SLL gripper and the benchmark Pneu-net gripper. This test demonstrates the minimum of the three common antipodal failure modes for soft grippers; slipping, twisting, and shearing. Data was gathered using an Instron 68SC-2 at

200Hz as can be seen in Fig. 5.8. The grippers were closed around a 90 mm diameter test cylinder made from VeroWhite on a Stratasys J750 Digital Anatomy printer. The diameter of the cylinder was matched to the distance between antipodal grippers. The grippers were mounted to a Universal Robotics UR-5 and pressurized to 10kPa. The cylinder was moved upwards at a rate of 10mm/s for 100 mm. The data from the experiment can be seen in Fig. 5.7. Our gripper shows much larger forces compared to the benchmark gripper reaching 3N compared to an eventual 1N. We also demonstrate a 7.8x increase in grasp stiffness at 1.8mm of extension. This shows that the TR-SLL gripper has a higher minimum for the three antipodal failure modes, and can lift larger payloads.

We can see a significant difference in performance of the TR-SLL and standard Pneu-net gripper in Fig. 5.8. A peak force of 3N was observed for the gripper with TR-SLL, while the benchmark gripper demonstrated a peak force of 1N. The TR-SLL gripper has a higher minimum value for the three common failure conditions for an antipodal grasp; slipping, twisting, and shearing. The TR-SLL gripper showed a much higher stiffness compared to the benchmark gripper. Over the first 1.8mm, the benchmark gripper had a stiffness of 152N/m while the TR-SLL gripper showed a stiffness of 1181N/m. By using the TR-SLL instead of the benchmark SLL, we demonstrate a 7.8x increase in grasp stiffness. A larger grip stiffness demonstrates a higher minimum antipodal grasp failure condition and can allow for better understanding of where objects are within the grasp.

4.6.3 YCB Object Grasping

We demonstrate the TR-SLL gripper's ability to pickup objects from the YCB object dataset [28]. We chose to limit our object selection to non-box objects larger than 100g and smaller than 300g. This was set as 100g is the maximum possible lifting force applied by the benchmark gripper and 300g was the limit for the TR-SLL gripper. Boxes were excluded due to their lack of compliance required for their grasp. From this set, we filtered out objects that did not fit between the TR-SLL grippers using the mount shown in Fig. 5.8. In total this left six objects in our test set as seen in Fig. 5.9. All objects were filled to match their

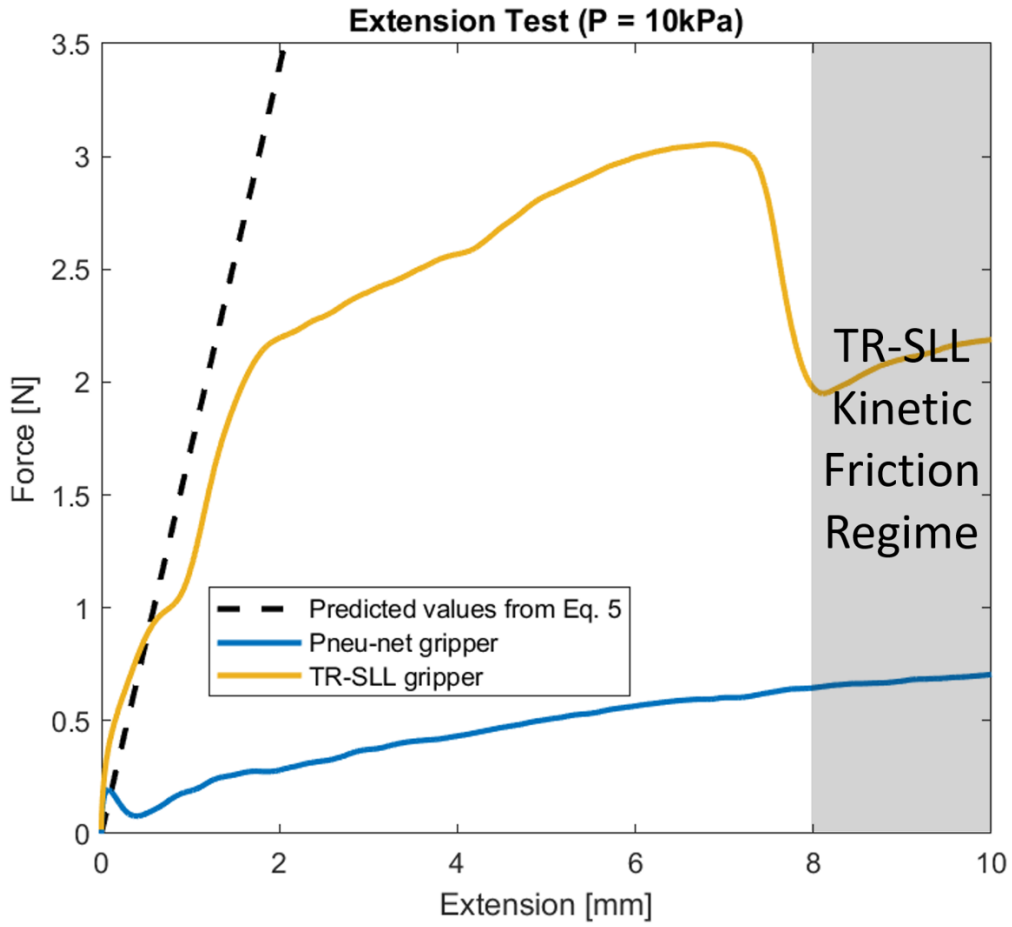

Figure 4.8: Data from a single extension test shows an increase in maximum force response for the TR-SLL gripper. The TR-SLL gripper demonstrates peaks of 3N grip force, compared to an eventual 1N from the benchmark gripper. As seen in our supplemental video, the Pneu-net gripper without a TR-SLL quickly slips due to insufficient torsional stiffness, resulting in a much lower gripper stiffness. At 1.8mm extension, the TR-SLL gripper demonstrates a 7.8x increase in effective grip stiffness. The larger grip stiffness demonstrates a higher minimum antipodal grasp failure condition and can allow for better understanding of an object's position when grasped.

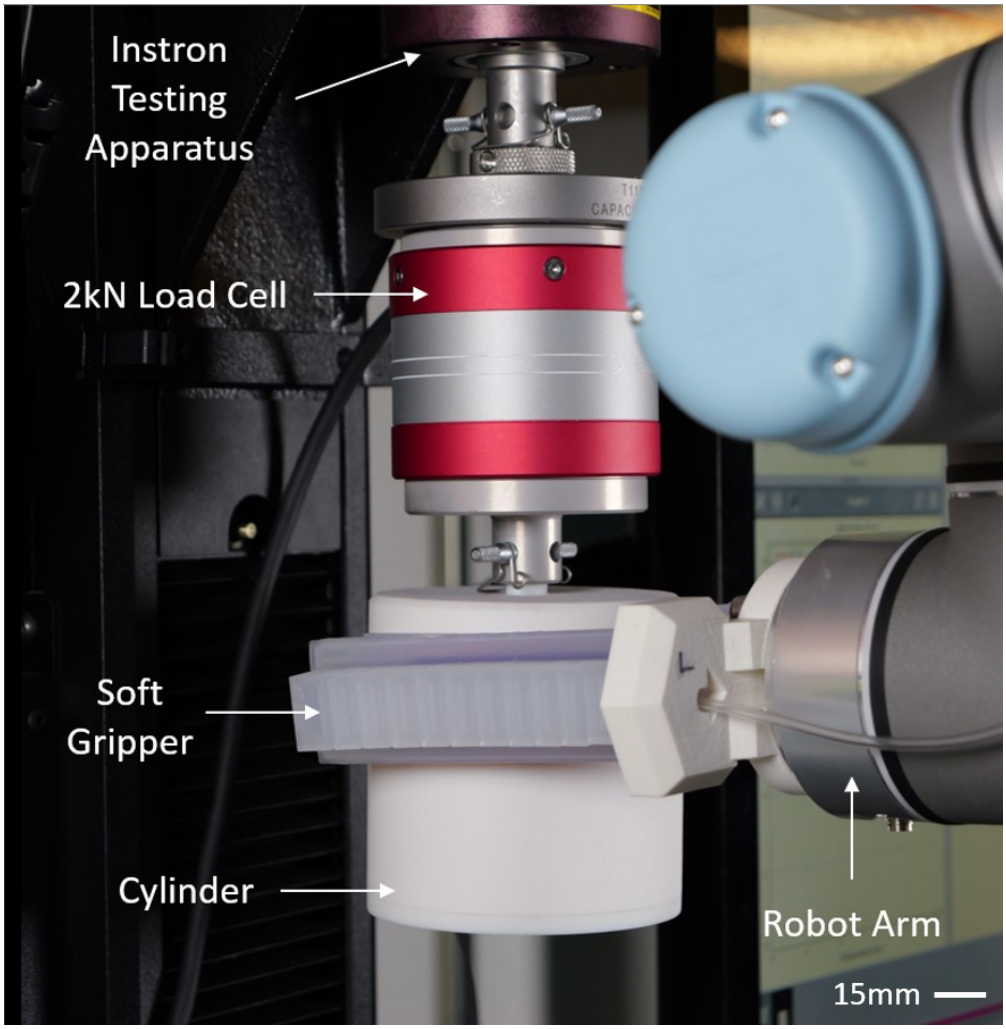

Figure 4.9: The Instron testing setup for gripper characterization. The two grippers are fixed to a UR5 robot arm. They are positioned to antipodially grasp a 3D Printed cylinder that is 90mm in diameter. The grippers are pressurized to 10 kPa before beginning the test. The Instron testing apparatus moves up and the force response is collected by the transducer. This demonstrates the minimum of the three common antipodal failure modes for soft grippers; slipping, twisting, and shearing.

weight and approximate mass distribution according to the data from [28].

We were able to successfully lift five of the objects, with two of the five being partial lifts. A successful lift is fully lifting the object off the ground and maintaining contact. A partial success is lifting the object but not maintaining contact. The objects the TR-SLL gripper successfully grasped were the Pringles can, the wine glass, and the mug. The partial successes were the tuna fish can and the baseball. The baseball slipped out of the grasp due to pitching backward. The tuna fish can slipped out due to roll. The TR-SLL gripper was unable to grasp the padlock due to it being too narrow to generate enough normal force. If the gripper mount were closer together, the TR-SLL gripper would have likely been able to lift the padlock.

We demonstrated a significant increase in capability for the TR-SLL gripper compared to the Pneu-net gripper. Not only did we show the addition of the TR-SLL increased normal force and torsional stiffness, but it translated to a greater capability set for Pneu-net grippers. This can enable their use on a wider variety of tasks and reduces a key limitation of their adoption.

4.7 Conclusion and Future Work

In this paper, we developed a torsion resistant strain limiting layer (TR-SLL) to increase payload capacity by increasing torsional resistance. A comprehensive design study was conducted using FEA simulations to understand the design landscape of triangulated beams. The number of triangles on a 100mm-long strain limiting layer was varied to characterize the performance of the TR-SLL in plane and out of plane. It was found that the overall change in angular displacement was small for all cases compared to no triangles. However, the TR-SLL with thirty triangles showed good in-plane bending characteristics and evenly distributed stresses along the length of the structure. A modified casting process was adopted to integrate the TR-SLL to a standard Pneu-net actuator, and extension and Optitrack tests were conducted to see the performance improvement over the standard Pneu-net actuator.

This work found that adding a torsion resistant strain limiting layer dramatically in-

Figure 4.10: This figure shows the YCB objects we evaluated the TR-SLL gripper against. All of the items were chosen to be above the maximum demonstrated capacity for the Pneu-net gripper so any objects grasped show added capability. Additionally we filtered to non-box objects that fit within the jaws of the TR-SLL gripper. Of these items, the TR-SLL lifted five items successfully, with two being partial successes. The only failure is the padlock.

creased torsional performance, reducing deformations by up to 97.7%. The addition of the TR-SLL allowed a standard Pneu-net gripper to pick up a 5kg dumbbell, maxing out the capacity of the robot arm it was installed on. The TR-SLL gripper was also tested on a subset of the YCB data set and successfully picked up all but one item, all of which were heavier than the maximum demonstrated payload capacity for a Pneu-net gripper without the TR-SLL. The TR-SLL gripper also demonstrated increased grasp stiffness by 7.8x the standard Pneu-net gripper. Future work for these TR-SLL grippers include sensorization and co-optimization of cast material properties with TR-SLL materials. Additionally, adding a variable gap between the TR-SLL gripping surfaces would allow them to lift a larger variety of objects. This work lays the foundation to easily incorporate TR-SLLs into existing soft robots and demonstrates additional payload capacity that is often lost due to torsional deflection in soft grippers.

Chapter 5

TORSION RESISTANT STRAIN LIMITING LAYERS ENABLE HIGH GRIP STRENGTH OF ELECTRICALLY-DRIVEN HANDED SHEARING AUXETIC GRIPPERS

5.1 Notice

Please note, this work is a part of a co-first author publication. Certain sub-chapters have been removed as they do not contribute towards this thesis. For access to these sub chapters, please wait for the work to be published.

5.2 Summary

Soft grippers have demonstrated a strong ability to successfully pick and manipulate many objects. A key limitation to their wider adoption is their inability to grasp larger payloads due to objects slipping out of grasps. We have overcome this limitation by introducing a torsionally rigid strain limiting layer (TR-SLL). This reduces out-of-plane bending while maintaining the gripper's softness and in-plane flexibility. We characterize the design space of the strain limiting layer and Handed Shearing Auxetic actuators for a soft gripper using simulation and experiment. We found that the use of our TR-SLL HSA gripper enabled pinch grasping of payloads over 1kg. We demonstrate a lifting capacity of 5 kg when loading using the TR-SLL. We also demonstrate a peak pinch grasp force of 5.8 N, and a peak planar caging force of 14.5 N. Finally, we test the TR-SLL gripper on a suite of 43 YCB objects. We show success on 37 objects demonstrating significant capabilities.

5.3 Introduction

Soft robotic fingers have focused on emulating the ability of human and other biotas compliance when bending [153]. However, the key to human's remarkable grip is that our fingers can simultaneously bend while resisting torsion and lateral loading. People rely on a rigid skeleton with discrete joints to provides this selective compliance. Here we show how a torsion resistant strain limiting layer (TR-SLL) can provides soft robotic grippers with this same ability without a discrete skeleton.

The bending of a finger defines a plane. In-plane bending and compliance is desired in a gripper. Its what allows a finger to conform to an object while still applying a normal force. Movement normal to this plane, or out-of-plane deformation, leads to grasp failures [155,176] and localization uncertainty [133]. This is especially true for antipodal or planar caging grasping where two fingers interact with and object.

Soft robotic grippers inability to resist out-of-plane loads has been identified as a major limiter in soft robotic systems [85,173]. With caging or parallel-to-gravity lifts, soft robotic systems have been able to lift car tires and dumbbells [106–108]. However, when a gripper is perpendicular to the gravity field, or when large moments are present, soft grippers lose their grasp from deformations and twists. This limits their ability to manipulate meaningful payloads.

This work shows how a torsion resistant strain limiting layer (TR-SLL) integrated into an electrically-driven handed shearing auxetic gripper can exceed payloads of 1 kg when grasping using the fingers as demonstrated in Fig. B.1(a), and increase the lifting capacity to 5 kg when loading through the continuous skeleton as shown in Fig. B.1(b).

The most common place in soft robotics where strain limiting layers appear is in Pneunets [124]. The standard Pneunet uses a simple rectangular beam as the strain limiting layer (SLL). Rectangular cross sections have low second moments of inertia in one direction, allowing them to bend in the thin direction. While in theory, this would make them able to resist deformations along their thick direction, in practice, these structures have a low

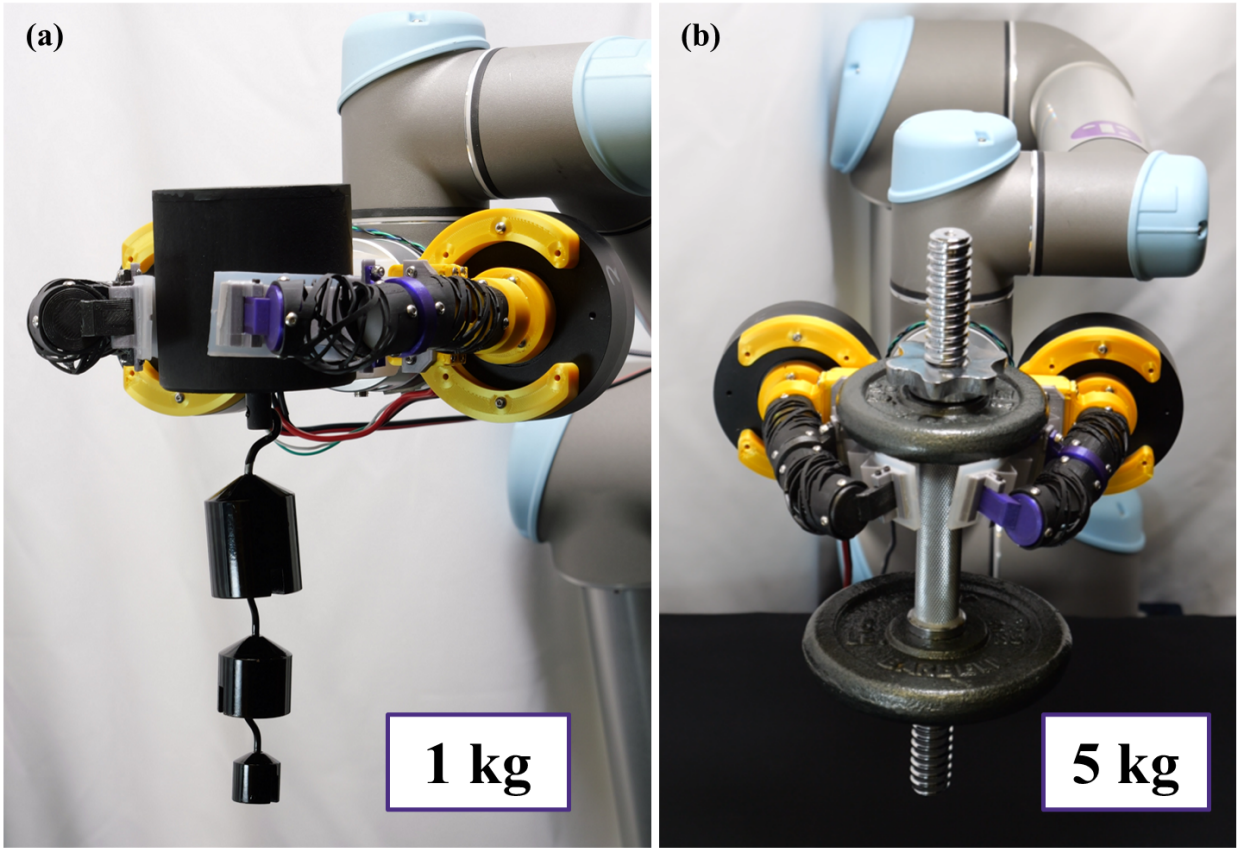

Figure 5.1: We create a new Torsion Resistant Strain Limiting Layer (TR-SLL) that can be added to an existing soft gripper. It increases the gripper's resistance to torsion, allowing the gripper to lift larger payloads. Additionally, we can load the skeleton of the TR-SLL directly, dramatically increasing lifting capacity. Here we create a Handed Shearing Auxetic (HSA)-based gripper using the TR-SLL and two quasi direct drive motors. in a) We show the HSA-based TR-SLL gripper lifting a 1 kg mass using a planar caging grasp. In b) we lift a 5 kg dumbbell using the skeleton from the TR-SLL, the maximum payload capacity of the UR5 robot arm.

resistance to torsion. This causes any out-of-plane loading to generate a twist in the SLL and gripper.

For electrically-driven handed shearing auxetic grippers, a torque must be resisted to generate extension or bending of the HSA. A strain limiting layer has typically been ommited in favor of a second, opposite handed HSA [39, 41]. In another work, rigid cable elements in addition to a second HSA are used to stiffen the system to undesired bending modes [38]. The second HSA increases the moment of inertia, reducing non-planar bending modes. However, this does not reduce out-of-plane deformations as much as the TR-SLL work presented here. These works also demonstrate lower payload capacities when looking at solely HSA-based gripping. Additionally, these systems need a non-rotating grasping surface to be added to the gripper whereas the TR-SLL in this work serves both purposes.

Several strategies have emerged for improving the out-of-plane performance of soft grippers through the SLL. One approach focuses on changing the material distribution by using multi-material topology optimization [190]. Another approach discritizes the SLL and inserts hinges to allow a thicker material to still bend [114]. The first still experiences large out-of-plane deformations while demonstrating smaller increases in torsional stiffness. The second uses hinge-based strain limiting layers (SLL) which can reduce the structures ability to conform to objects compared to the continous design presented here.

We focus on using advancements from the field of compliant mechanisms to change the geometry of the SLL. We use triangulated beams as the torsion resistant strain limiting layer (TR-SLL) of Pneu-net. These triangulated beams resist torsion but allow bending on planar and spherical surfaces [132, 150]. While one might expect the triangles along the beam to localize the deformation to interfaces between triangles, the structures deform over their entire length, with all sides of the triangle deforming when bent. Rhombus and honeycomb cross-sections have been integrated into robots using pneumatic air bladders [70,86] and tendons [35] however both systems demonstrate smaller payloads than this work. The triangularized beams act as a continuum structure with enhanced stiffness to out-of-plane bending and torsion. This behaviour has a close analog with the human hand in the

tendons and bones, however this work produces a continuous skeleton instead of discretized elements.

We integrate the TR-SLLs into electrically-driven handed shearing auxetic grippers and provide a step-by-step guide for integrating the TR-SLLs. Next, we perform a parametric sweep on the TR-SLLs to provide a design guide. We found that triangles close to equilateral best resisted torsion. We found in plane stress concentrations decreased with triangle count while stress from torsion followed that trend above 10 triangles per 100mm span. We tested the integrated gripper on a cylindrical pull test and found that the addition of the TR-SLL enabled grip forces above 5N for pinch grasps and above 14N for caging grasps. Finally, we tested the gripper by picking up a weighted structure entirely using the sides of the gripper. As seen in Fig. B.1, the TR-SLL gripper can pick up a 5 kg weight (the max capacity of the UR5) using lateral loading.

In this paper we:

- Model key parameters to understand a torsion resistant strain limiting layer
- Analyze the design space of handed shearing auxetics through mechanical characterization
- Integrate the TR-SLL with handed shearing auxetics to build a soft gripper and demonstrate its enhanced payload capacity

5.4 Background

Soft robotics researchers have attempted to improve the out-of-plane performance of soft grippers using several techniques. One method is to redesign the gripper as a whole. This can involve putting a skeleton around the entire gripper [155]. However, this requires significantly more input energy to reach the same normal force output and demonstrates smaller lifting capacity. Another method involves optimizing the design of individual cells to improve torsion resistance [173].

Active strain limiting layers are another area of research. Many of these change their SLL stiffness through phase change [201], jamming chain, [87] or through the thermoelectric properties of Field's metal [26, 65] or by heating hydrogels, causing them to swell [188]. Additionally, work has been done to use jamming to increase a gripper's ability to grasp objects and increase out-of-plane grip strength [45].

Our solution allows a simple passive SLL made from a single material to be easily integrated into existing soft gripper designs. It demonstrates a large torsional spring constant and high in-plane compliance. It can be made with a low cost 3D printer and can be integrated into a variety of different soft gripper designs.

5.5 Derivation of the effect of Torsion on Antipodal Gripping for Soft Bodies

In this section we characterize the three common failure modes for soft grippers. We introduce the idea that deformations from moments are often a dominant term, and then map equations to describe this failure mode.

Antipodal gripping is a widespread application for soft robotic grippers. It involves picking up an object through two opposite points. There are three common limits to a soft grippers ability to perform an antipodal grasp; insufficient normal force, slippage due to torsional deformation, and shearing of the soft layer. All three of these modes as well as an example antipodal grasp can be seen in Fig. 5.2. The minimum of these three modes govern the payload capacity for an antipodally lifted object. If the payload minimum is governed by insufficent normal force, the force a gripper can lift is shown in Eq. 5.1.

$$F_{static} = \mu F_n \tag{5.1}$$

where F_{static} is the maximum force a gripper can lift, μ is the coefficient of static friction, and F_n is the normal force the gripper applies as shown in Fig. 5.2. If instead the gripper is just at the limit of slip from twisting, we get:

$$M = F_g r \tag{5.2}$$

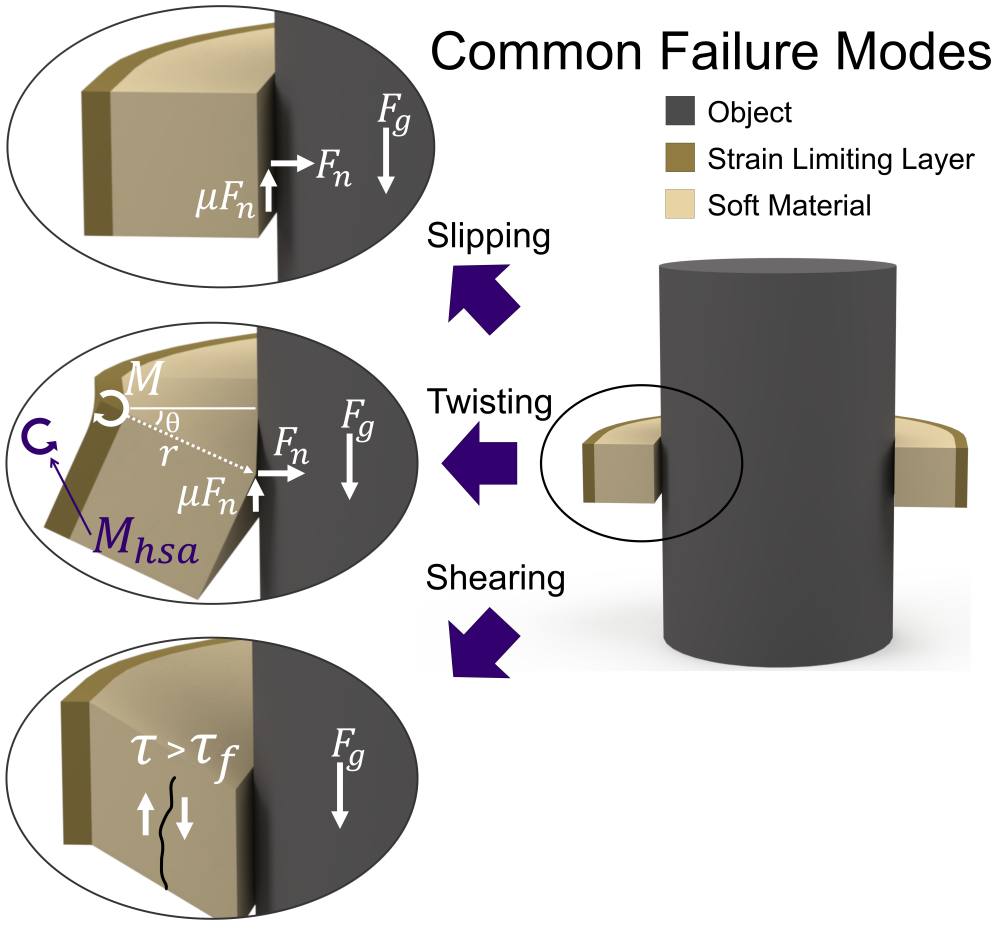

Figure 5.2: We demonstrate the common failure modes for soft robotic grasping. On the right we can see a simplified gripper grabbing a cylinder using an antipodal grasp. Only the Strain Limiting Layer and soft gripping material between the SLL and object is shown (not to scale). On the left, three common failure modes are shown; slipping due to low normal forces, twisting due to torsional deformation in the SLL, and shearing of the soft material. The maximum payload capacity for a this gripper is governed by the minimum of the set of these conditions. By understanding these limits, we can better inform gripper design. By including the TR-SLL, we dramatically increase our soft grippers resistance to twist. This allows it to lift larger payloads while having a better understanding of where the object is in our grasp.

$$M = \kappa\theta \tag{5.3}$$

where M is the moment on the SLL, F_g is the gravitational force from the object, r is the distance from the neutral axis of the gripper to the object, κ is the torsional spring constant from twisting failure, and θ is the angle of twist relative to the normal force. These can be seen labeled in the twisting failure modes in Fig. 5.2. If we assume there is some small vertical deformation x as the gripper is loaded but no slip or rolling occur, we get Eq. 5.4.

$$x = r\theta \tag{5.4}$$

Combining Eq. 5.2, Eq. 5.3, and Eq. 5.4 we can solve for F_g as a function of x:

$$F_g = \frac{\kappa}{r_t^2}x \tag{5.5}$$

Where $\frac{\kappa}{r_t^2}$ is the effective stiffness of the TR-SLL. We can use the net torque requirement from the HSA to further enhance F_g. We intentionally choose a HSA chirality that resists objects slipping due to the gravity field, adding to the net force supported.

$$F_g = \frac{\kappa}{r_t^2}x + \frac{c_\tau}{r_h}\varphi \tag{5.6}$$

where c_τ is the torsional spring constant as presented in [63], r_h is the distance from the center of the HSA to the grasping surface, and φ which is the angle of twist of the HSA from the motor. As shown in Fig. 5.2, the HSA's contribution is represented with the opposite direction torque M_{hsa} where the second half of Eq. 5.6 is equal to it.

$$M_{hsa} = \frac{c_\tau}{r_h}\varphi \tag{5.7}$$

Shearing of the soft gripping material can be another concern and is defined when:

$$\tau > \tau_f \tag{5.8}$$

where τ is the length of the shear vector in the material and τ_f is the shear fracture of the material. For this study delamination was seen for high mass objects.

Together, the minimum force value from Eq. 5.1, Eq. 5.6, and Eq. 5.8 govern the payload capacity of a soft gripper performing an anti-podal pick on a simple object. Since soft grippers often demonstrate out-of-plane deformation as a common failure mode, this work looks to Eq. 5.6 as a way to increase the payload capacity of soft grippers. This paper achieves this through the creation of a continuously-deformable torsion resistant strain limiting layer.

5.6 Design of Torsion Resistant Strain Limiting Layer

This section describes the design of our torsion-resistant strain limiting layer. First, it explores the design space for a flat strain limiting layer and evaluates them based on their bending and torsional stiffness as a function of thickness. Then, we explore the design space of the TR-SLL using FEA simulations by varying the number of triangles present over the length from two to eighty. We look at torsional stiffness, bending stiffness, as well as the average stresses present in the TR-SLL. Finally, we use the simulation results to inform which TR-SLL design to instantiate in the real world.

5.6.1 Flat Strain Limiting Layers

The first design parameter to be considered to explore the design space of flat strain limiting layers is the thickness. We chose a flat rectangular beam with a fixed length of 102 mm, and a width of 25 mm was used as the base of the SLL to evaluate the angular and in-plane deformation for different thicknesses. This dimension was chosen as it is the standard strain limiting design for soft grippers. We chose PA-6 as the base material because it has favorable elastic properties, is easy to manufacture into complex shapes, is well documented in simulation, and had similar properties as PLA which was used to fabricate the TR-SLL.

To understand the in-plane and torsional performance of the flat SLL, we analyzed the design using finite element analysis (FEA). We varied the thickness of the flat SLL and compared the torsional and bending stiffness. The stiffness values were calculated using the

Table 5.1: Simulated Torsional and Bending Stiffness for the Flat Strain Limiting Layer (SLL). Fixed dimensions are 102×25 ($l \times w$) in mm.

Thickness [mm]	Torsional Stiffness [Nmm/rad] (M = 0.5 Nmm)	Bending Stiffness [N/mm] (F = 0.01 N) $\times 10^{-3}$
0.3	1.04	0.23
0.4	2.30	0.47
0.5	4.44	0.87
0.6	7.62	1.47
0.7	12.05	2.23
0.8	17.93	3.46
0.9	25.46	4.93
1.0	34.81	6.67

angular and in-plane deformation from the simulation. Low In-plane or bending stiffness is important as it allows less energy to be expended on complying to the desired shape. High torsional stiffness is important because a major failure mode for soft gripper not being able to lift an object is due to twisting of the grasp. Large values of torsional stiffness can cause the grasp failure condition to switch from twisting to a lack of normal force or shearing of the soft material. Additionally, high torsional stiffness allows for better reasoning over where objects are in the grasp.

The data from the FEA analysis of the flat strain limiting layer can see seen in Table 5.1. We can see that torsional and bending stiffness increase as the SLL thickness is increased. The performance ratio of in-plane displacement over angular displacement also improves as thickness decreases. We apply a moment that is an order of magnitude smaller than the moment applied to the TR-SLL due to its reduced torsional stiffness, and to achieve reasonable deformation for the flat SLL.

5.6.2 Simulation of Torsion-Resistant Layer Strain Limiting Layer (TR-SLL)

The next step is to analyze the design space of the TR-SLL. We select a number of triangles as a parameter to explore the design space. We fixed the length of the TR-SLL base to be equal to 102 mm and the height to be 12 mm. 12 mm was chosen as a reasonable value to search the design space without significantly increasing the volume of the gripper, and to easily retrofit onto pre-existing works. In the 102 mm long base, we included a 1-mm long extension at the ends of the TR-SLL to ensure proper meshing around the area where the triangles meet the base. This gives 100 mm for complete triangles to be generated over. Because our design relies on having complete triangles, this discritizes our search space to be angles that result in integer numbers of triangles along the length of the TR-SLL. The number of triangles was varied from two to eighty. Examples of three such configurations can be seen in Fig. 5.4. Due to manufacturing limitations, the smallest realizable beam thickness as tested was 0.4 mm. This was used for the thickness of the triangles, however 0.8 mm (double the realizable thickness) was used as this provided a continuous path for the 3D printer nozzle to follow. Alternative manufacturing methods like resin printing or casting could eliminate this restriction.

In-plane and torsional bending conditions were simulated using Ansys Mechanical 2022 FEA software. Similar to the flat SLL, PA-6 was used as the model material. A tetrahedral mesh with an element size of 0.2 mm was chosen to achieve consistent results for all the design configurations. For out-of-plane twisting, one end of the TR-SLL was fixed, and a bending moment of 5 Nmm was applied to the free end of the beam. This simulates the twisting failure condition that occurs during object grasping. Similarly, for in-plane bending simulation, one end of the TR-SLL was fixed and a force of 0.01 N was applied to the free edge of the beam. This simulates the condition that occurs when the HSAs are driven and causes bending. The total deformation and equivalent stress values are obtained from the simulation, and the deformation values are used for calculating stiffness for in-plane bending and out-of-plane twisting conditions.

The torsional stiffness values start to rise from two triangles, and then reaches a maximum at five triangles before dropping as the triangle count increases. The eighty-triangle design configuration had the least amount of torsional stiffness, meaning that it has the highest angular deformation of all TR-SLL designs. Beyond 30 triangles, the slope of the curve flattens considerably. A similar trend holds true for the bending stiffness plot. The two triangle design results in a local minima that rises to a maximum with the eight-triangle design before continuing to fall as triangle count increases. The curve flattens, and then starts to rise beyond the 33-triangle design. As predicted by statics, designs around the equilateral triangle best resist deformations.

Using linear elastic strain energy theory, we can compare the rotational stiffness of each of the beams following:

$$\kappa = \frac{M}{\theta} \tag{5.9}$$

where κ is the torsional stiffness, M is the applied moment, and θ is the angular displacement. The value for the 0.4 mm SLL in Table 5.1 result in a torsional stiffness of 2.3 Nmm/rad while the values from Fig. 5.4(a) result in 518.7 Nmm/rad for the two-triangle TR-SLL, and 964.76 Nmm/rad for the five triangle TR-SLL. The inclusion of triangles to the SLL has a dramatic impact on torsional resistance. Since torsional stiffness directly contributes to the twisting failure mode, we choose the TR-SLL with the highest resistance to torsion to design a gripper, as this minimizes the twisting failure. This TR-SLL design also had lower average stress while twisting, as it can been in Fig. 5.4(c). Since the applied loads are relatively small, the stress values are correspondingly small. These values are well below the failure criteria for the materials (PA-6 or PLA), but they serve as helpful guides to trends in stress values as the number of triangles is changed and as applied loads are increased.

Torsional stiffness was calculated for each TR-SLL configuration for an applied moment of 5 Nmm using the angle of rotation and Eq. 5.9. For calculating the angle of rotation, we

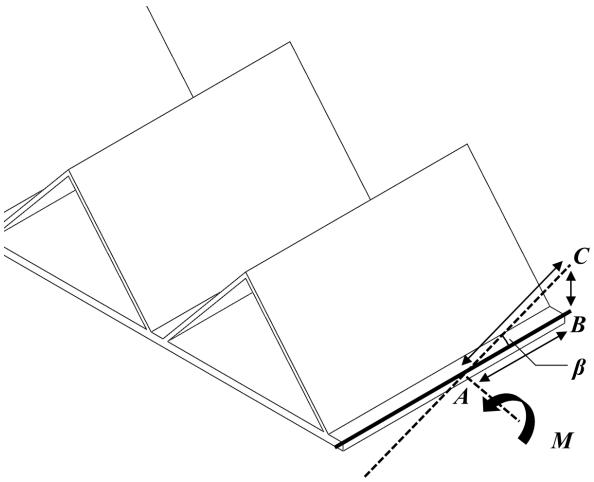

Figure 5.3: Torsional bending setup for simulated angle measurement. The example shown here is a five-triangle TR-SLL. A moment M is applied about the longitudinal axis of the TR-SLL. Line AB is deformed to line AC forming the angle β, which is calculated using Eq. 5.10. The number of triangles was varied across a span of 100 mm resulting in different triangle widths.

employed Eq. 5.10 to find the angle β using the deformation values from the simulation.

$$\beta = \sin^{-1}\left(\frac{BC}{\sqrt{(AB)^2 + (BC)^2}}\right) \tag{5.10}$$

where, AB is the distance from the center to the edge, BC is the linear displacement in vertical direction, β is the angle between line AB and AC, as represented in Fig. 5.3.

Similarly, the in-plane deformation value was used to calculate the bending stiffness for an applied force of 0.01 N for each configuration. The stiffness values were plotted against the corresponding number of triangles that were present in the TR-SLL, and the results are shown in Fig. 5.4.

5.7 Fabrication of Handed Shearing Auxetic Gripper

In this section, we describe the manufacturing and characterization of the Handed Shearing Auextic (HSA) actuators, and the fabrication and assembly steps for the gripper. We present the fabrication process for the TR-SLL, and describe the test methods to evaluate the performance of our gripper.

5.7.1 Characterization of Handed Shearing Auxetics (HSA)

In order to establish a design for our gripper, we characterized HSAs using two main properties, force (F) and torque (τ) as a function of both displacement and rotation. We characterized two different configurations of the HSA, long and short. The long HSA is described as the configuration with eight rows and five columns of unit cells. This configuration provides an extension that allows the gripper to fully close. The short HSA has four rows and five columns of unit cells. The short HSA is included in this work as the long HSA would be poorly constrained with just a connection at the proximal and distal ends. All the HSAs we tested had an outer diameter of 31.75 mm and a wall thickness of 1.8 mm. Rendered images of the two configurations of the HSAs can be seen in Fig. 5.5.

When selecting HSAs for the gripper, a connection at the midpoint of the TR-SLL is required. This ensures that the HSA extension couples directly with TR-SLL bending. For

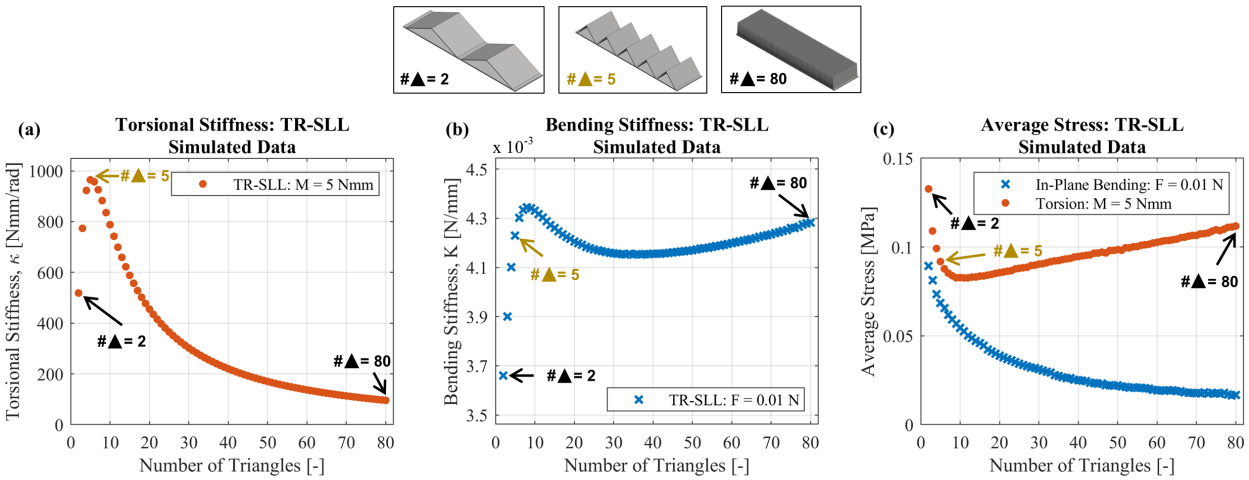

Figure 5.4: Plot of (a) torsional stiffness, (b) bending stiffness, and (c) average stress during bending and torsion as a function of number of triangles in the TR-SLL. In (a), we see torsional stiffness of the TR-SLL calculated from out-of-plane deformation due to an applied moment of 5 Nmm. The most torsionally resistant design is the one with five triangles. In (b), we see the bending stiffness calculated from in-plane deformation due to an applied force of 0.01 N. The design that uses the least amount of input force to achieve the same displacement is the two triangle design. The average stress data in (c) provides insights on stress concentrations in the TR-SLL. All stress values are well below the yield of the material tested.

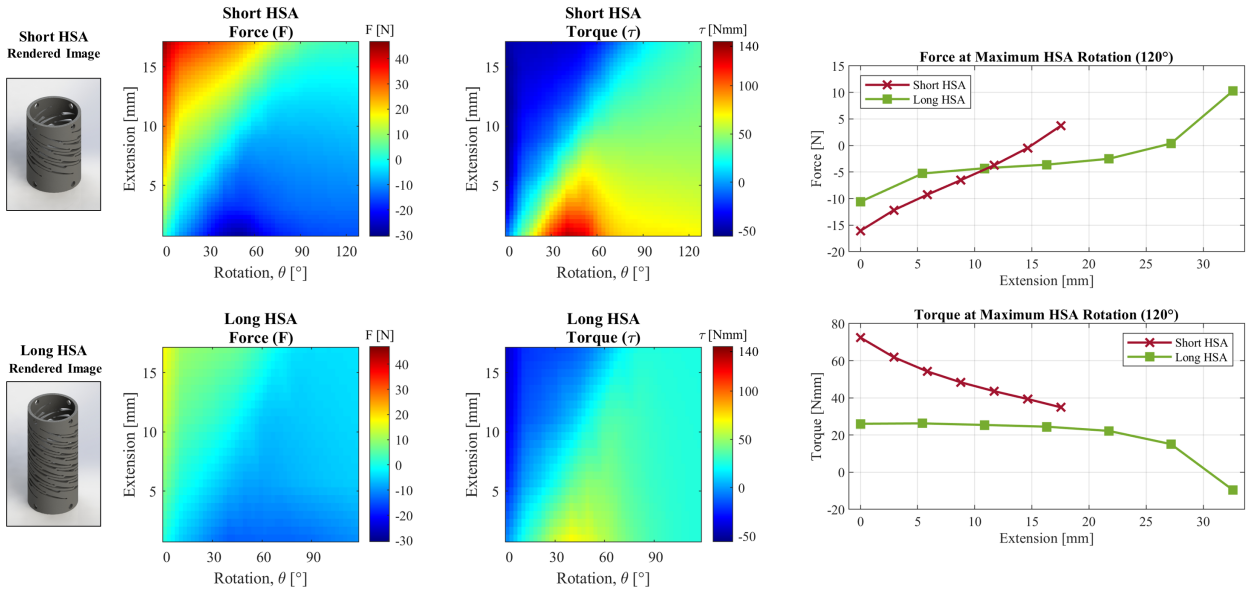

Figure 5.5: This presents the linear interpolated performance heat maps of the short and long HSAs. We measure the mean force and torque as a function of extension and rotation. Negative values represent the HSA pushing on the environment, and positive values represent it pulling on the environment. In the heatmap we see non-linear behavior with a maximum negative force occurring around 0 mm extension and 45° for both HSAs. Values start to shrink beyond this as the HSA experiences larger deformations. Torque values follow a similar trend. Slices of the heatmaps are plotted for the maximum HSA rotation. This corresponds to the angle used when lifting objects. In the sliced 2D plots, we see the force (vs) extension, and the torque (vs) extension data for the long and short HSAs at 120° rotation.

the gripper, two short HSAs are used.

All HSAs we tested were fabricated using the Carbon M1 3D printer with FPU 50. All HSAs were printed horizontally on the build platform, and were post processed following the manufacturer's guidelines and specifications.

The test procedure consisted of a series of extensions and rotations that were programmed using a custom test method on an Instron 68SC-2 at 200 Hz. We varied the extension from 0 to 30 mm, and the rotation from 0 to 120°. The ranges of extension and rotation were determined by manually observing them for the two configurations. The data was collected over seven and fourteen equidistantly spaced points in displacement and rotation respectively. This results in 98 datapoint groups per HSA. Each datapoint group was collected during a 1 mm vertical displacement at 10 mm/s. The raw data collected from the test apparatus was approximated using cubic fits for displacement and rotation to visualize the force (F) and torque (τ) responses of the HSA as shown in Fig. 5.5.

As the HSAs tend towards large compression or extension values, their properties approach that of the bulk material. HSAs are also non-linear. Thus, the smallest order surface fit was chosen that is both non-linear and allows the extrema to tend towards the first and third quadrants. This results in a cubic fit for the data for displacement and rotation. For force, this resulted in an R^2 of 0.974 and an RMSE of 2.82 N for the short HSA, and an R^2 of 0.978 and an RMSE of 1.7 N for the long HSA. For Torque, this resulted in an R^2 of 0.945 and an RMSE of 6.83 Nmm.

A linear interpolation surface fit was chosen to visualize the data. For the force plot, positive values represent the HSA pulling on the environment while negative values represent pushing on the environment. For torque, positive values represent the HSA trying to twist less in the direction it is twisting and negative values represent the HSA trying to twist more than the direction it is twisting in. When added to the gripper, positive torque values positively contribute to payload capacity from the perspective of Eq. 5.6.

For the short HSA, force values reach a maximum of 45.9 N at 17.1 mm extension and 0.0° rotation and a minimum of -29.6 N at 0.0 mm extension and 47° rotation. For torque

values, the short HSA reaches a maximum of 139.2 Nmm at 0.0 mm extension and 39.2° rotation and a minimum of -56.02 Nmm at 8.95 mm extension and 0.0° rotation.

For the long HSA, force values reach a maximum of 23.56 N at 31.9 mm extension and 0.0° rotation and a minimum of -13.55 N at 0.0 mm extension and 48.4° rotation. For torque values, the long HSA reaches a maximum of 68.6 Nmm at 0.0 mm extension and 38.7° rotation and a minimum of -41.2 Nmm at 15.9 mm extension and 0.0° rotation. This work uses a bang-bang position command for opening and closing the gripper. So we compared the performance of the two HSA designs by looking at force and torque at 120° HSA rotation as a function of displacement. This makes it easier to visually understand what is happening during grasp.

5.7.2 Fabrication Process

The fabrication process for the HSA gripper can be seen in Fig. 5.6. First, the HSAs and the TR-SLL were fabricated using SLA and FDM printing processes respectively. Here, we use two left-handed short HSAs for one finger, and two right-handed short HSAs for the other finger. The HSAs were 3D-printed out of FPU 50, while the TR-SLL was printed out of PLA. Additionally, all of the required components, adaptors, and mounts of the HSA gripper were 3D-printed using the FDM process with PLA. The middle section of our gripper contains a bearing that allows rotation of the HSAs, while acting as a constraint for the TR-SLL. At the proximal end of the gripper, a bearing allows the HSAs to be rotated by the motor. We add a layer of Ecoflex 00-30 to the TR-SLL's base and to the gripper's palm to increase the coefficient of static friction. The final assembly of the HSA gripper can be seen in Fig. 5.6. Once assembled, the gripper is mounted on the UR5 arm using four bolts. The gripper weighs 1521 g with the motors and 386 g without the motors and their mounts. If a low inertia end-effector is desired, a flex shaft can be used to transmit motor torque to the gripper.

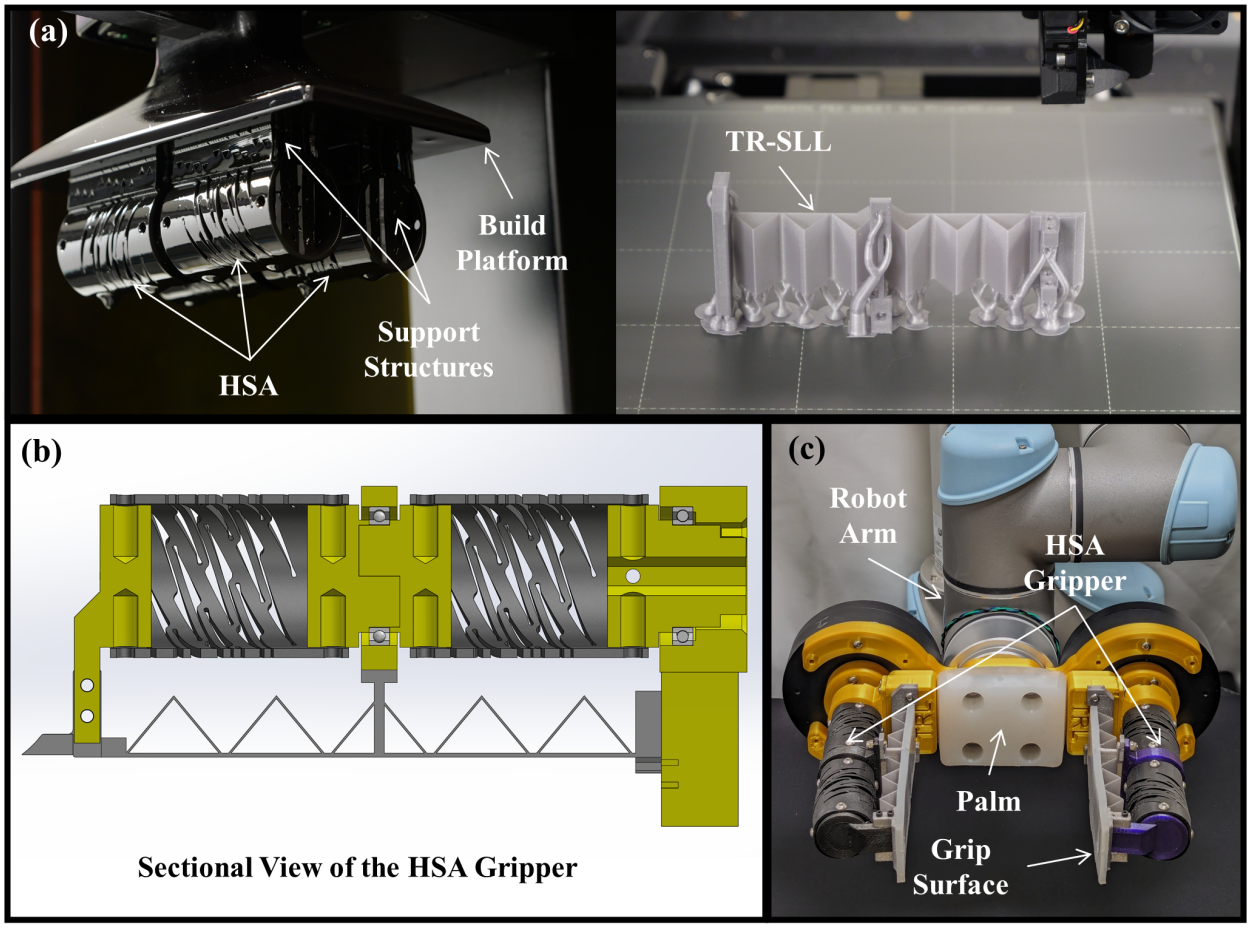

Figure 5.6: This figure shows the fabrication processes of the HSA gripper. First, (a) we print the HSAs using the stereolithography 3D printing process with FPU 50. We also print the TR-SLL with PLA using a standard FDM printer. For the TR-SLL, we cast a layer of Ecoflex 00-30 to achieve a high coefficient of friction. Then in (b), we assemble the components with adaptors and bearings as shown. Finally, we mount the gripper to a UR5 robot arm with two quasi direct drive motors using a shaft as shown in (c). We also mount a cast Ecoflex 00-30 palm to perform caging grasps.The total gripper weight is 1521 g with motors and 386 g without motors.

5.8 Results - Performance Evaluation of HSA Gripper

In this section, we evaluate the performance of our HSA gripper. We test the HSA gripper using the grip force characterization, where the gripper grabs a 90 mm diameter cylinder that is pulled out of its grasp. This demonstrates the maximum payload capacity for the grippers. Finally, the HSA gripper is tested on a subset of the YCB dataset. The subset features objects that fit within the HSA gripper with pinch and planar caging grasps. We show an overall success rate of 86.% out of the 43 objects we tested.

5.8.1 Grip Slip Force Characterization

We characterized the grip strength of our TR-SLL gripper using the grip force test. This test demonstrates the minimum of the three common antipodal failure modes for soft grippers; slipping, twisting, and shearing. Data was gathered using an Instron 68SC-2 at 200 Hz, and the test setup can be seen in Fig. 5.8. Pinch and caging grasps were performed around a painted, 3D-printed 90 mm diameter test cylinder made from VeroWhite on a Stratasys J750 Digital Anatomy printer. The grippers were mounted to a Universal Robotics UR5 arm. The HSAs were rotated 120° to grasp the cylinder. The cylinder was then moved downwards at a rate of 1 mm/s for 10 mm. The force contributions of the HSAs and the TR-SLL were recorded, and the data from the experiment can be seen in Fig. 5.7(c).

The prediction from Eq. 5.6 is also shown in Fig. 5.7(c). To fully analyze this equation, we need use the data for κ for the five triangle TR-SLL as shown in Fig. 5.4. We measure r_t and r_{hsa} using both SolidWorks and micrometers to record the exact thickness of the Ecoflex grip surface using a median measurement. x is recorded during the Instron tests which leaves c_τ to be calculated.

There are two values of c_τ that can be modeled. We can consider two short HSAs in series, or use the data from the long HSA. Additionally, the path must be considered. For this work, we compute c_τ for both the blocked force path (i.e. the path that allows zero extension and only rotation) as well as the path that accounts for the gap between the

gripper and the object as it pinches the cylinder. We call the former the blocked force path and the latter the cylinder prediction path. All four cases are modeled and presented in Fig. 5.7(a) and 5.7(b). Raw data from the Instron tests were used to compute the values of c_τ for all cases. The blocked force path should be an upper absolute bound on values for c_τ for the HSAs presented here as the maximum positive torque value occurred with no displacement.

The long HSA is selected for analysis in Fig. 5.7(c) since it does not require the assumption of two identical series springs. Since the grip force characterization uses the cylinder, the cylinder prediction path is used. Since c_τ is calculated by dividing the torque by the rotation, values around 0° tend towards infinity. For this work, we choose to ignore the infinite values as they do not match real world performance.

In Fig. 5.7(a), we see a max c_τ of 2.53 Nmm/° when rotation is 9.7° for the blocked force path. This tends towards a value of 0.31 Nmm/° when the HSA rotation is 117.5°. The cylinder prediction path starts at -0.58 Nmm/° at 9.7°, reaches a maximum of 0.72 Nmm/° at 48.6° and reaches 0.31 Nmm/° at 117.5°. The values for blocked force are always positive as the torque values start at zero and then steadily climb. For the cylinder prediction path, there is a non-zreo starting displacement. This causes the values to start negative as the HSA applies a negative torque, before transitioning to a positive value.

In Fig. 5.7(b), we see a larger maximum c_τ of 2.77 Nmm/° when rotation is 9.8° for the blocked force path of the long HSA. This tends towards a value of 0.21 Nmm/° when the HSA rotation is 118.6°. This is considerably smaller than the value computed for the short HSA. The cylinder prediction path starts at a larger value of -1.58 Nmm/° at 9.8°, reaches a maximum of 0.58 Nmm/° at a later 57.6° and reaches 0.21 Nmm/° at 118.6°. Since the Cylinder force characterization test uses a motor input of 120°, a c_τ value of 0.21 is selected. Thus a full value for the prediction can be computed. This is shown in Fig. 5.7(c) as a black dashed line.

We can the see that the HSA gripper is capable of achieving a peak holding force of 5.8 N using pinch grasp, and 14.6 N with planar caging grasp. Over the first 3 mm, we observe a grasp stiffness of 1.64 N/mm with pinch grasp, and a grasp stiffness of 3.06 N/mm with the

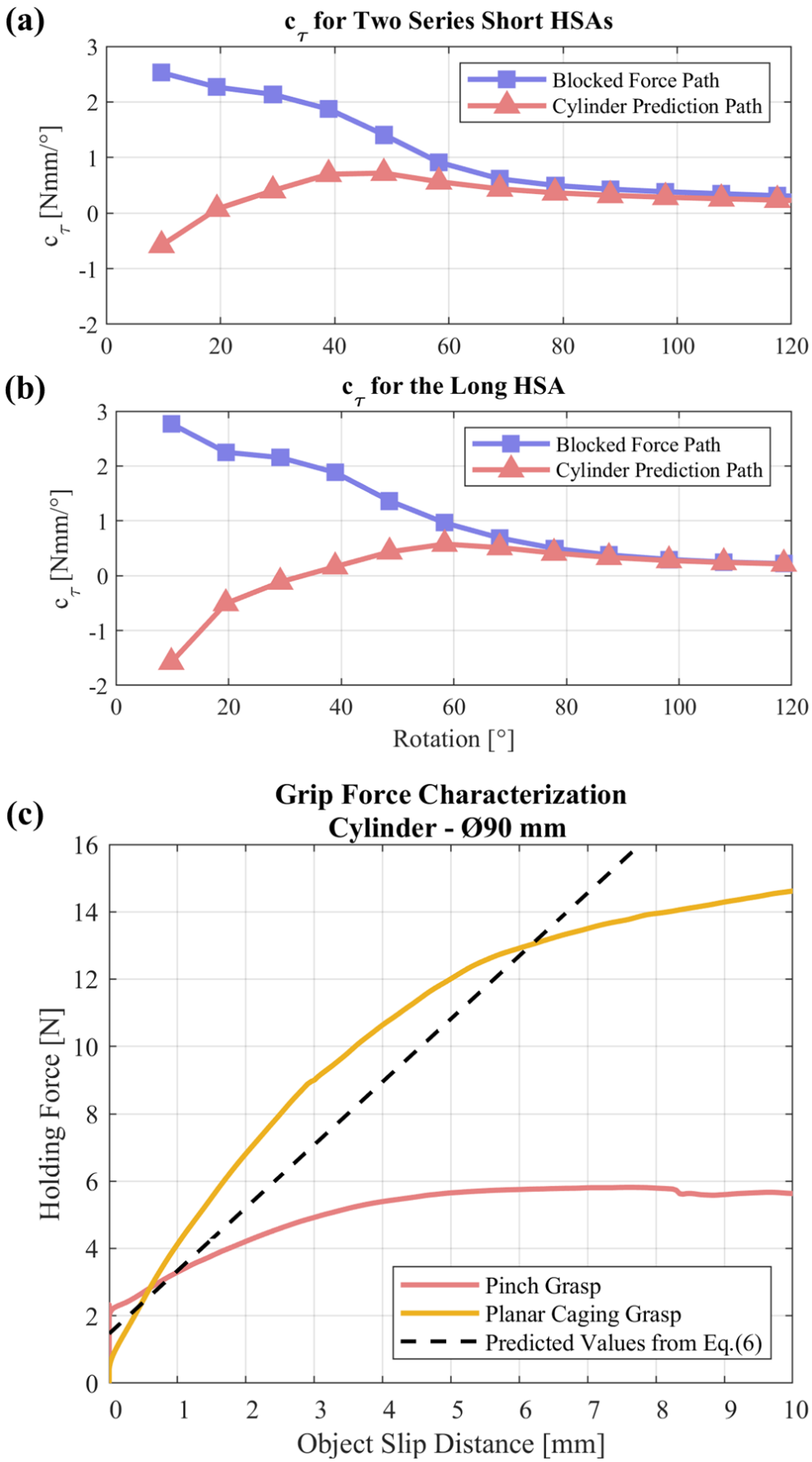
(a)
c_τ for Two Series Short HSAs
Blocked Force Path
Cylinder Prediction Path
c_τ [Nmm/°]
(b)
c_τ for the Long HSA
Blocked Force Path
Cylinder Prediction Path
c_τ [Nmm/°]
Rotation [°]
(c)
Grip Force Characterization
Cylinder - Ø90 mm
Holding Force [N]
Pinch Grasp
Planar Caging Grasp
Predicted Values from Eq.(6)
Object Slip Distance [mm]

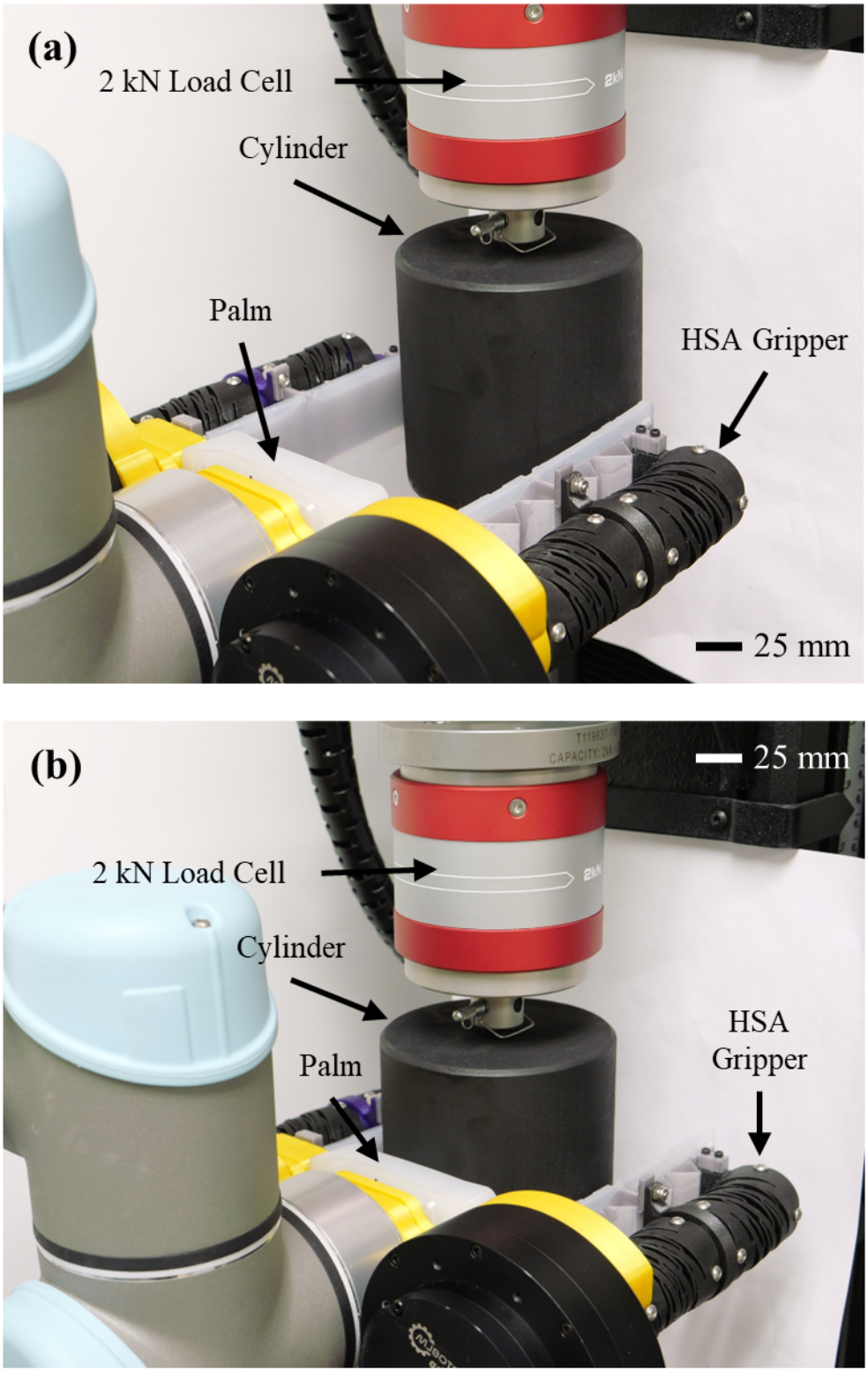

Figure 5.8: Here the Instron testing setup for HSA TR-SLL gripper characterization is presented. The HSA grippers and the motors are fixed to a UR5 robot arm. They are positioned to perform antipodal (a) and planar caging (b) grasps using a painted-, 3D-

planar caging grasp. The prediction model under represents the contribution from the HSA, predicting a value of 1.47 N when the realized performance is 1.98 N. This could be described by the differences in testing environment and by the stacked HSA configuration instead of a single monolithic HSA as used in the prediction. The slope of the dashed line represents the contribution from the TR-SLL element. Based on Fig. 5.2, the minimum set of slipping, twisting, and shearing will govern the maximum holding force the gripper can sustain. Since the slope of the pinch grasp is shallower than the predicted value, this demonstrates that the gripper is not limited by the twisting failure condition. By visual inspection from the supplementary video, the slip condition is insufficient normal force.

5.8.2 YCB Object Grasping

We demonstrate the TR-SLL gripper's ability to pickup objects from the YCB object dataset [28]. We chose to select objects that fit within the gripper (0 to 105 mm). Due to the torque from the HSA, the grippers curve in a smile shape. This causes a minimum height of object below which the object cannot be grasped perpendicular to the gravity field. This height was measured at 14.5 mm. Thus, the set was limited to objects that were at least 14.5 mm tall when standing in their default orientation and able to fit between the opened jaws of the gripper. This left us with 43 objects to test our HSA gripper with. All objects were filled to match their weight and approximate mass distribution according to the data from [28].

Within the object dataset, we chose three possible pick states: Success, Partial Success, and Failure. A successful lift is fully lifting the object off the ground and maintaining it in the grasp for at least 30 seconds. A partial success is lifting the object but not maintaining contact for the full time duration. A failure is not successfully maintaining contact on the object. Of the objects that were not successful in the pinch grasp, a caging grasp was attempted. The maximum of these two grasp attempts is reported as the number of successes, partial successes, and failures. All tests were done using a bang-bang controller switching between two states: open (0°) and closed (120°). The motors used were QDD100 Beta 3 servos from MJbots. The default gains were used on the motors. Across both pinch and

caging grasps, the success rate of the gripper was 86% (37/43), the partial success rate was 9.3%(4/43), and 4.7%(2/43) were unsuccessful.

Object from the YCB data set were first tested using a pinch grasp. The HSA gripper was able to successfully lift 32 objects, with a success rate of 74.41%. The 32 successful objects were the chips can, the cracker box, the mustard bottle, the gelatin box, pudding box, potted meat can, banana, strawberry, apple, lemon, peach, pear, orange, plum, the wine glass, the mug, spatula, padlock, flat and Phillips screwdrivers, the soft ball, baseball, tennis ball, racquetball, golf ball, the smallest and the largest cup, foam brick, colored wood block, the nine-hold peg test, the timer, and the Rubik's Cube. Out of the ten cups, we tested the extreme sizes (smallest and largest) to ensure objects had similar importance within the dataset.

There were five partial successes: the sugar box, tomato soup can, master chef can, the wood block, and the large marker. In this case, while the gripper did not experience any twisting load during object pickup, the first 4 objects listed were partially successful due to insufficient normal force. This corresponds to the slip failure mode in soft grippers. The large marker was a partial success as contact on the object was on the top half of the cylinder, leading to an eventual drop. Hence, 11.6% of the total objects were partially successful with the pinch grasp.

Six objects from the set were failures: the hammer, the windex bottle, bleach cleanser, the nine-hold peg test, the die, and the power drill. The mode of failure was either insufficient normal force or shearing of the Ecoflex layer.

A planar caging grasp was used on the objects that were not in the previous success category. Objects were caged using the palm. Out of eleven objects that were tested with the planar caging grasp, five were successful (nine-hole peg test, master chef can, wood block, sugar box, power drill), two were partially successful (windex bottle, bleach cleanser), and four were failures (hammer, die, large marker, tomato soup can). Two of the objects (windex bottle, bleach cleanser) were partially successful due insufficient normal force. Two of the four objects (hammer, large marker) failed due to insufficient normal force while two (soup

can, die) automatically failed due to the objects being unable to reach both the gripper and the palm.

The overall unsuccessful objects for both the pinch and planar caging grasps accounted to only 13.9% of the entire tested objects. The primary failure modes were determined to be slipping and material shearing. This shows that the TR-SLL increased the gripper's resistance to torsion.

5.9 Conclusion and Future Work

In this paper, we developed a torsion resistant strain limiting layer (TR-SLL) to increase payload capacity by increasing torsional resistance. A comprehensive design study was conducted using FEA simulations to understand the design landscape of triangulated beams. The number of triangles on a 102-mm long strain limiting layer was varied to characterize the performance of the TR-SLL in plane and out of plane. It was found that designs near equilateral triangles best resist torsional loads. We also characterize the 3D force and torque landscape for HSAs in terms of displacement and rotation. This data was then used to predict the payload capacity due to twisting of the gripper and found that twist was not the dominant failure mode for the gripper.

This work found that adding a torsion resistant strain limiting layer dramatically increased torsional performance, demonstrating a grasp stiffness value of 3060 N/m. The addition of the TR-SLL allowed a electrically-driven handed shearing auxetic gripper to pick up a 5 kg dumbbell, maxing out the payload capacity of the robot arm it was installed on. The TR-SLL gripper was also tested on a subset of the YCB data set and successfully picked up 86% of the objects. Future work for these TR-SLL grippers include sensorization, additional characterization of the TR-SLL design space to incorporate additional design parameters, and more intelligent controls to further improve grasp performance. This work lays the foundation to easily incorporate TR-SLLs into existing soft robots and demonstrates additional payload capacity that is often lost due to torsional deflection in soft grippers.

Figure 5.9: This figure shows the YCB test objects we evaluated the HSA gripper against. Objects were filtered to have a critical dimension that fit within the jaws of the gripper. First a pinch grasp was performed on the dataset. A success was defined as lifting the object and holding it for 30 seconds. A partial success was fulfilled if the object was able to be picked up but was not stable after 30 seconds. If the object was unable to be lifted off the ground, it was a failure. Of the objects that were not fully stable after the time period, a caging grasp was employed. The same success metrics were employed. The gripper was successfully able to lift all objects across both grasp modes. However, three objects only achieved a peak of partial success.

Chapter 6

TORQUE RESPONSIVE METAMATERIALS ENABLE HIGH PAYLOAD SOFT ROBOT ARMS

6.1 summary

Soft robots have struggled to support large forces and moments while also supporting their own weight against gravity. This limits their ability to reach certain configurations necessary for tasks such as inspection and pushing object up. We have overcome this limitation by creating an electrically driven metamaterial soft arm using handed shearing auxetics (HSA) and bendable extendable torque resistant (BETR) shafts. These use the large force and torque capacity of HSAs and the nestable torque transmission of BETRs to create a strong soft arm. We found that the HSA arm was able to push 2.3kg vertically and lift more than 600g when positioned horizontally, resulting in .33Nm of torque at the base. The arm is able to move between waypoints while carrying the large payload and demonstrates consistent movement with path variance below 5mm. Finally, we test the arm in a pipe inspection task. The arm is able to locate all the defects while sliding against the inner surface of the pipe, demonstrating its compliance.

6.2 Introduction

Soft robot arms have been trapped in hanging form factors and low payloads due to their inability to support larger forces and moments. Hanging form factors restrict a soft robot's ability to interact with their environment to a top-down perspective, rather than the one that most benefits the task at hand. We present an electrically driven metamaterial robot arm that is capable of lifting large payloads while also supporting its full weight under gravity as seen in Fig.6.1 A). This allows the arm to operate in whatever orientation best serves the

current task.

Soft robot arms are a broad area of research [169, 198]. They have been used to explore ruins [42], for sample collection underwater [193], and even mounted on drones for docking [3]. A huge benefit of soft robot arms comes from their distributed compliance which helps provide a physical guarantee of safety and with tasks such as pick and place. However they are broadly held back by two limitations: small supported torque and payload capacities.

Supporting large forces and torques is critical for robot arms. Li et al [108] is able to create tremendous force capacities through fluid driven artifical muscles, capable of lifting car tires. However these are limited to pulling through the body of the soft arm and can not support meaningful torques. The combination of both meaningful force and torque resistance is vital to a useful robot arm. We build a soft robotic arm that is capable of lifting large payloads while supporting its own weight under gravity.

In this paper we:

- Design a soft robot arm using handed shearing auxetics capable of lifting more than 2 kg vertically and 600 g horizontally.

- Analyze the design space of handed shearing auxetics and characterize bendable, extendable flex shafts

- Evaluate the arm through object lifting and pipe inspection tasks

6.3 Background

There is a large body of recent literature in soft robot arms. Guan et al. created an arm capable of lifting strawberries through cable driven helicoid structures [64]. Kang et al. and Zhao et al. used shape memory alloy muscles to lift water cups and ping pong balls [93, 204]. Ahlquist et al., Lui et al., and Bianchi et al. all created pneumatics based arms to dock, pick flowers, and throw ping pong balls [3, 13, 113]. However all of these works have two things in common: Small payloads, and an inability to support themselves outside of a hanging

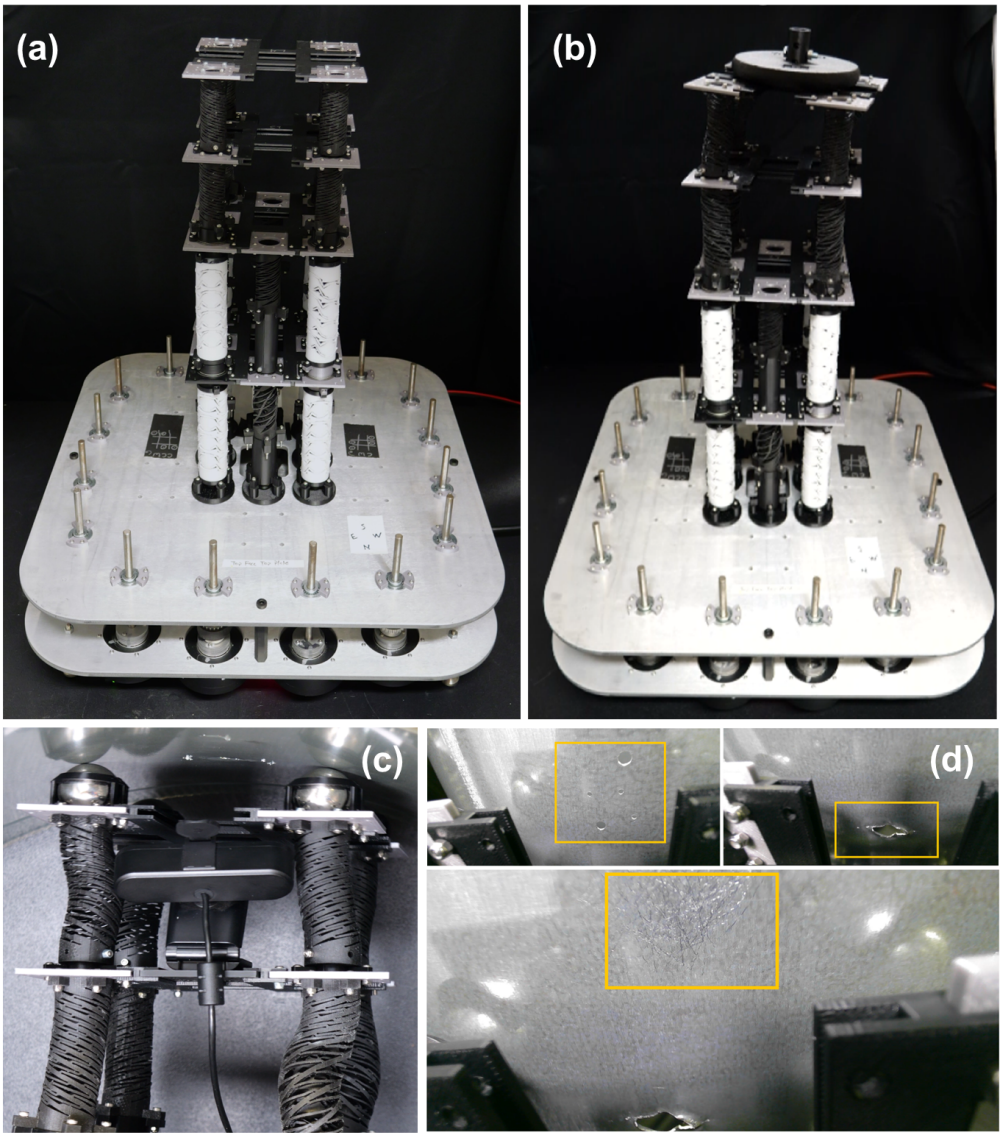

Figure 6.1: We present a soft Handed Shearing Auxetics (HSA) robot arm that is able to support meaningful forces and torques while holding itself up against gravity. Subfigure (a) shows the assembled soft HSA arm, (b) shows the soft HSA arm lifting a 2.3kg payload vertically, (c) shows the inspection task setup with the mounted webcam, and (d) shows the different pipe defects (holes, gash, scratches from top left) captured by the HSA arm during the inspection task.

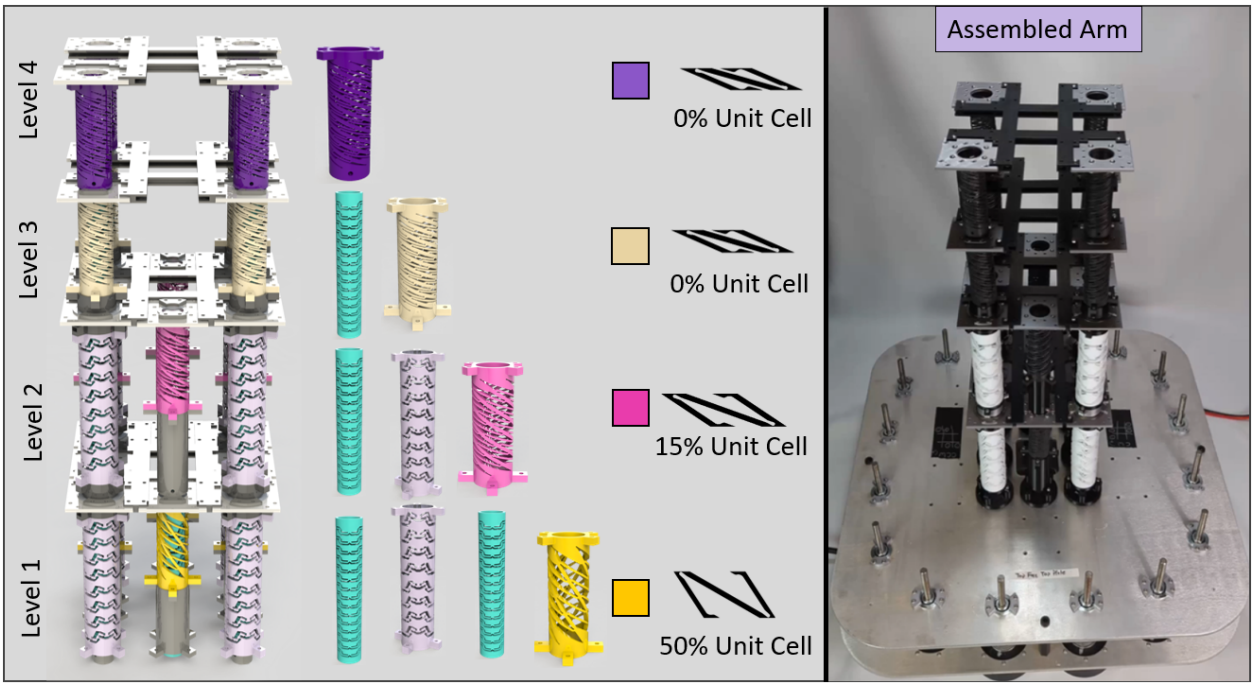

Figure 6.2: A System overview is presented for the HSA Arm. The arm is made from four layers, with each driven by a different HSA. Proximal layers use HSAs printed further along the auxetic trajectory culminating in a thinner distal HSA. HSAs on level two through four are driven by nested Bendable Extendable Torsionally Rigid (BETR) shafts. A rendered version of the arm is shown on the left and the realized construction can be seen on the right.

configuration. These arms cannot be inverted and would buckle while trying to support their own weight, let alone additional weight from a payload. These are major restrictions. The field of robotics has centralized on objects from the YCB dataset [28] which have masses much greater than that of a ping pong ball or strawberry. To demonstrate the great benefit of soft robots, we need to support payloads in the hundreds of grams range.

Some soft robot arms can lift meaningful payloads. Li et al. used pnematic muscles to lift a car tire [108]. While capable of supporting meaningful payloads, this arm cannot support itself outside of the truck configuration and can only support large forces, not moments. Childs et al.,Yang et al., and Bruder et al. have created soft robotic arms capable of meaningful payloads while supporting moments, however, they support smaller forces and torques that the work presented here [23, 35, 197].

Handed Shearing Auxetic (HSA) soft robots have emerged as a promising field for their ability to generate large forces and for their ability to hold themselves up against gravity [63, 111]. Work has been done to generate controls and models for 4-DoF platforms resisting gravity [62, 172]. They have also been used in mobile robots [97, 100] to carry electronics payloads, and in packing groceries [34]. For mobile platforms, payloads are still relatively small compared to the largest objects in the YCB set and for the grocery packing robot, only the gripper was soft. The largest limitation however is that handed shearing auxetic robots are limited to a single layer of HSA, preventing their use as a robot arm. Recent works [100,180] have enabled torque transmission to HSAs not directly connected to a motor.

This points towards electrically driven soft robots as a capable solution for soft robot arms. HSAs can support large forces and torques while supporting themselves under gravity and now no longer require a direct connection to a motor to actuate.

6.4 Design of Metamaterial Soft Robot Arm

This section describes the design of our four layer soft metamaterial robot arm. First, we use a lumped element model to determine component performance targets for horizontal payloads of 500 g and 2 kg vertically. Then, we manufacture and test components for both

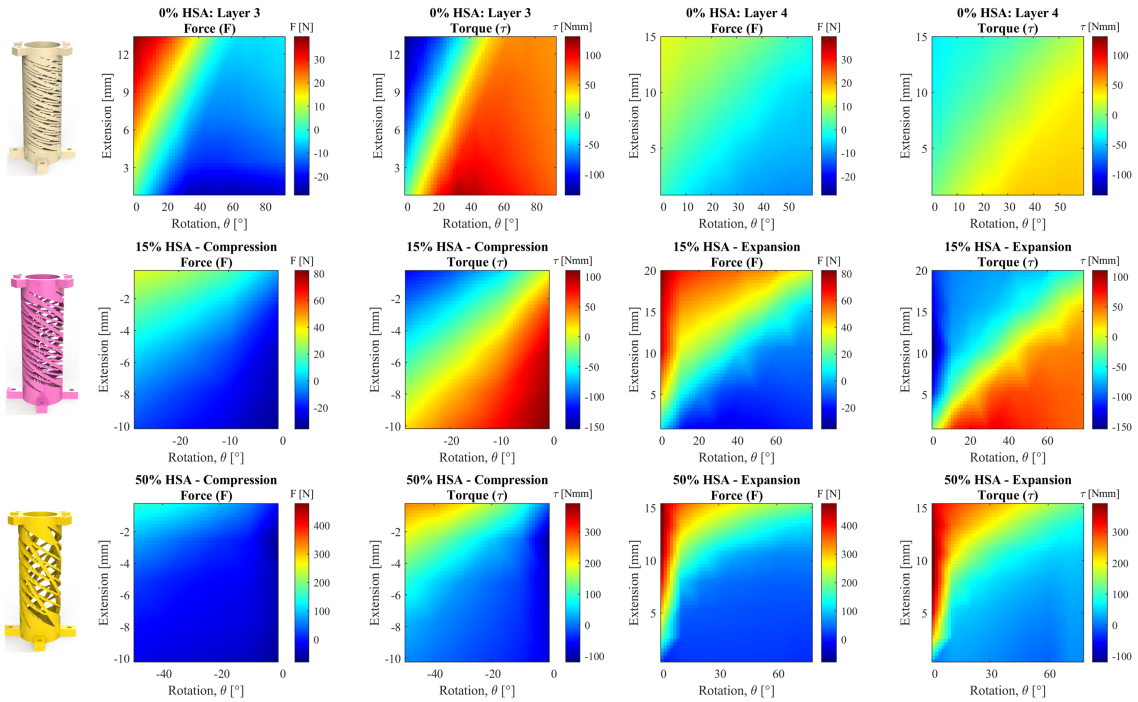

Figure 6.3: Interpolated HSA force and torque characterization is presented here for each of the four layers of HSA in the soft arm. Thick- and thin-walled HSAs printed at 0% of way along the auxetic trajectory are presented with just expansion data (layer 3, 4 respectively) and HSAs printed beyond that (layer 1, 2) are shown with both expansion and compression regions.

Table 6.1: Table showing the minimum and maximum force (F) and torque (τ) values for all the HSA configurations from the mechanical characterization data. Here, θ represents the corresponding value of rotation and **e** represents the corresponding value of extension. The table is divided into two categories to represent the values in the compression and expansion regimes.

COMPRESSION

HSA Type	**Min. Force (θ, e) [N]**	**Max. Force (θ, e) [N]**	**Min. Torque (θ, e) [Nmm]**	**Max. Torque (θ, e) [Nmm]**
50%	-79.5 (0, -2.6)	167.3 (-49.9, 0)	-120.3 (0, -2.6)	275.8 (-49.9, 0)
15%	-34.5 (0, -10.4)	38.3 (-29.9, 0)	-130.2 (-29.9, 0)	110.89 (0, -10.4)
0% (Thick)	-	-	-	-
0% (Thin)	-	-	-	-

EXPANSION

HSA Type	**Min. Force (θ, e) [N]**	**Max. Force (θ, e) [N]**	**Min. Torque (θ, e) [Nmm]**	**Max. Torque (θ, e) [Nmm]**
50%	0 (0, 0)	478.1 (0, 15.7)	-8.8 (59.9, 0)	392.2 (0, 10.4)
15%	-26.3 (29.9, 0)	82.5 (0, 20.4)	-153.29 (0, 10.2)	87.9 (9.9, 20.4)
0% (Thick)	-27.9 (42, 0)	39.7 (0, 13.6)	-134.8 (0, 13.6)	131 (31.3, 0)
0% (Thin)	-11.21 (59.9, 0)	13.1 (0, 15.3)	-40.2 (0, 15.3)	47 (19.9, 0)

extension performance and torque transmission. We finally evaluate the assembled system to see how well it meats the initial design requirements.

6.4.1 HSA Characterization

To establish a design space for the HSAs in the arm, we selected a 2 kg vertical lift target and a 500 g horizontal lift target. We then used kinematics to determine the forces and torques required to support those loads and used that as targets for the HSA property space. Based on work from [63,183], we designed HSAs to achieve the target properties, then printed them.

We characterized the HSAs using two main properties, force (F) and torque (τ) as a function of both displacement and rotation. We characterized four different configurations of the HSA, 50% open, 15% open, 0% open, and 0% open with thinner walls. The 50% open HSAs occupied the first layer of the arm, 15% open HSAs occupied the second layer, and the 0% HSAs occupied layers three and four as shown in Fig. 6.2. For layer 4, we reduced the wall thickness of the HSA to reduce the torque requirement for actuation. All of the HSAs on layers 1, 2 and 3 (50%, 15%, 0%) had a length of 90.5 mm, an outer diameter of 30.7 mm, and a wall thickness of 3.5 mm. Layer 4 HSAs (0%) had the same length and outer diameter with a wall thickness of 1.7 mm.

6.4.2 Torque Transmission Characterization

All HSAs we characterized were fabricated using the Carbon M1 3D printer with FPU 50. All HSAs were printed horizontally on the build platform, and were post processed following the manufacturer's guidelines and specifications.

The test procedure consisted of a series of extensions and rotations that were programmed using a custom test method on an Instron 68SC-2 at 200 Hz. We individually chose the extension and rotation values based on the maximum safe limits of the tested HSA configurations. The ranges of extension and rotation were determined by manually observing them for all HSA configurations. The data was collected over seven and fourteen equidistantly spaced points in displacement and rotation respectively. This results in 98 datapoint groups per

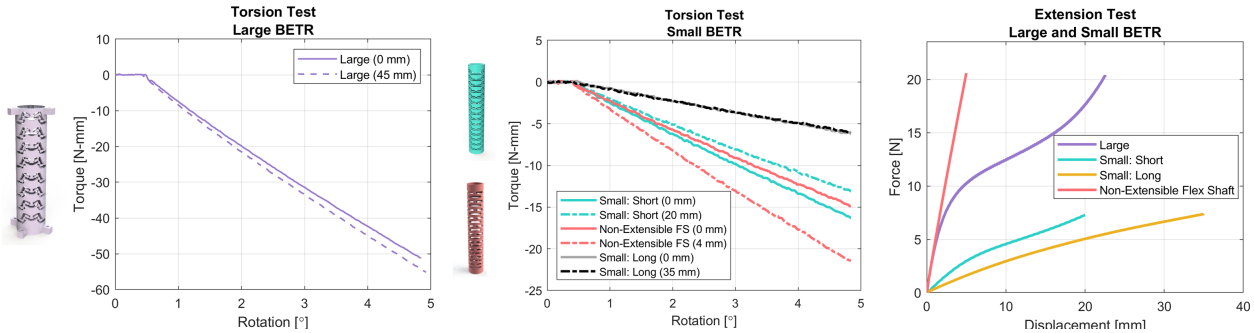

Figure 6.4: Plot of Torsion and extension tests for the soft soft torque transmission elements in the robot arm. We characterize elements for layer 2 (Small: Short), layer 3 (Large BETR), and layer 4 (Small: Long). We also characterize the single non-extendable flex shaft for complete individual component level analysis. Torque characterization was done when in the extended (dashed) and rest states (solid). The X intercept represents the slack/deadband in the material and the slope represents the torsional stiffness. Forces required to extend the elements in the arm are also shown in the extension test plot. These values oppose HSA extension.

HSA. Each datapoint group was collected during a 1 mm vertical displacement at 10 mm/s. The raw data collected from the test apparatus was approximated using cubic fits for displacement and rotation to visualize the force (F) and torque (τ) responses of the HSA as shown in Fig. 6.3.

A linear interpolation surface fit was chosen to visualize the data. For the force plot, positive values represent the HSA pulling on the environment while negative values represent pushing on the environment. For torque, positive values represent the HSA trying to twist less in the direction it is twisting and negative values represent the HSA trying to twist more than the direction it is twisting in. The maximum and minimum force and torque values observed for each HSA configuration is shown in Table 6.1.

To deliver torque to layers two through four, a bendable, extendable torque transmission system is needed.We looked to the work presented in [180]. We characterized three different configurations of the extendable flex shafts (BETRs), large, long, and short. We characterized their force and torque responses using an Instron 68SC-2 mechanical testing machine. As these BETRs are intended for transmitting torque from the motors to the HSAs, we evaluated the torsional stiffness of these BETRs, while also testing the force required to extend them. Additionally, we incorporated a non-extensible flex shaft at the first layer of the arm to provide enhanced torsional stiffness, while the extendable BETRs were used for the second and third layer. The CAD rendering of the BETR designs can be seen in Fig. 6.2. The large BETR had an outer diameter of 30.7 mm and a wall thickness of 4.5 mm. They were fabricated with PTFE tubes using a Bantam Desktop CNC machine. The large BETRs were utilized to drive the arm's third layer. Additionally, we fabricated two variants of small BETRs, short and long. The small BETRs were made out of FPU 50 using a Carbon M1 3D printer, and can be seen in Fig. 6.4. The long BETR was fabricated by connecting two short BETRs and a single non-extendable flex shaft using 3D-printed adaptors made out of PLA. The short BETRs were used to drive the 15% HSAs on the second layer of the HSA arm, while the long BETRs were used to drive the 0% HSAs on layer 4 as shown in Fig.6.2.

The torque response was recorded for the large, short, and long BETRs and the non-

extendable flex shaft by applying a rotation of 5 degrees at a rate of 1 deg/s. This characterization was done in both non-extended and extended states for each of the components to understand how torsional stiffness changes with extension. Little change was observed for the BETRS. The large, long, and short BETRs were extended to 45 mm, 35 mm, and 20 mm respectively, while the non-extendable flex shaft was extended to 4 mm. Similarly, for force response, an extension of 22 mm, 20 mm, 35 mm and 5 mm was used for the large, short, long, and non-extensible flex shaft respectively at the rate of 1 mm/s. All of the recorded data were visualized as shown in Fig. 6.4.

The torsional stiffness values were then calculated from raw data for each of the BETRs. The large BETR had torsional stiffness values of -11.52 Nmm/deg and -12.03 Nmm/deg at the non-extended and extended states respectively. The long BETR was at -1.39 Nmm/deg and -1.33 Nmm/deg at the non-extended and extended states, showing very little difference in its performance. The short BETR had torsional stiffness values of -3.60 Nmm/deg and -2.90 Nmm/deg at its non-extended and extended states. The non-extendable flex shaft had torsional stiffness values of -3.29 Nmm/deg and -4.78 Nmm/deg at the non-extended and extended states respectively.

6.4.3 Fabrication of the Soft Arm

In this section, we describe the manufacturing and characterization of the Handed Shearing Auxetic (HSA) actuators, and Bendable Extendable Torsionally-Rigid (BETR) flex shafts. We also describe the fabrication and assembly steps for the HSA arm. We then describe the test methods that were used to evaluate the performance of the robot arm.

A parallel plate system was used to connect the sixteen independent Quasi-Direct Drive motors (QDD100 Beta 3) to the HSAs and BETRs through pulleys. Two torques were transmitted along the same shaft using a set of live and dead axle pulleys with the motors preventing unwanted cross-talk. This forms the metal base at the bottom of the robot that the soft arm is built on top of.

The components used for the fabrication of the robot arm can be seen in Fig. 6.2. The

HSA arm is made from four levels or layers, where each level was connected to the other layer using 3D-printed plate sections.

For the first level, we added four large BETRs (lavender) with one in each section that drives another four large BETRs at level 2. The large BETRs drive the 0% HSA (gold) at level 3. Long BETRs (teal) run through the inner sections of the large BETR up to level 4 to drive the thinner HSAs (purple) at the distal end. Levels 1 and 2 are driven using 50% (yellow) and 15% (pink) HSAs at levels 1 and 2 respectively. In order to maximize force output, the HSAs were connected to 3D-printed adaptors at levels 1 and 2 as shown in gray in Fig. 6.2.

6.5 Results - Performance Evaluation of HSA Arm

In this section, we evaluate the performance of our HSA arm. The arm performs lifting tasks to demonstrate payload capabilities in both a horizontal and vertical configuration. The arm's compliance is evaluated by inspecting a pipe ,commonly found in the Oil and Gas industry, for defects. The workspace of the arm is evaluated using an optical motion tracking system. This demonstrates the HSA arm's reachable positions in 3D space. The arm was tested for its repeatability by programming it to follow triangular and square patterns for a fixed period of time.

6.5.1 Payload Evaluation

We demonstrate the payload capacity of the metamaterial soft robot arm in both horizontal (extending out) and vertical (extending up) configurations.

The horizontal test is conducted following the methods established in [197]. The arm is commanded to move up against gravity from the home position and weights are added until it returns home. The home position was recorded as breaking the beam of the laser and the test ended when the beam when the beam was broken again. The arm was able to support 550g in weights without breaking the beam but failed to support 575g. The weights were suspended 60cm out from the base, resulting in a torque to the base of the arm of 0.33Nm.

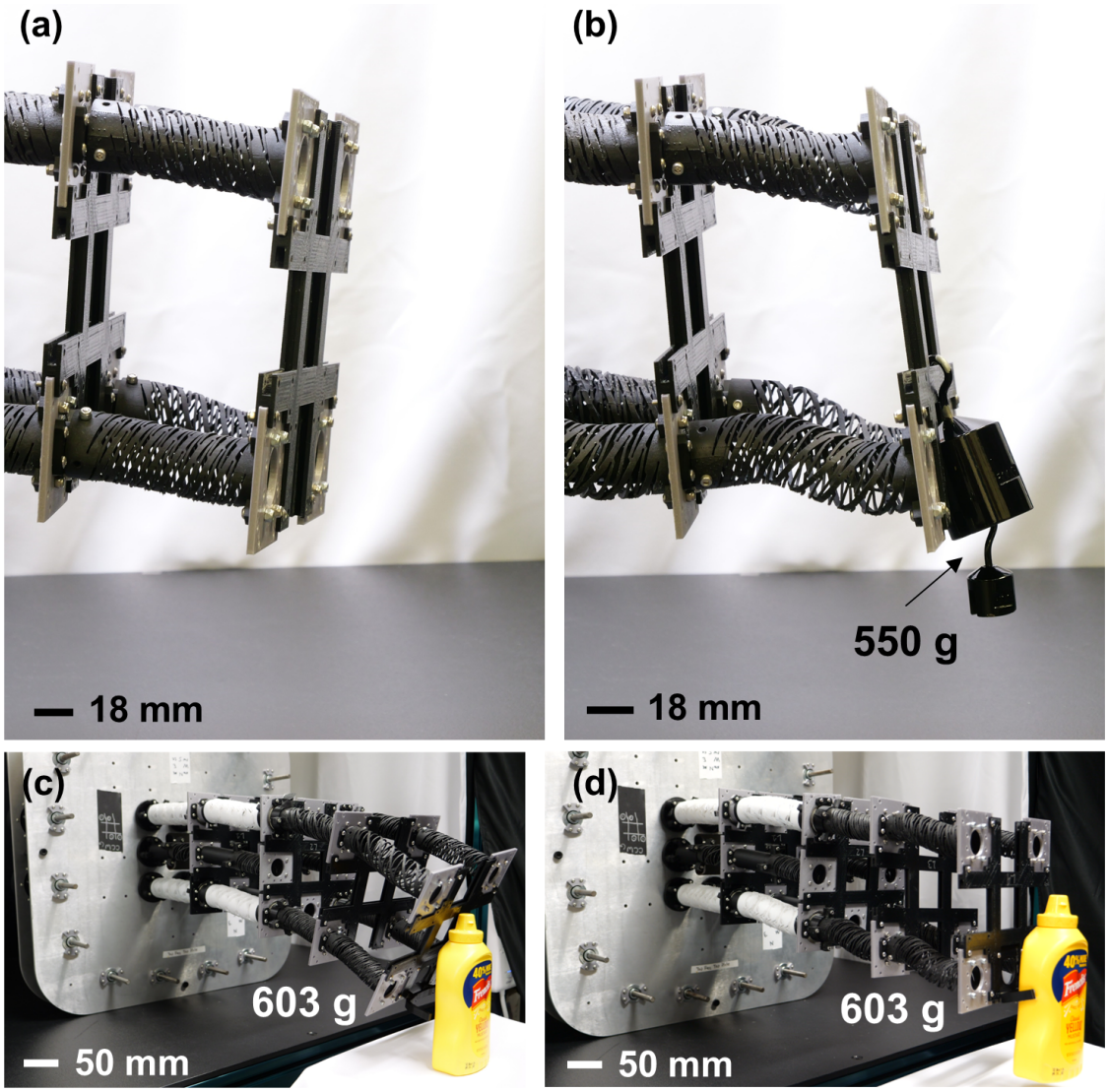

Figure 6.5: Here we present the maximum load supported when the arm is positioned horizontally (b). First the arm's default resting position is recorded with a laser level. Then the arm is moved up to its maximum extension. Weights are added to the distal tip until the arm returns to its starting position. The arm is able to support 600 g when horizontally extended, resulting in 0.33 Nm of resisted torque. Subfigures (c) and (d) show the HSA arm before and after lifting a 603-g mustard bottle from the YCB object dataset

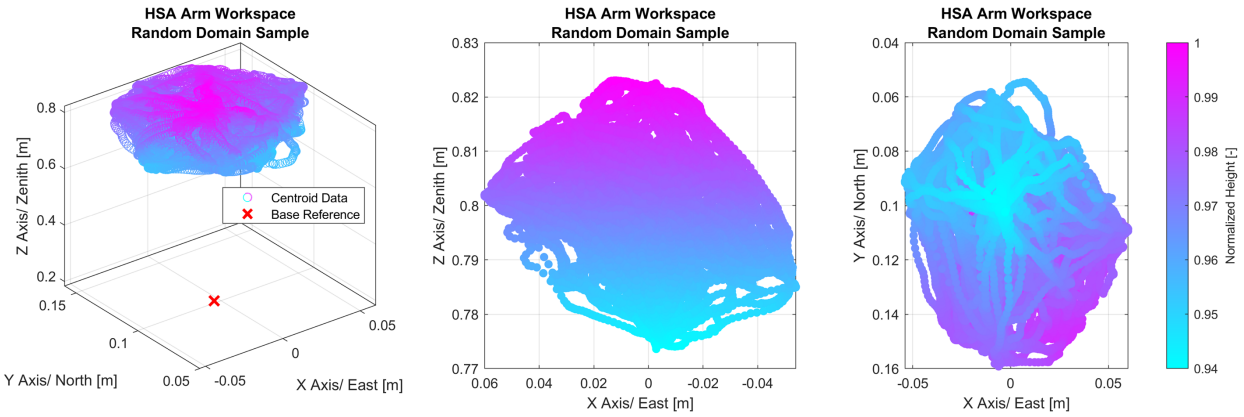

Figure 6.6: Here we present the workspace of the Arm as tracked by a rigid body at the tip of distal tip of the robot arm. The arm is moved to the cardinal, inter-cardinal, extended, and twisted positions in a randomized order. The centroid as tracked from the motion capture system is presented in 3D as well as in two slices from the Y and Z direction respectively. The arm covers a range of 106.5 mm in X, 105 mm in Y and 50 mm of extension in Z.

This demonstrates a huge payload, especially for a soft robot arm that is supporting itself perpendicular to gravity.

A vertical lift test was also conducted as shown in Fig.6.1 B). Here a 2.3kg payload was bolted to the distal tip of the arm, and the arm was commanded to extend upwards. Extension and a twisting motion were observed. The arm successfully lifted the payload and was able to move through both repeatability test motions (triangle and square). The arm was also supporting the entire weight of the soft components up against gravity, demonstrating large payload capacity, even when constrained to support its own body weight.

6.5.2 Inspection Evaluation

We performed a mock inspection of a 2 foot (610mm) diameter pipe, commonly found in the Oil and Gas industry. The goal of the inspection task was to show that the HSA arm can be controlled to move along a curvature, which helps in performing inspection tasks. The

HSA arm was placed horizontally before performing the inspection task. A roller was placed on top of each section using FDM 3D-printed mounts to facilitate smooth drag across the surface of the pipe when the arm is in contact. We inspected three common pipe defects, a gash, holes, and scratches [46, 135]. We fixed a Webcam on layer 3 to view and record the pipe defects and arm movement. Highlights from this can be found in Fig.6.1 D) where the holes, gash, and scratches are highlighted in a gold box. The arm was teleoperated in a search pattern from left to right, and top to bottom over the pipe surface. The arm movement was manually stopped when the defect was found, and the search motion was resumed. The video of the HSA arm's inspection task can be found in the supplementary material.

6.5.3 HSA Arm Workspace Analysis

First, we evaluated the reachable workspace of the HSA arm using random domain sampling among thirteen target positions (rest, two extension, two twist, four cardinals, and four ordinals). The workspace analysis helps in assessing factors such as the arm's ability to reach all the necessary points to perform a specific task. Four tracking markers were attached to 3D-printed mounts, which were fixed to the fourth layer of the HSA arm. A rigid body was then defined using these four markers at the distal tip of the arm and compared to a base reference for tracking. The test was allowed to run continuously for ten minutes to fill in the workspace. The data was recorded using an OptiTrack motion capture system using four Flex 13 cameras. The centroid data of the rigid body at the distal tip was considered to visualize the reachable workspace of the HSA arm, which is shown in Fig. 6.6. Here, the base reference point was determined by subtracting the total height of the arm from the initial position of the tracked centroid. The arm was able to fill in the domain sample quite well with less coverage coming to or from the rest position. The centroid achieved a mobility range of 106.5 mm in X, 105 mm in Y and 50 mm of extension in Z. This provides a reasonable workspace to manipulate heavy objects such as lifting a YCB mustard bottle [28] as shown in Fig.6.5C) and D).

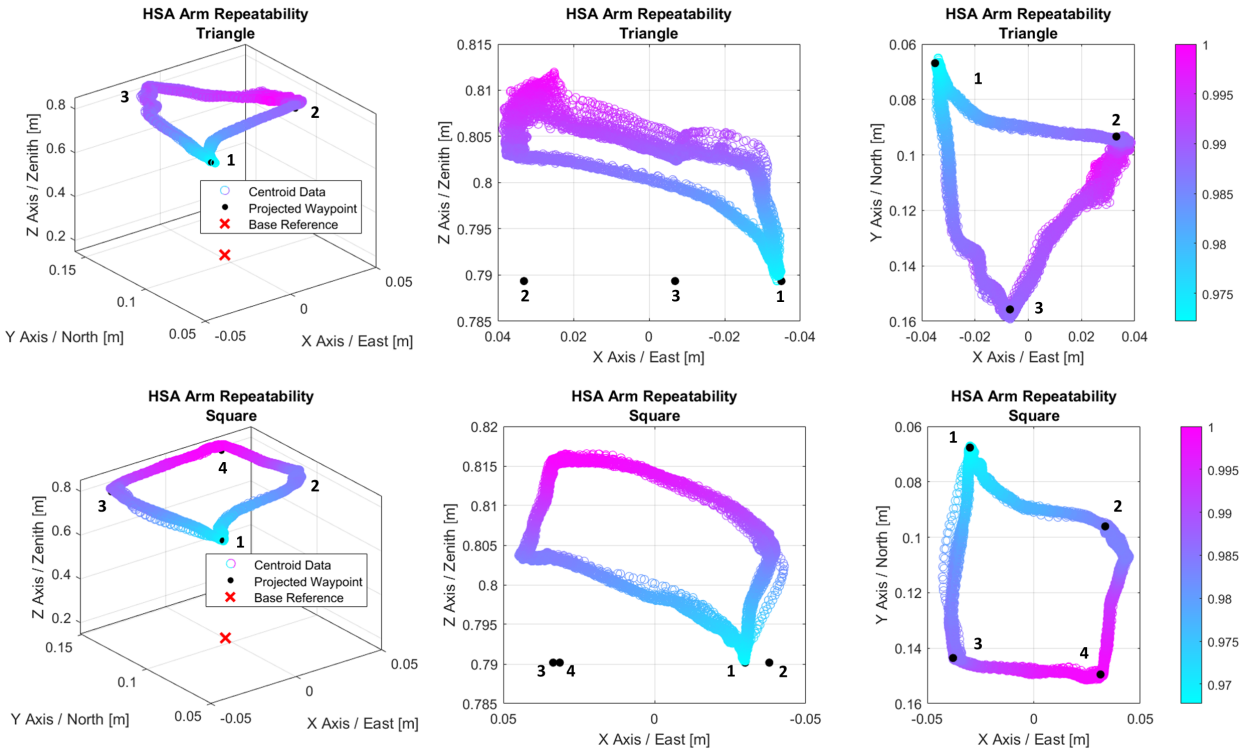

Figure 6.7: In this figure we show motor inputs corresponding to a triangular movement pattern (N, SE, SW) and a square movement pattern (NW, NE, SE, SW) repeated 45 times. Color represents Zenith and black dots represent the most common location the arm moved to projected down to the lowest point in its trajectory. As can be observed, the arm is very repeatable, with most variance in position below 5 mm.

6.5.4 HSA Arm Repeatability

Repeatability tests were performed to show the HSA arm's ability to repeat specific patterns by programming the arm to move to specific cardinal and inter-cardinal directions. We chose triangular and square movement patterns for this evaluation task. The same optical motion tracking setup as described in the previous subsection was used to record the data during the movement of our arm. We moved the arm to the north (N), southeast (SE), and southwest (SW) positions for a triangular pattern, and to the northwest (NW), northeast (NE), southeast (SE), and southwest (SW) positions to follow a square movement pattern. The triangular and the square patterns were repeated for 45 cycles, where each cycle took 11.6 seconds for the square pattern, and 8.6 seconds for the triangular pattern. The transient startup data from the first cycle was removed. The centroid data was recorded and plotted in the three-dimensional space to visualize its path. For the two repeatability test patterns, we have shown the path of the tracked centroid corresponding to a reference point which denotes the base of the arm. The base reference points shown in Fig. 6.7 were calculated by subtracting the total height of the arm (590 mm) from the rest position of the centroid for each pattern. During the repeatability tests, variances can be observed in some regions (for square pattern: paths 1 to 3 & 2 to 1; for triangular pattern: paths 3 to 2 & 2 to 1) which might be caused by the internal PID controllers of the motors. Projected waypoints are shown in black in Fig. 6.7. Waypoints were determined by identifying the points where the centroid moved to frequently, and projecting them onto the plane where the global minimum value lies so they could be visualized. Most X-Y variance between paths falls under 5 mm, demonstrating strong repeatability.

6.6 Conclusion and Future Work

In this paper, we designed and fabricated a soft robot arm using handed shearing auxetics (HSA) and bendable extendable torsionally-rigid flex shafts (BETR). We characterized the 3D force and torque landscape for HSAs in terms of displacement and rotation. We also

analyzed the BETRs using mechanical testing to measure its force and torque responses. Then, we performed the workspace and repeatability analysis of the HSA arm using optical motion tracking system. We tested the arm's maximum load capacity and demonstrated the arm's ability in performing tasks such as lifting and pipe inspection.

The arm was able to lift more than 600 g when horizontal and 2300 g when vertical while also supporting its own weight against gravity. The arm demonstrated a range of motion of 100mm in translation and 50mm in extension. Through repeatability tests, the arm showed strong repeatability with most path variance below 5mm. Future works could consider expanding the available workspace for the arm, and developing more robust controls and controllers.

This work set out to show that soft robot arms can support large payloads and moments, all while supporting their own weight under gravity. This enables more functionality for soft robotic arms by allowing them to be mounted in various configurations. By leveraging the benefits of handed shearing auxetics (HSAs) and bendable, extendable flex shafts (BETR), torque can be transmitted through a multi-stage arm, capable of lifting and moving with more than 2 kg.

BIBLIOGRAPHY

[1] *Overview*, chapter 1, pages 1–50. John Wiley and Sons, Ltd, 2015.

[2] Eric Acome, Shane K Mitchell, TG Morrissey, MB Emmett, Claire Benjamin, et al. Hydraulically amplified self-healing electrostatic actuators with muscle-like performance. *Science*, 359(6371):61–65, 2018.

[3] Maxwell Ahlquist, Rianna Jitosho, Jiawen Bao, and Allison M Okamura. phlosar: a portable, high-flow pressure supply and regulator enabling untethered operation of large pneumatic soft robots. In *2024 IEEE 7th International Conference on Soft Robotics (RoboSoft)*, pages 28–33. Ieee, 2024.

[4] Yara Almubarak and Yonas Tadesse. Twisted and coiled polymer (tcp) muscles embedded in silicone elastomer for use in soft robot. *International Journal of Intelligent Robotics and Applications*, 1(3):352–368, 2017.

[5] Jorge Angeles. *Fundamentals of robotic mechanical systems: theory, methods, and algorithms*. Springer, 2003.

[6] I. Arruego, M. T. Guerrero, S. Rodriguez, J. Martinez-Oter, J. J. Jimenez, et al. Owls: a ten-year history in optical wireless links for intra-satellite communications. *IEEE Journal on Selected Areas in Communications*, 27(9):1599–1611, 2009.

[7] Cameron A Aubin, Benjamin Gorissen, Edoardo Milana, Philip R Buskohl, Nathan Lazarus, et al. Towards enduring autonomous robots via embodied energy. *Nature*, 602(7897):393–402, 2022.

[8] Yoseph Bar-Cohen. Electroactive polymers as artificial muscles: capabilities, potentials and challenges. In *Robotics 2000*, pages 188–196, 2000.

[9] Martin Philip Bendsoe and Ole Sigmund. *Topology optimization: theory, methods, and applications*. Springer Science & Business Media, 2003.

[10] James M Bern, Pol Banzet, Roi Poranne, and Stelian Coros. Trajectory optimization for cable-driven soft robot locomotion. In *Robotics: Science and Systems*, volume 1, 2019.

[11] James M Bern, Yannick Schnider, Pol Banzet, Nitish Kumar, and Stelian Coros. Soft robot control with a learned differentiable model. In *2020 3rd IEEE International Conference on Soft Robotics (RoboSoft)*, pages 417–423. Ieee, 2020.

[12] Ankit Bhatia, Aaron M Johnson, and Matthew T Mason. Direct drive hands: Force-motion transparency in gripper design. In *Robotics: science and systems*, 2019.

[13] Diego Bianchi, Michele Gabrio Antonelli, Cecilia Laschi, Angelo Maria Sabatini, and Egidio Falotico. Softoss: Learning to throw objects with a soft robot. *IEEE Robotics & Automation Magazine*, 2023.

[14] Antonio Bicchi and Vijay Kumar. Robotic grasping and contact: A review. In *Proceedings 2000 ICRA. Millennium Conference. IEEE International Conference on Robotics and Automation. Symposia Proceedings (Cat. No. 00CH37065)*, volume 1, pages 348–353. Ieee, 2000.

[15] R. Adam Bilodeau and Rebecca K. Kramer. Self-healing and damage resilience for soft robotics: A review. *Frontiers in Robotics and AI*, 4:48, 2017.

[16] D. Blanding. *Exact Constraint: Machine Design Using Kinematic Principles*. ASME Press, 01 1999.

[17] Gerardo Bledt, Matthew J. Powell, Benjamin Katz, Jared Di Carlo, Patrick M. Wensing, et al. Mit cheetah 3: Design and control of a robust, dynamic quadruped robot. In *2018 IEEE/RSJ International Conference on Intelligent Robots and Systems (IROS)*, pages 2245–2252, 2018.

[18] Thiago Boaventura, Gustavo A. Medrano-Cerda, Claudio Semini, Jonas Buchli, and Darwin G. Caldwell. Stability and performance of the compliance controller of the quadruped robot hyq. In *2013 IEEE/RSJ International Conference on Intelligent Robots and Systems*, pages 1458–1464, 2013.

[19] J William Boley, Wim M van Rees, Charles Lissandrello, Mark N Horenstein, Ryan L Truby, et al. Shape-shifting structured lattices via multimaterial 4d printing. *Proceedings of the National Academy of Sciences*, 116(42):20856–20862, 2019.

[20] Amanda Bouman, Muhammad Fadhil Ginting, Nikhilesh Alatur, Matteo Palieri, David D. Fan, et al. Autonomous spot: Long-range autonomous exploration of extreme environments with legged locomotion. In *2020 IEEE/RSJ International Conference on Intelligent Robots and Systems (IROS)*, pages 2518–2525, 2020.

[21] Luzius Brodbeck and Fumiya Iida. An extendible reconfigurable robot based on hot melt adhesives. *Autonomous Robots*, 39(1):87–100, 2015.

[22] Russell G Brown and Randy C Brost. A 3-d modular gripper design tool. *IEEE Transactions on Robotics and Automation*, 15(1):174–186, 1999.

[23] Daniel Bruder, Moritz A Graule, Clark B Teeple, and Robert J Wood. Increasing the payload capacity of soft robot arms by localized stiffening. *Science Robotics*, 8(81):eadf9001, 2023.

[24] Herman Bruyninckx, Sabine Demey, and Vijay Kumar. Generalized stability of compliant grasps. In *Proceedings. 1998 IEEE International Conference on Robotics and Automation (Cat. No. 98CH36146)*, volume 3, pages 2396–2402. Ieee, 1998.

[25] Jonas Buchli, Mrinal Kalakrishnan, Michael Mistry, Peter Pastor, and Stefan Schaal. Compliant quadruped locomotion over rough terrain. In *2009 IEEE/RSJ international conference on Intelligent robots and systems*, pages 814–820. Ieee, 2009.

[26] Trevor L Buckner, Michelle C Yuen, Sang Yup Kim, and Rebecca Kramer-Bottiglio. Enhanced variable stiffness and variable stretchability enabled by phase-changing particulate additives. *Advanced Functional Materials*, 29(50):1903368, 2019.

[27] Samuel A Burden, Thomas Libby, Kaushik Jayaram, Simon Sponberg, and J Maxwell Donelan. Why animals can outrun robots. *Science Robotics*, 9(89):eadi9754, 2024.

[28] Berk Calli, Arjun Singh, Aaron Walsman, Siddhartha Srinivasa, Pieter Abbeel, et al. The ycb object and model set: Towards common benchmarks for manipulation research. In *2015 International Conference on Advanced Robotics (ICAR)*, pages 510–517, Jul 2015.

[29] Berk Calli, Aaron Walsman, Arjun Singh, Siddhartha Srinivasa, Pieter Abbeel, et al. Benchmarking in manipulation research: Using the yale-cmu-berkeley object and model set. *IEEE Robotics & Automation Magazine*, 22(3):36–52, Sep 2015.

[30] Molly Carton. *Design, Fabrication, and Application of Mechanical Metamaterials Using Point Group Symmetries*. PhD thesis, University of Washington, 2024.

[31] Angel X. Chang, Thomas Funkhouser, Leonidas Guibas, Pat Hanrahan, Qixing Huang, et al. ShapeNet: An Information-Rich 3D Model Repository. Technical Report arXiv:1512.03012 [cs.GR], Stanford University — Princeton University — Toyota Technological Institute at Chicago, 2015.

[32] Tianjian Chen, Zhanpeng He, and Matei Ciocarlie. Hardware as policy: Mechanical and computational co-optimization using deep reinforcement learning. *arXiv preprint arXiv:2008.04460*, 2020.

[33] Valerie K Chen, Lillian Chin, Jeana Choi, Annan Zhang, and Daniela Rus. Real-time grocery packing by integrating vision, tactile sensing, and soft fingers. In *2024 IEEE 7th International Conference on Soft Robotics (RoboSoft)*, pages 392–399. Ieee, 2024.

[34] Valerie K Chen, Lillian Chin, Jeana Choi, Annan Zhang, and Daniela Rus. Real-time grocery packing by integrating vision, tactile sensing, and soft fingers. In *2024 IEEE 7th International Conference on Soft Robotics (RoboSoft)*, pages 392–399. Ieee, 2024.

[35] Jake A. Childs and Caleb Rucker. Leveraging geometry to enable high-strength continuum robots. *Frontiers in Robotics and AI*, 8, 2021.

[36] L. Chin, J. Lipton, R. MacCurdy, J. Romanishin, C. Sharma, et al. Compliant electric actuators based on handed shearing auxetics. In *2018 IEEE International Conference on Soft Robotics (RoboSoft)*, pages 100–107, 2018.

[37] L. Chin, M. C. Yuen, J. Lipton, L. H. Trueba, R. Kramer-Bottiglio, et al. A simple electric soft robotic gripper with high-deformation haptic feedback. In *2019 International Conference on Robotics and Automation (ICRA)*, pages 2765–2771, 2019.

[38] Lillian Chin, Felipe Barscevicius, Jeffrey Lipton, and Daniela Rus. Multiplexed manipulation: Versatile multimodal grasping via a hybrid soft gripper. In *2020 IEEE International Conference on Robotics and Automation (ICRA)*, pages 8949–8955. Ieee, 2020.

[39] Lillian Chin, Jeffrey Lipton, Robert MacCurdy, John Romanishin, Chetan Sharma, et al. Compliant electric actuators based on handed shearing auxetics. In *2018 IEEE International Conference on Soft Robotics (RoboSoft)*, pages 100–107. Ieee, 2018.

[40] Lillian Chin, Jeffrey Lipton, Michelle C Yuen, Rebecca Kramer-Bottiglio, and Daniela Rus. Automated recycling separation enabled by soft robotic material classification. In *2019 2nd IEEE International Conference on Soft Robotics (RoboSoft)*, pages 102–107. Ieee, 2019.

[41] Lillian Chin, Michelle C Yuen, Jeffrey Lipton, Luis H Trueba, Rebecca Kramer-Bottiglio, et al. A simple electric soft robotic gripper with high-deformation haptic feedback. In *2019 International Conference on Robotics and Automation (ICRA)*, pages 2765–2771. Ieee, 2019.

[42] Margaret M Coad, Laura H Blumenschein, Sadie Cutler, Javier A Reyna Zepeda, Nicholas D Naclerio, et al. Vine robots. *IEEE Robotics & Automation Magazine*, 27(3):120–132, 2019.

[43] Peter I Corke. A simple and systematic approach to assigning denavit–hartenberg parameters. *IEEE transactions on robotics*, 23(3):590–594, 2007.

[44] Whitney Crooks, Shane Rozen-Levy, Barry Trimmer, Chris Rogers, and William Messner. Passive gripper inspired by manduca sexta and the fin ray® effect. *International Journal of Advanced Robotic Systems*, 14(4):1729881417721155, 2017.

[45] George B Crowley, Xianpai Zeng, and Hai-Jun Su. A 3d printed soft robotic gripper with a variable stiffness enabled by a novel positive pressure layer jamming technology. *IEEE Robotics and Automation Letters*, 7(2):5477–5482, 2022.

[46] Lianshuang Dai, Dongpo Wang, Ting Wang, Qingshan Feng, and Xinqi Yang. Analysis and comparison of long-distance pipeline failures. *Journal of Petroleum Engineering*, 2017(1):3174636, 2017.

[47] Bhaskar Dasgupta and TS1739334 Mruthyunjaya. The stewart platform manipulator: a review. *Mechanism and machine theory*, 35(1):15–40, 2000.

[48] Kalyanmoy Deb, Samir Agrawal, Amrit Pratap, and Tanaka Meyarivan. A fast elitist non-dominated sorting genetic algorithm for multi-objective optimization: Nsga-ii. In *International conference on parallel problem solving from nature*, pages 849–858. Springer, 2000.

[49] Raphael Deimel, Patrick Irmisch, Vincent Wall, and Oliver Brock. Automated co-design of soft hand morphology and control strategy for grasping. In *2017 IEEE/RSJ International Conference on Intelligent Robots and Systems (IROS)*, pages 1213–1218. Ieee, 2017.

[50] Cosimo Della Santina, Manuel G Catalano, Antonio Bicchi, M Ang, O Khatib, et al. Soft robots. *Encyclopedia of Robotics*, 489, 2020.

[51] Cosimo Della Santina, Ryan Landon Truby, and Daniela Rus. Data–driven disturbance observers for estimating external forces on soft robots. *IEEE Robotics and Automation Letters*, 5(4):5717–5724, 2020.

[52] Jacques Denavit and Richard S Hartenberg. A kinematic notation for lower-pair mechanisms based on matrices. *ASME Journal of Applied Mechanics*, 1955.

[53] Krishnamanaswi M Digumarti, Christian Gehring, Stelian Coros, J Hwangbo, and Roland Siegwart. Concurrent optimization of mechanical design and locomotion control of a legged robot. In *Mobile Service Robotics*, pages 315–323. World Scientific, 2014.

[54] Dylan Drotman, Saurabh Jadhav, David Sharp, Christian Chan, and Michael T Tolley. Electronics-free pneumatic circuits for controlling soft-legged robots. *Science Robotics*, 6(51), 2021.

[55] Tao Du, Adriana Schulz, Bo Zhu, Bernd Bickel, and Wojciech Matusik. Computational multicopter design. *ACM Transactions on Graphics (TOG)*, 35(6):1–10, 2016.

[56] Johannes F Elfferich, Dimitra Dodou, and Cosimo Della Santina. Soft robotic grippers for crop handling or harvesting: A review. *IEEE Access*, 10:75428–75443, 2022.

[57] Yahya Elsayed, Augusto Vincensi, Constantina Lekakou, Tao Geng, CM Saaj, et al. Finite element analysis and design optimization of a pneumatically actuating silicone module for robotic surgery applications. *Soft Robotics*, 1(4):255–262, 2014.

[58] G. Fadini, T. Flayols, A. Del Prete, N. Mansard, and P. Souères. Computational design of energy-efficient legged robots: Optimizing for size and actuators. In *2021 IEEE International Conference on Robotics and Automation (ICRA)*, pages 9898–9904, 2021.

[59] Péter Fankhauser and Marco Hutter. Anymal: a unique quadruped robot conquering harsh environments. *Research Features*, (126):54–57, 2018.

[60] Samuel Felton, Michael Tolley, Erik Demaine, Daniela Rus, and Robert Wood. A method for building self-folding machines. *Science*, 345(6197):644–646, 2014.

[61] Anthony V. Fiacco and Garth P. McCormick. The sequential unconstrained minimization technique for nonlinear programing, a primal-dual method. *Manage. Sci.*, 10(2):360–366, jan 1964.

[62] Aman Garg, Ian Good, Daniel Revier, Kevin Airis, and Jeffrey Lipton. Kinematic modeling of handed shearing auxetics via piecewise constant curvature. In *2022 IEEE 5th International Conference on Soft Robotics (RoboSoft)*, pages 423–430. Ieee, 2022.

[63] Ian Good, Tosh Brown-Moore, Aditya Patil, Daniel Revier, and Jeffrey Ian Lipton. Expanding the design space for electrically-driven soft robots through handed shearing auxetics. *arXiv preprint arXiv:2110.00669*, 2021.

[64] Qinghua Guan, Francesco Stella, Cosimo Della Santina, Jinsong Leng, and Josie Hughes. Trimmed helicoids: an architectured soft structure yielding soft robots with high precision, large workspace, and compliant interactions. *npj Robotics*, 1(1):4, 2023.

[65] PDSH Gunawardane, N Budiardjo, G Alici, CW de Silva, and M Chiao. Thermoelastic strain-limiting layers to actively-control soft actuator trajectories. In *2022 IEEE 5th International Conference on Soft Robotics (RoboSoft)*, pages 48–53. Ieee, 2022.

[66] Varan Gupta, Rithul Perathara, Aditya K Chaurasiya, and Jitendra P Khatait. Design and analysis of a flexure based passive gripper. *Precision Engineering*, 56:537–548, 2019.

[67] Huy Ha, Shubham Agrawal, and Shuran Song. Fit2form: 3d generative model for robot gripper form design. *arXiv preprint arXiv:2011.06498*, 2020.

[68] Sehoon Ha, Stelian Coros, Alexander Alspach, Joohyung Kim, and Katsu Yamane. Joint optimization of robot design and motion parameters using the implicit function theorem. In *Robotics: Science and systems*, volume 8, 2017.

[69] Michael W. Hannan and Ian D. Walker. Kinematics and the implementation of an elephant's trunk manipulator and other continuum style robots. *Journal of Robotic Systems*, 20(2):45–63, 2003.

[70] Jiang Hao, Xinghua Liu, Xiaotong Chen, Zhanchi Wang, Yusong Jin, et al. Design and simulation analysis of a soft manipulator based on honeycomb pneumatic networks. pages 350–356, 12 2016.

[71] Elliot Hawkes, B An, Nadia M Benbernou, H Tanaka, Sangbae Kim, et al. Programmable matter by folding. *Proceedings of the National Academy of Sciences*, 107(28):12441–12445, 2010.

[72] Christopher Hazard, Nancy Pollard, and Stelian Coros. Automated design of manipulators for in-hand tasks. In *2018 IEEE-RAS 18th International Conference on Humanoid Robots (Humanoids)*, pages 1–8. Ieee, 2018.

[73] Qiguang He, Zhijian Wang, Yang Wang, Adriane Minori, Michael T Tolley, et al. Electrically controlled liquid crystal elastomer–based soft tubular actuator with multimodal actuation. *Science advances*, 5(10):eaax5746, 2019.

[74] Stephanie Hendrixson. Laser-sintered grippers solve robotic packing challenges, 4 2016.

[75] Clinton G. Hobart, Anirban Mazumdar, Steven J. Spencer, Morgan Quigley, Jesper P. Smith, et al. Achieving versatile energy efficiency with the wanderer biped robot. *IEEE Transactions on Robotics*, 36(3):959–966, 2020.

[76] Dónal P Holland, Evelyn J Park, Panagiotis Polygerinos, Gareth J Bennett, and Conor J Walsh. The soft robotics toolkit: Shared resources for research and design. *Soft Robotics*, 1(3):224–230, 2014.

[77] Mohammadali Honarpardaz, Martin Meier, and Robert Haschke. Fast grasp tool design: From force to form closure. In *2017 13th IEEE Conference on Automation Science and Engineering (CASE)*, pages 782–788. Ieee, 2017.

[78] Mohammadali Honarpardaz, Mehdi Tarkian, Johan Ölvander, and Xiaolong Feng. Finger design automation for industrial robot grippers: A review. *Robotics and Autonomous Systems*, 87:104–119, 2017.

[79] Xiaonan Huang, Kitty Kumar, Mohammad K Jawed, Amir Mohammadi Nasab, Zisheng Ye, et al. Highly dynamic shape memory alloy actuator for fast moving soft robots. *Advanced Materials Technologies*, 4(4):1800540, 2019.

[80] Joshua D Hubbard, Ruben Acevedo, Kristen M Edwards, Abdullah T Alsharhan, Ziteng Wen, et al. Fully 3d-printed soft robots with integrated fluidic circuitry. *Science Advances*, 7(29):eabe5257, 2021.

[81] William Hunter et al. Topy - topology optimization with python. `https://github.com/williamhunter/topy`, 2017.

[82] Marco Hutter, Christian Gehring, Dominic Jud, Andreas Lauber, C Dario Bellicoso, et al. Anymal-a highly mobile and dynamic quadrupedal robot. In *2016 IEEE/RSJ international conference on intelligent robots and systems (IROS)*, pages 38–44. Ieee, 2016.

[83] Filip Ilievski, Aaron D Mazzeo, Robert F Shepherd, Xin Chen, and George McClelland Whitesides. Soft robotics for chemists. *Angewandte Chemie International Editiion*, 2011.

[84] Alec Jacobson, Daniele Panozzo, et al. libigl: A simple C++ geometry processing library, 2018. https://libigl.github.io/.

[85] Snehal Jain, Saikrishna Dontu, Joanne Ee Mei Teoh, and Pablo Valdivia Y Alvarado. A multimodal, reconfigurable workspace soft gripper for advanced grasping tasks. *Soft Robotics*, 10(3):527–544, 2023. Pmid: 36346280.

[86] Hao Jiang, Zhanchi Wang, Yusong Jin, Xiaotong Chen, Peijin Li, et al. Hierarchical control of soft manipulators towards unstructured interactions. *The International Journal of Robotics Research*, 40(1):411–434, 2021.

[87] Yongkang Jiang, Diansheng Chen, Che Liu, and Jian Li. Chain-like granular jamming: a novel stiffness-programmable mechanism for soft robotics. *Soft robotics*, 6(1):118–132, 2019.

[88] Steven G. Johnson. The NLopt nonlinear-optimization package, 2014. http://github.com/stevengj/nlopt.

[89] B. A. Jones and I. D. Walker. Kinematics for multisection continuum robots. *IEEE Transactions on Robotics*, 22(1):43–55, 2006.

[90] Pranav Kaarthik, Francesco L Sanchez, James Avtges, and Ryan L Truby. Motorized, untethered soft robots via 3d printed auxetics. *Soft Matter*, 18(43):8229–8237, 2022.

[91] Pranav Kaarthik, Francesco L. Sanchez, James Avtges, and Ryan L. Truby. Motorized, untethered soft robots via 3d printed auxetics. *Soft Matter*, 18:8229–8237, 2022.

[92] P Kaelo and MM Ali. Some variants of the controlled random search algorithm for global optimization. *Journal of optimization theory and applications*, 130(2):253–264, 2006.

[93] Minchae Kang, Ye-Ji Han, and Min-Woo Han. A shape memory alloy-based soft actuator mimicking an elephant's trunk. *Polymers*, 15(5):1126, 2023.

[94] Robert K Katzschmann, Cosimo Della Santina, Yasunori Toshimitsu, Antonio Bicchi, and Daniela Rus. Dynamic motion control of multi-segment soft robots using piecewise constant curvature matched with an augmented rigid body model. In *2019 2nd IEEE International Conference on Soft Robotics (RoboSoft)*, pages 454–461. Ieee, 2019.

[95] Robert K. Katzschmann, Cosimo Della Santina, Yasunori Toshimitsu, Antonio Bicchi, and Daniela Rus. Dynamic motion control of multi-segment soft robots using piecewise constant curvature matched with an augmented rigid body model. In *2019 2nd IEEE International Conference on Soft Robotics (RoboSoft)*, pages 454–461, 2019.

[96] Christoph Keplinger, Jeong-Yun Sun, Choon Chiang Foo, Philipp Rothemund, George M Whitesides, et al. Stretchable, transparent, ionic conductors. *Science*, 341(6149):984–987, 2013.

[97] Jake Ketchum, Sophia Schiffer, Muchen Sun, Pranav Kaarthik, Ryan L Truby, et al. Automated gait generation for walking, soft robotic quadrupeds. In *2023 IEEE/RSJ International Conference on Intelligent Robots and Systems (IROS)*, pages 10245–10251. Ieee, 2023.

[98] Sangbae Kim, Cecilia Laschi, and Barry Trimmer. Soft robotics: A bioinspired evolution in robotics. *Trends in Biotechnology*, 31(5):287–294, 2013.

[99] Taekyoung Kim, Pranav Kaarthik, and Ryan L. Truby. A flexible, architected soft robotic actuator for motorized extensional motion. *Advanced Intelligent Systems*, n/a(n/a):2300866.

[100] Taekyoung Kim, Pranav Kaarthik, and Ryan L Truby. A flexible, architected soft robotic actuator for motorized extensional motion. *Advanced Intelligent Systems*, page 2300866, 2024.

[101] Heinrich Kruger and A Frank van der Stappen. Partial closure grasps: Metrics and computation. In *2011 IEEE International Conference on Robotics and Automation*, pages 5024–5030. Ieee, 2011.

[102] Heinrich Kruger and A. Frank van der Stappen. Partial closure grasps: Metrics and computation. In *2011 IEEE International Conference on Robotics and Automation*, pages 5024–5030, 2011.

[103] Y. Lee, W.J. Song, and J.-Y. Sun. Hydrogel soft robotics. *Materials Today Physics*, 15:100258, 2020.

[104] S. Levine, C. Finn, T. Darrell, and P. Abbeel. End-to-end training of deep visuomotor policies. *Journal of Machine Learning Research (JMLR)*, 2016.

[105] Shucong Li, Gabriele Librandi, Yuxing Yao, Austin J Richard, Alyssha Schneider-Yamamura, et al. Controlling liquid crystal orientations for programmable anisotropic transformations in cellular microstructures. *Advanced Materials*, page 2105024, 2021.

[106] Shuguang Li, Samer A Awale, Katharine E Bacher, Thomas J Buchner, Cosimo Della Santina, et al. Scaling up soft robotics: a meter-scale, modular, and reconfigurable soft robotic system. *Soft Robotics*, 9(2):324–336, 2022.

[107] Shuguang Li, John J Stampfli, Helen J Xu, Elian Malkin, Evelin Villegas Diaz, et al. A vacuum-driven origami "magic-ball" soft gripper. In *2019 International Conference on Robotics and Automation (ICRA)*, pages 7401–7408. Ieee, 2019.

[108] Shuguang Li, Daniel M Vogt, Daniela Rus, and Robert J Wood. Fluid-driven origami-inspired artificial muscles. *Proceedings of the National academy of Sciences*, 114(50):13132–13137, 2017.

[109] Jeffrey Lipton, Lillian Chin, Jacob Miske, and Daniela Rus. Modular volumetric actuators using motorized auxetics. In *2019 IEEE/RSJ International Conference on Intelligent Robots and Systems (IROS)*, pages 7460–7466. Ieee, 2019.

[110] Jeffrey Ian Lipton, Sarah Angle, Rona Elinor Banai, Eliad Peretz, and Hod Lipson. Electrically actuated hydraulic solids. *Advanced Engineering Materials*, 18(10):1710–1715, 2016.

[111] Jeffrey Ian Lipton, Robert MacCurdy, Zachary Manchester, Lillian Chin, Daniel Cellucci, et al. Handedness in shearing auxetics creates rigid and compliant structures. *Science*, 360(6389):632–635, 2018.

[112] Jeffrey Ian Lipton, Robert MacCurdy, Zachary Manchester, Lillian Chin, Daniel Cellucci, et al. Handedness in shearing auxetics creates rigid and compliant structures. *Science*, 360(6389):632–635, 2018.

[113] Wenbo Liu, Youning Duo, Jiaqi Liu, Feiyang Yuan, Lei Li, et al. Touchless interactive teaching of soft robots through flexible bimodal sensory interfaces. *Nature communications*, 13(1):5030, 2022.

[114] Amin Lotfiani, Huichan Zhao, Zhufeng Shao, and Xili Yi. Torsional stiffness improvement of a soft pneumatic finger using embedded skeleton. *Journal of Mechanisms and Robotics*, 12(1):011016, 2020.

[115] Kevin Sebastian Luck, Heni Ben Amor, and Roberto Calandra. Data-efficient co-adaptation of morphology and behaviour with deep reinforcement learning. In *Conference on Robot Learning*, pages 854–869. Pmlr, 2020.

[116] Pingchuan Ma, Tao Du, John Z. Zhang, Kui Wu, Andrew Spielberg, et al. Diffaqua: A differentiable computational design pipeline for soft underwater swimmers with shape interpolation. *ACM Trans. Graph.*, 40(4), jul 2021.

[117] Raymond R Ma and Aaron M Dollar. On dexterity and dexterous manipulation. In *2011 15th International Conference on Advanced Robotics (ICAR)*, pages 1–7. Ieee, 2011.

[118] J. Mahler, J. Liang, S. Niyaz, M. Laskey, R. Doan, et al. Dex-Net 2.0: Deep learning to plan robust grasps with synthetic point clouds and analytic grasp metrics. 2017.

[119] Jeremy Maitin-Shepard, Marco Cusumano-Towner, Jinna Lei, and Pieter Abbeel. Cloth grasp point detection based on multiple-view geometric cues with application to robotic towel folding. In *2010 IEEE International Conference on Robotics and Automation*, pages 2308–2315. Ieee, 2010.

[120] Ramses V Martinez, Ana C Glavan, Christoph Keplinger, Alexis I Oyetibo, and George M Whitesides. Soft actuators and robots that are resistant to mechanical damage. *Advanced Functional Materials*, 24(20):3003–3010, 2014.

[121] Gianmarco Mengaldo, Federico Renda, Steven L Brunton, Moritz Bächer, Marcello Calisti, et al. A concise guide to modelling the physics of embodied intelligence in soft robotics. *Nature Reviews Physics*, 4(9):595–610, 2022.

[122] Aslan Miriyev, Kenneth Stack, and Hod Lipson. Soft material for soft actuators. *Nature communications*, 8(1):1–8, 2017.

[123] Anand Kumar Mishra, Emanuela Del Dottore, Ali Sadeghi, Alessio Mondini, and Barbara Mazzolai. Simba: Tendon-driven modular continuum arm with soft reconfigurable gripper. *Frontiers in Robotics and AI*, 4:4, 2017.

[124] Bobak Mosadegh, Panagiotis Polygerinos, Christoph Keplinger, Sophia Wennstedt, Robert F Shepherd, et al. Pneumatic networks for soft robotics that actuate rapidly. *Advanced functional materials*, 24(15):2163–2170, 2014.

[125] Arsalan Mousavian, Clemens Eppner, and Dieter Fox. 6-DOF GraspNet: Variational Grasp Generation for Object Manipulation. In *International Conference on Computer Vision*, 2019.

[126] Hossein Mousazadeh, Alireza Keyhani, Arzhang Javadi, Hossein Mobli, Karen Abrinia, et al. A review of principle and sun-tracking methods for maximizing solar systems output. *Renewable and Sustainable Energy Reviews*, 13(8):1800–1818, 2009.

[127] Caio Mucchiani, Monroe Kennedy, Mark Yim, and Jungwon Seo. Object picking through in-hand manipulation using passive end-effectors with zero mobility. *IEEE Robotics and Automation Letters*, 3(2):1096–1103, 2018.

[128] Caio Mucchiani and Mark Yim. Dynamic grasping for object picking using passive zero-dof end-effectors. *IEEE Robotics and Automation Letters*, 6(2):3089–3096, 2021.

[129] A. Murali, A. Mousavian, C. Eppner, C. Paxton, and D. Fox. 6-DOF grasping for target-driven object manipulation in clutter. 2020.

[130] A. Nagabandi, K. Konolige, S. Levine, and V. Kumar. Deep dynamics models for learning dexterous manipulation. 2019.

[131] Kenji Nagaoka, Hayato Minote, Kyohei Maruya, Yuki Shirai, Kazuya Yoshida, et al. Passive spine gripper for free-climbing robot in extreme terrain. *IEEE Robotics and Automation Letters*, 3(3):1765–1770, 2018.

[132] Mark Naves, Dannis Michel Brouwer, and Ronald GKM Aarts. Building block-based spatial topology synthesis method for large-stroke flexure hinges. *Journal of mechanisms and robotics*, 9(4):041006, 2017.

[133] Kaitlin Oliver-Butler, John Till, and Caleb Rucker. Continuum robot stiffness under external loads and prescribed tendon displacements. *IEEE Transactions on Robotics*, 35(2):403–419, 2019.

[134] Cagdas D Onal and Daniela Rus. A modular approach to soft robots. In *2012 4th IEEE RAS & EMBS International Conference on Biomedical Robotics and Biomechatronics (BioRob)*, pages 1038–1045. Ieee, 2012.

[135] Chinedu I Ossai, Brian Boswell, and Ian J Davies. Pipeline failures in corrosive environments–a conceptual analysis of trends and effects. *Engineering Failure Analysis*, 53:36–58, 2015.

[136] Xinlei Pan, Animesh Garg, Animashree Anandkumar, and Yuke Zhu. Emergent hand morphology and control from optimizing robust grasps of diverse objects. *arXiv preprint arXiv:2012.12209*, 2020.

[137] Dalibor Petković, Nenad D Pavlović, Shahaboddin Shamshirband, and Nor Badrul Anuar. Development of a new type of passively adaptive compliant gripper. *Industrial Robot: An International Journal*, 2013.

[138] Panagiotis Polygerinos, Nikolaus Correll, Stephen A. Morin, Bobak Mosadegh, Cagdas D. Onal, et al. Soft robotics: Review of fluid-driven intrinsically soft devices; manufacturing, sensing, control, and applications in human-robot interaction. *Advanced Engineering Materials*, 19(12):1700016, 2017.

[139] Panagiotis Polygerinos, Stacey Lyne, Zheng Wang, Luis Fernando Nicolini, Bobak Mosadegh, et al. Towards a soft pneumatic glove for hand rehabilitation. In *2013 IEEE/RSJ International Conference on Intelligent Robots and Systems*, pages 1512–1517. Ieee, 2013.

[140] Polyvios Polygerinos, Nikolaus Correll, Stephen A Morin, Bobak Mosadegh, Cagdas D Onal, et al. Soft robotics: Review of fluid-driven intrinsically soft devices; manufacturing, sensing, control, and applications in human-robot interaction. *Advanced Engineering Materials*, 19(12):1700016, 2017.

[141] Gill A Pratt and Matthew M Williamson. Series elastic actuators. In *Proceedings 1995 IEEE/RSJ international conference on intelligent robots and systems. Human robot interaction and cooperative robots*, volume 1, pages 399–406. Ieee, 1995.

[142] Zengyi Qin, Kuan Fang, Yuke Zhu, Li Fei-Fei, and Silvio Savarese. Keto: Learning keypoint representations for tool manipulation. 2020.

[143] R. Rahmatizadeh, P. Abolghasemi, L. Boloni, and S. Levine. Vision-based multi-task manipulation for inexpensive robots using end-to-end learning from demonstration. 2018.

[144] Federico Renda, Michele Giorelli, Marcello Calisti, Matteo Cianchetti, and Cecilia Laschi. Dynamic model of a multibending soft robot arm driven by cables. *IEEE Transactions on Robotics*, 30(5):1109–1122, 2014.

[145] Siavash Rezazadeh, Andy Abate, Ross L. Hatton, and Jonathan W. Hurst. Robot leg design: A constructive framework. *IEEE Access*, 6:54369–54387, 2018.

[146] R.C. Richardson, M.C. Levesley, M.D. Brown, J.A. Hawkes, K. Watterson, et al. Control of ionic polymer metal composites. *IEEE/ASME Transactions on Mechatronics*, 8(2):245–253, 2003.

[147] III Robert J. Webster and Bryan A. Jones. Design and kinematic modeling of constant curvature continuum robots: A review. *The International Journal of Robotics Research*, 29(13):1661–1683, 2010.

[148] David W Robinson, Jerry E Pratt, Daniel J Paluska, and Gill A Pratt. Series elastic actuator development for a biomimetic walking robot. In *1999 IEEE/ASME International Conference on Advanced Intelligent Mechatronics (Cat. No. 99TH8399)*, pages 561–568. Ieee, 1999.

[149] Alberto Rodriguez, Matthew T Mason, and Steve Ferry. From caging to grasping. *The International Journal of Robotics Research*, 31(7):886–900, 2012.

[150] Jelle Rommers, Volkert van der Wijk, and Just L Herder. A new type of spherical flexure joint based on tetrahedron elements. *Precision Engineering*, 71:130–140, 2021.

[151] Samuel Rosset and Herbert R Shea. Flexible and stretchable electrodes for dielectric elastomer actuators. *Applied Physics A*, 110:281–307, 2013.

[152] P. Roth, A. Georgiev, and H. Boudinov. Design and construction of a system for sun-tracking. *Renewable Energy*, 29(3):393–402, 2004.

[153] Daniela Rus and Michael T Tolley. Design, fabrication and control of soft robots. *Nature*, 521(7553):467–475, 2015.

[154] Daniela Rus and Michael T. Tolley. Design, fabrication and control of soft robots. *Nature*, 521(7553):467–475, May 2015.

[155] Rob BN Scharff, Jun Wu, Jo MP Geraedts, and Charlie CL Wang. Reducing out-of-plane deformation of soft robotic actuators for stable grasping. In *2019 2nd IEEE International Conference on Soft Robotics (RoboSoft)*, pages 265–270. Ieee, 2019.

[156] François Schmitt, Olivier Piccin, Laurent Barbé, and Bernard Bayle. Soft robots manufacturing: A review. *Frontiers in Robotics and AI*, 5:84, 2018.

[157] Andreas Schroeffer, Christoph Rehekampff, and Tim C Lueth. An automated design approach for task-specific two finger grippers for industrial applications. In *2019 IEEE International Conference on Robotics and Biomimetics (ROBIO)*, pages 184–189. Ieee, 2019.

[158] Arthur Seibel, Mert Yıldız, and Berkan Zorlubaş. A gecko-inspired soft passive gripper. *Biomimetics*, 5(2):12, 2020.

[159] Daniel Seita, Nawid Jamali, Michael Laskey, Ajay Kumar Tanwani, Ron Berenstein, et al. Deep transfer learning of pick points on fabric for robot bed-making. 2019.

[160] Silvia Sellán, Noam Aigerman, and Alec Jacobson. Swept volumes via spacetime numerical continuation. *ACM Transactions on Graphics*, 2021.

[161] Jungwon Seo, Mark Yim, and Vijay Kumar. A theory on grasping objects using effectors with curved contact surfaces and its application to whole-arm grasping. *The International Journal of Robotics Research*, 35(9):1080–1102, 2016.

[162] Sangok Seok, Albert Wang, Meng Yee Chuah, Dong Jin Hyun, Jongwoo Lee, et al. Design principles for energy-efficient legged locomotion and implementation on the mit cheetah robot. *Ieee/asme transactions on mechatronics*, 20(3):1117–1129, 2014.

[163] Zequn Shen, Feifei Chen, Xiangyang Zhu, Ken-Tye Yong, and Guoying Gu. Stimuli-responsive functional materials for soft robotics. *Journal of Materials Chemistry B*, 8(39):8972–8991, 2020.

[164] Jun Shintake, Vito Cacucciolo, Dario Floreano, and Herbert Shea. Soft robotic grippers. *Advanced materials*, 30(29):1707035, 2018.

[165] Jun Shintake, Vito Cacucciolo, Dario Floreano, and Herbert Shea. Soft robotic grippers. *Advanced Materials*, 30(29):1707035, 2018.

[166] Bruno Siciliano and Oussama Khatib, editors. *Springer Handbook of Robotics*. Springer, 2016.

[167] Luca Somm, David Hahn, Nitish Kumar, and Stelian Coros. Expanding foam as the material for fabrication, prototyping and experimental assessment of low-cost soft robots with embedded sensing. *IEEE Robotics and Automation Letters*, 4(2):761–768, 2019.

[168] Andrew Spielberg, Allan Zhao, Yuanming Hu, Tao Du, Wojciech Matusik, et al. Learning-in-the-loop optimization: End-to-end control and co-design of soft robots through learned deep latent representations. *Advances in Neural Information Processing Systems*, 32:8284–8294, 2019.

[169] Francesco Stella and Josie Hughes. The science of soft robot design: A review of motivations, methods and enabling technologies. *Frontiers in Robotics and AI*, 9:1059026, 2023.

[170] Kerry Stevenson. What every 3d printing company should be doing. Online, November 2019.

[171] Maximilian Stölzle, Sonal Santosh Baberwal, Daniela Rus, Shirley Coyle, and Cosimo Della Santina. Guiding soft robots with motor-imagery brain signals and impedance control. In *2024 IEEE 7th International Conference on Soft Robotics (RoboSoft)*, pages 276–283, 2024.

[172] Maximilian Stölzle, Lillian Chin, Ryan L Truby, Daniela Rus, and Cosimo Della Santina. Modelling handed shearing auxetics: Selective piecewise constant strain kinematics and dynamic simulation. In *2023 IEEE International Conference on Soft Robotics (RoboSoft)*, pages 1–8. Ieee, 2023.

[173] Renbo Su, Yingjun Tian, Mingwei Du, and Charlie CL Wang. Optimizing out-of-plane stiffness for soft grippers. *IEEE Robotics and Automation Letters*, 7(4):10430–10437, 2022.

[174] Seref Kemal Talas, Bora Alp Baydere, Timur Altinsoy, Cem Tutcu, and Evren Samur. Design and development of a growing pneumatic soft robot. *Soft robotics*, 7(4):521–533, 2020.

[175] Jie Tan, Tingnan Zhang, Erwin Coumans, Atil Iscen, Yunfei Bai, et al. Sim-to-real: Learning agile locomotion for quadruped robots. *arXiv preprint arXiv:1804.10332*, 2018.

[176] Charbel Tawk, Rahim Mutlu, and Gursel Alici. A 3d printed modular soft gripper integrated with metamaterials for conformal grasping. *Frontiers in Robotics and AI*, 8, 2022.

[177] Andreas ten Pas, Marcus Gualtieri, Kate Saenko, and Robert Platt. Grasp pose detection in point clouds. *The International Journal of Robotics Research*, 36(13-14):1455–1473, 2017.

[178] Seppe Terryn, Joost Brancart, Dirk Lefeber, Guy Van Assche, and Bram Vanderborght. Self-healing soft pneumatic robots. *Sci. Robot.*, 2(9), 2017.

[179] The CGAL Project. *CGAL User and Reference Manual*. CGAL Editorial Board, 5.3.1 edition, 2021.

[180] Sawyer Thomas. *From Arteries to Space Structures: How Tiling Mechanisms Leads to Custom Adaptation*. PhD thesis, University of Washington, 2024. unpublished as of the time of writing.

[181] Minh Tran, Lukas Gabert, Sarah Hood, and Tommaso Lenzi. A lightweight robotic leg prosthesis replicating the biomechanics of the knee, ankle, and toe joint. *Science robotics*, 7(72):eabo3996, 2022.

[182] R. L. Truby, L. Chin, and D. Rus. A recipe for electrically-driven soft robots via 3d printed handed shearing auxetics. *IEEE Robotics and Automation Letters*, 6(2):795–802, 2021.

[183] Ryan L Truby, Lillian Chin, and Daniela Rus. A recipe for electrically-driven soft robots via 3d printed handed shearing auxetics. *IEEE Robotics and Automation Letters*, 6(2):795–802, 2021.

[184] V. A. Tucker. The energetic cost of moving about: Walking and running are extremely inefficient forms of locomotion. much greater efficiency is achieved by birds, fish–and bicyclists. *American Scientist*, 63(4):413–419, 1975.

[185] Nathan S Usevitch, Zachary M Hammond, Mac Schwager, Allison M Okamura, Elliot W Hawkes, et al. An untethered isoperimetric soft robot. *Science Robotics*, 5(40):eaaz0492, 2020.

[186] B. Vanderborght, A. Albu-Schaeffer, A. Bicchi, E. Burdet, D. G. Caldwell, et al. Variable impedance actuators: A review. 61(12):1601–1614.

[187] VB Velasco and Wyatt S Newman. Computer-assisted gripper and fixture customization using rapid-prototyping technology. In *Proceedings. 1998 IEEE International Conference on Robotics and Automation (Cat. No. 98CH36146)*, volume 4, pages 3658–3664. Ieee, 1998.

[188] Francesco Visentin, Saravana Prashanth Murali Babu, Fabian Meder, and Barbara Mazzolai. Selective stiffening in soft actuators by triggered phase transition of hydrogel-filled elastomers. *Advanced Functional Materials*, 31(32):2101121, 2021.

[189] Hung Quy Vu, Xiaoxiang Yu, Fumiya Iida, and Rolf Pfeifer. Improving energy efficiency of hopping locomotion by using a variable stiffness actuator. *IEEE/ASME Transactions on Mechatronics*, 21(1):472–486, 2016.

[190] Zhanwei Wang, Seppe Terryn, Julie Legrand, Pasquale Ferrentino, Seyedreza Kashef Tabrizian, et al. Topology optimized multi-material self-healing actuator with reduced out of plane deformation. In *2022 IEEE/RSJ International Conference on Intelligent Robots and Systems*, 2022.

[191] Robert J Webster III and Bryan A Jones. Design and kinematic modeling of constant curvature continuum robots: A review. *The International Journal of Robotics Research*, 29(13):1661–1683, 2010.

[192] Michael Wehner, Ryan L Truby, Daniel J Fitzgerald, Bobak Mosadegh, George M Whitesides, et al. An integrated design and fabrication strategy for entirely soft, autonomous robots. *Nature*, 536(7617):451–455, 2016.

[193] Zhexin Xie, Feiyang Yuan, Jiaqi Liu, Lufeng Tian, Bohan Chen, et al. Octopus-inspired sensorized soft arm for environmental interaction. *Science Robotics*, 8(84):eadh7852, 2023.

[194] Jie Xu, Tao Chen, Lara Zlokapa, Michael Foshey, Wojciech Matusik, et al. An end-to-end differentiable framework for contact-aware robot design. In *Robotics: Science and Systems*, 2021.

[195] Rui Wu Xu, Kai Chin Hsieh, Un Hou Chan, Hoi Un Cheang, Wei Kai Shi, et al. Analytical review on developing progress of the quadruped robot industry and gaits research. In *2022 8th International Conference on Automation, Robotics and Applications (ICARA)*, pages 1–8, 2022.

[196] Guang-Zhong Yang, Jim Bellingham, Pierre E Dupont, Peer Fischer, Luciano Floridi, et al. The grand challenges of science robotics. *Science robotics*, 3(14):eaar7650, 2018.

[197] Liu Yang, Zhilei Zhang, Zengzhi Zhang, Yuzhong Lou, Shijie Han, et al. Design of heavy-load soft robots based on a dual biomimetic structure. *Biomimetics*, 9(7):398, 2024.

[198] Oncay Yasa, Yasunori Toshimitsu, Mike Y Michelis, Lewis S Jones, Miriam Filippi, et al. An overview of soft robotics. *Annual Review of Control, Robotics, and Autonomous Systems*, 6(1):1–29, 2023.

[199] Qifan Yu and Nick Gravish. Multimodal locomotion in a soft robot through hierarchical actuation. *Soft Robotics*, 11(1):21–31, 2024.

[200] Haijie Zhang, Elisha Lerner, Bo Cheng, and Jianguo Zhao. Compliant bistable grippers enable passive perching for micro aerial vehicles. *IEEE/ASME Transactions on Mechatronics*, 2020.

[201] Yuan-Fang Zhang, Ningbin Zhang, Hardik Hingorani, Ningyuan Ding, Dong Wang, et al. Fast-response, stiffness-tunable soft actuator by hybrid multimaterial 3d printing. *Advanced Functional Materials*, 29(15):1806698, 2019.

[202] Zhongkai Zhang, Jeremie Dequidt, Alexandre Kruszewski, Frederick Largilliere, and Christian Duriez. Kinematic modeling and observer based control of soft robot using real-time finite element method. In *2016 IEEE/RSJ International Conference on Intelligent Robots and Systems (IROS)*, pages 5509–5514. Ieee, 2016.

[203] Allan Zhao, Jie Xu, Mina Konaković-Luković, Josephine Hughes, Andrew Spielberg, et al. Robogrammar: graph grammar for terrain-optimized robot design. *ACM Transactions on Graphics (TOG)*, 39(6):1–16, 2020.

[204] Luyang Zhao, Yijia Wu, Wenzhong Yan, Weishu Zhan, Xiaonan Huang, et al. Starblocks: Soft actuated self-connecting blocks for building deformable lattice structures. *IEEE Robotics and Automation Letters*, 8(8):4521–4528, 2023.

[205] Bo Zhu, Mélina Skouras, Desai Chen, and Wojciech Matusik. Two-scale topology optimization with microstructures, 2017.

Appendix A

COMPUTATIONAL DESIGN OF PASSIVE GRIPPERS

A.1 Summary

This work proposes a novel generative design tool for passive grippers—robot end effectors that have no additional actuation and instead leverage the existing degrees of freedom in a robotic arm to perform grasping tasks. Passive grippers are used because they offer interesting trade-offs between cost and capabilities. However, existing designs are limited in the types of shapes that can be grasped. This work proposes to use rapid-manufacturing and design optimization to expand the space of shapes that can be passively grasped. Our novel generative design algorithm takes in an object and its positioning with respect to a robotic arm and generates a 3D printable passive gripper that can stably pick the object up. To achieve this, we address the key challenge of jointly optimizing the shape and the insert trajectory to ensure a passively stable grasp. We evaluate our method on a testing suite of 22 objects (23 experiments), all of which were evaluated with physical experiments to bridge the virtual-to-real gap. Code and data are at

A.2 introduction

Passive grippers are end-effectors with no actuation. They leverage the existing degrees of freedom in a robotic arm to perform grasping tasks. Among the robotics literature, there has been a growing interest in such grasping techniques as they: reduce the manufacturing and deployment cost when compared to active grippers; have lower energy consumption since they do not require continuous power; and enable easier human-robot-interaction as anything passively grasped can be removed by a human without changing the robot state. A fundamental limitation to the widespread use of passive grippers, however, is that they

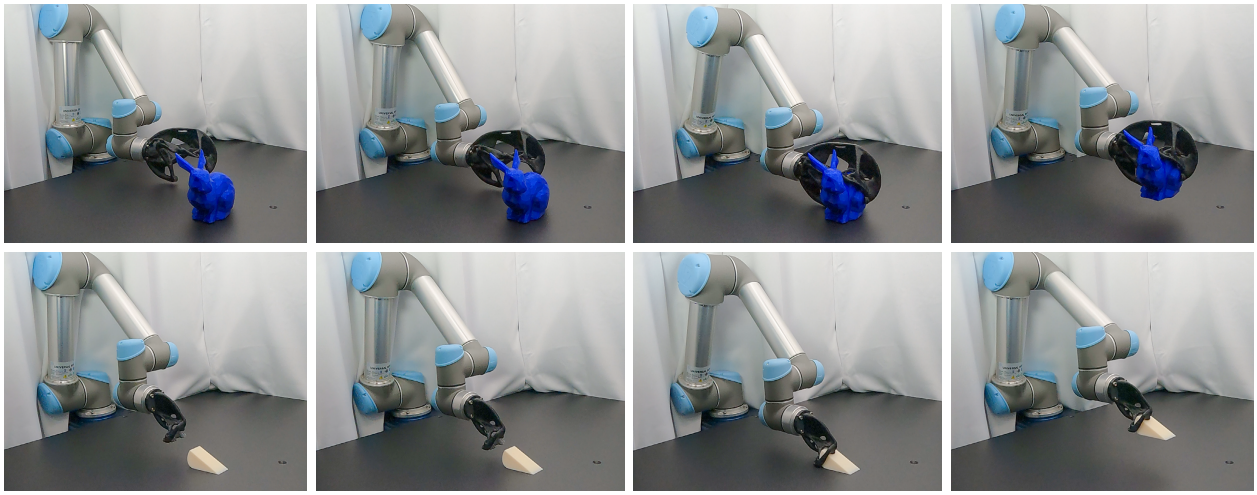

Figure A.1: We present an automated algorithm for designing passive grippers given a target object and its positioning. As our algorithm co-designs both the gripper shape and the insert trajectory, our approach broadens the space of shapes that can be passively grasped, compared to existing methods. The figure shows two of the 21 grippers (out of 23) that can successfully pick up the object in reality.

are currently significantly restricted in the types of shapes that can be grasped.

Motivating this work is the insight that rapid-manufacturing and design optimization can be used to expand the space of shapes that can be passively grasped. We propose an algorithm that, given an input shape, can automatically generate a 3D printable custom gripper and an accompanying grasp insertion trajectory for stable pickup. This approach is directly applicable to a plethora of robotics applications that target repetitive tasks. For example, it can be used for task-specific tooling of robotic work cells in assembly lines, allowing assembly lines instrumented with simple robotic systems (i.e. systems that lack dexterity) to be easily updated to respond to changes in the product. We can simply optimize and print new passive grippers overnight and re-purpose existing hardware.

The challenge with optimizing a passive gripper for a given input is that (1) there is a valid insert trajectory for making contact with the object and (2) once contact is made, the object can be lifted stably. This implies a large-scale search, nominally at the resolution of the 3D printer, where performance evaluation is expensive to compute since it involves physical evaluation and a nested optimization.

We address these challenges with two fundamental insights that allow us to reduce the complexity of this search. First, we observe that stability is a function of the contact points between the gripper and the object. We call this set of contact points the *grasp configuration* (GC) and we expose it as a design variable that should be optimized. We observe that, given the GC, an insert trajectory must ensure that there exists a gripper whose final insert configuration touches the GC and can be inserted without colliding with the rest of the shape. Based on this observation, our second insight is that we can search for such a trajectory by creating an abstraction of the gripper geometry that reflects such minimal requirements and then running a co-optimization over the space of trajectories and abstracted gripper shapes. The abstraction we propose is a parametric skeleton of infinitesimal thickness that connects the points on the GC to the *flange frame's origin* (FFO) of the robot, the center of where we mount the gripper. This reflects the requirement of a rigid object that is attached to the FFO and makes contact with the selected points.

From these two insights, one could argue for a two-step approach that optimizes the GC for stability and then, co-optimizes the trajectory and the gripper abstraction given the GC. The challenge, however, is that the chance of successfully finding a feasible insertion trajectory depends on the choice of the GC. We therefore propose a strategy for computing a ranked list of stable GC candidates that are likely to enable a collision-free insert trajectory. We use this ranked list of candidates for co-optimizing the trajectory and gripper abstraction. Once the trajectory and the GC are found, a straightforward modification of classic topology optimization algorithms can be used for computing the gripper geometry.

We evaluate our method over an experimental dataset of 23 examples, containing both representative samples from standard grasping datasets as well as a set of challenge models that are difficult to pick up. Our method finds solutions for all of these examples (see Figure A.1). We evaluate the virtual-to-real gap by running real physical experiments in *all* 23 results. We are able to pick up all but two models whose 3D representation fundamentally differed from the real shape. The vast majority of models have high grasp reliability and a large range of stability, but for one we generated a solution with marginal stability.

A.3 Related Work

Robotic Co-design Robot design involves specifying both geometry and actuation sequences. Traditional methods start with general-purpose geometry and then customize the actuation. This is useful given the cost of manufacturing and the relative ease of reprogramming. However, the revolution in digital fabrication and the resulting ease of customization has opened a new era of task-specific robot design. A body of recent work has shown the advantages of jointly optimizing a robot's shape and actuation for a variety of tasks such as ground locomotion [53,68,115,168,203], flying [55], swimming [116], and grasping [32, 49, 72, 136, 194]. Our work builds on this new trend, but instead of customizing a whole robot, we propose to enhance a general-purpose robot with customized end-effectors that can be rapidly fabricated, lowering the cost of customization.

Generative Gripper Design Past work on generative gripper design has focused on active grippers. Antipodal grasping was an early target for computational design efforts [22, 187], with researchers developing shaped fingertips for antipodal grasping using direct formulaic approaches [22,77,78,157,187] and neural network techniques [67]. Vacuum-based gripper design is another direction. The user specifies target locations, and then a 3D printable manifold and superstructure are generated for a specific object [74,170]. Our work extends these ideas to passive grippers.

Passive Grippers In literature, many grippers were classified as passive only because they passively conform to an object (as in the case of compliant [44] and soft robotics [158]). Some so-called passive grippers rely on actuators to release a grasp [131,137,158,200]. Truly passive grippers have zero degrees of freedom and have no reliance on actuators.The most widely deployed passive grippers in industry are forklifts, but they can only be used on objects specifically designed for them, e.g., pallets, shipping containers, and FIBC bags. The passive grippers proposed by [127, 128] use a rotational motion to engage an antipodal grasp, but they can only pick up extruded cross sections (e.g., a cylinder), the key category not covered by our method. Other work has focused on passive deformations around objects to apply antipodal forces [21, 66].

We stress that Table A.1 highlights *characteristics* of objects, not a strict classification. By covering a larger number of characteristics, we significantly expand the space of objects that can be passively grasped. For example, the bottom row of Figure A.1 shows an object that is graspable outside its CoM and is antipodal resistant and therefore can not be grasped by prior work.

Table A.1 summarizes the object shape restrictions posed by different types of grippers. The forklifts can pick up objects around their center of mass (CoM) and through internal pickup (e.g., holes and handles). Active parallel jaw grippers or other passive grippers that generate antipodal grasps work well on a variety of objects because they can create opposing forces anywhere and do not rely on gravity at the CoM for the opposing force. However,

Table A.1: Comparisons of different grippers on types of objects they are able to pick up.

	Internal Pickup	Antipodal Resistant	Grips Outside CoM	Extruded Cross Section
Ours	✓	✓	✓	
Non-Actuated Fork Lift	✓			
Mucchiani et al. 2018/2021			✓	✓
Antipodal (active or passive)			✓	✓
Antipodal (active) + Custom fingertips		✓	✓	✓
Vacuum-based (active)		✓	✓	✓

they suffer from picking up objects via internal structures and objects that are antipodal resistant. For example, the bottom row of Fig. A.1 shows an object that is graspable outside its CoM and is antipodal resistant. Parallel jaw grippers with custom fingertips may be able to pick up the antipodal resistant part due to their large conformable gripping area. Vacuum-based gripper can pick up a wide variety of objects with large enough flat surface. We stress that Table A.1 highlights *characteristics* of objects, not a strict classification. By covering a larger number of characteristics, our work significantly expand the space of objects that can be passively grasped.

Grasping All grippers require a grasp planning step and numerous methods have been applied to solving the problem. A fundamental metric for evaluating a grasp is force closure. A grasp is force closed if it can resist any arbitrary set of forces and torques [14, 24]. A grasp can be partially force closed if it resists all but a subset of forces and torques [101]. An alternative is to evaluate the caging of an object kinematically, in which an array of obstacles is placed around an object to limit the range of motion of the object [149,161]. The downside is that one cannot be sure where the object is relative to the robot when grasped, therefore

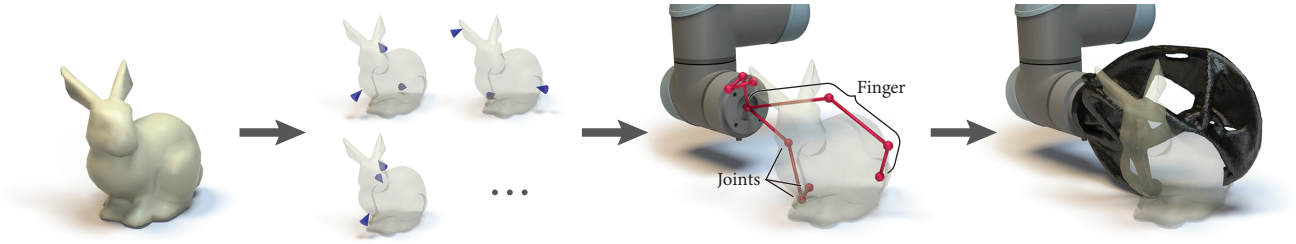

(a) Input Mesh (b) GC Generation (c) Input Trajectory Optimization (d) Topology Optimization

Figure A.2: Steps of our algorithm: (a) Import the object's shape from a user provided file; (b) Generate multiple promising GC candidates (where the blue cones point to contact points); (c) Optimize gripper shape and trajectory by using a skeleton (shown in red) as the simplified gripper model; (d) Generate the final gripper shape (shown in black) using topology optimization.

we chose to focus on a grasp being force closed.

The challenge with physics-based methods for grasp point selection is the need to model noise. Deep learning techniques have been shown to generate robust grasp poses both in the constrained 2.5D bin picking setting [118] and even the full cluttered 6D grasp pose setting [119, 125, 129, 142, 159, 177]. An alternative is to learn visomotor policies directly from raw visual data [104, 130, 143]. While learning methods successfully generate grasp candidates, they are trained primarily for antipodal and vacuum grippers and cannot be directly applied to passive grippers.

A.4 Overview

Our algorithm takes an object's geometry and positioning, along with a robot's kinematic structure as input, and generates (1) a passive gripper geometry that can be 3D printed and (2) a collision-free insert trajectory for creating a stable grasp.

Our algorithm involves three steps, as illustrated in Figure A.2. First, we generate a ranked list of GC (grasp configuration) candidates. We define a GC as three contact points on the object. We choose three contact points since this is the minimum number of points

that constrain a rigid motion. Next, we search for a collision-free trajectory for a given GC. The trajectory search is done by jointly optimizing the trajectory and a gripper abstraction. Finally, given the GC and the insert trajectory, we optimize the gripper shape to minimize compliance and weight using topology optimization.

As discussed, GC selection is uniquely responsible for final stability. However, it also impacts the likelihood for finding a valid insert trajectory in the second step and the possible trade-offs between compliance and weight in the third step. We consider four metrics: (1) a binary metric that validates static stability under gravity; (2) a measurement of robustness– the minimum disturbance force and torque that make the object unstable; (3) a heuristic to identify GCs that are unlikely to have a valid insert trajectory; and (4) an estimate of the final gripper weight. We use (1) and (3) to prune randomly sampled GCs and use (2) and (4) to rank the remaining GCs.

The next step is to optimize the insert trajectory to avoid collisions with the object. We consider one GC from the ranked list at a time and proceed to the next best GC if we fail to find the trajectory. Collision avoidance depends on both the trajectory and the gripper's overall shape, making it the most challenging objective. We first simplify the problem by ignoring the structural cost. We observe that the geometric aspect that affects collision is how the contact points are connected to the FFO and how the connecting structure moves through time. We propose to represent the gripper geometry using a *skeleton* (See Fig. A.2c.), which is parameterized curves that connect the FFO to each grasp point. We then jointly optimize over the space of skeletons and trajectories by minimizing a cost function associated with collision. We also add a trajectory complexity regularization term to the cost function to reward a simpler trajectory which reduces the chance of collision, leaves more collision-free space to optimize gripper shape, and lowers the robot's energy consumption.

The final step is to compute the gripper geometry. While the skeleton could serve as a workable gripper, it is too fragile. An alternative is to compute the volumetric region that does not intersect with the target object during insert motion, and use this full *collision-free volume* as the gripper. However, this gripper is too heavy. We therefore propose to

use topology optimization to generate the final gripper geometry, simultaneously minimizing compliance and weight, while constraining the gripper to lie in the collision-free volume (See Fig. A.2d.).

A.5 GC Candidates Generation

Recall that a GC (grasp configuration) is a set of three contact points on the target object. We choose three because it is the minimum number of points that constrains a rigid body. More contact points will kinematically over-constrain the solution, make it harder to find a collision-free trajectory, and make the gripper more sensitive to the approach direction [16]. Our proposed strategy for generating this list of candidates involves three steps. First, we propose a method for sampling GCs. Our sampling scheme identifies points on the surface that do not make contact with the floor and that can be directly connected to the FFO without colliding with the object; sets of three identified points are selected uniformly at random. We then drop GCs that are not statically stable under gravity (Section A.5.1) and the ones that we identify as *unreachable*—i.e., candidates that are unlikely to have a collision-free gripper shape and grasp trajectory (Section A.5.2). Finally, we rank the remaining GCs to maximize the robustness to external disturbances once the object is grasped, while trading-off compliance and weight of the gripper shape by using another heuristic metric (Section A.5.3).

A.5.1 Static Stability Under Gravity

Each contact point makes a contribution to the object's stability by exerting forces onto the object at different angles and location. We assume Coulomb's model of friction that limits the angle with respect to the surface at which the forces can be exerted. For contact point i, $|\mathbf{f}_i^T| \leq \mu_i |\mathbf{f}_i^N|$ where $\mathbf{f}_i^T$ and $\mathbf{f}_i^N$ are the tangential and normal forces exerted, respectively; and μ_i is the coefficient of friction at that point. This constraint can be viewed as a cone and can be approximated using a polyhedral cone with q sides where the allowed force is the non-negative linear combination of the edges of the polyhedral cone, called basis. Let

$\mathbf{w}_{ij}$ be the wrench (force and torque) generated by j-th basis of the cone at point i. The contribution from the i-th contact point can be written as $\sum_{j=1}^{q} k_{ij}\mathbf{w}_{ij}$ where $k_{ij} \geq \mathbf{0}$.

We determine if the GC is stable using *partial force closure*, which specifies whether a grasp can withstand a particular external disturbance (in our case, gravity) [102]. Formally, the partial force checks if there exists $k_{ij} \geq 0$ such that $\sum_{i}^{3}\sum_{j}^{q} k_{ij}\mathbf{w}_{ij} = [\mathbf{g}\ \mathbf{0}]^T$ where $\mathbf{g}$ is the unit vector of gravity. We say a GC is *stable* if it meets the partial force closure condition.

There is a slight problem with using this formulation of force contribution for passive grasping because the force of gravity does not directly cause top-facing contact points to generate forces, instead, the gripper only generates a contact force if there is a torque around the center of mass. To account for this, we set the frictional force generated by the top-facing contact points to zero and set those generated by the bottom-facing points depending on the angle with respect to the ground. Formally, we set $\mu_i = \max(0, \mathbf{n}_i \cdot \mathbf{g})\mu$ where μ is the base coefficient of friction.

There is a stronger condition called *force closure* which specifies whether a grasp can withstand any external forces and torques [14,24]. However, this type of grasp which typically involves contact points on different sides of the object makes breaking contact more difficult. We observe that, by utilizing gravity, the object can still be held stable without a force closure grasp. Hence, the partial force closure condition is sufficient for our purpose.

There is a small drawback from using force closure related metrics. These metrics assume that the contact points can exert forces onto the object. However, since our gripper is passive, the contact points just counteract the gravity and cannot exert additional force. This is problematic when we evaluate a GC with top-facing contact points. The metric will overestimate the stability. therefor we set the F^n to be $|F^n| = \mu \max(0, \hat{n}_i \cdot g)$, where $\hat{n}_i$ is the unit surface normal at point i on the object, g is the force of gravity.

A.5.2 Identifying Unreachable GC

Given a GC, it is expensive to determine if a collision-free trajectory exists—it involves solving the co-optimization problem in Section A.6. Thus, we need a fast heuristic that

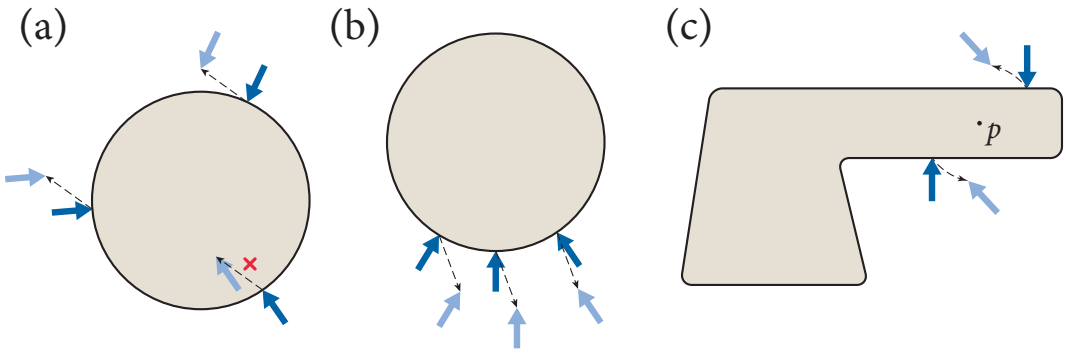

Figure A.3: Illustrations of the reachability heuristic. The dark blue arrows point to the contact points. The dashed black arrows show a candidate rigid motion to break all contact points simultaneously. (a) contact points cannot instantaneously break contact with the circle; (b) contact points can break the contact by translation; (c) contact points can leave the object by rotating counterclockwise around the point p.

identifies unreachable GCs. Our insight is to check if there exists an instantaneous motion where all contact points simultaneously break contact with the object.

We will motivate our heuristic in 2D for ease of illustration; these ideas extend naturally to 3D. Imagine grabbing a circle at three equally spaced locations in a 2D space (see Fig. A.3a.). It is trivial to see that there is no rigid motion to break all three contacts simultaneously without colliding with the circle, so we can drop it without running the expensive optimization. However, if the contact points are roughly on the same side (see Fig. A.3b.), then we can break the contacts just by moving the contact points away; hence, we keep this GC. One might be tempted to just check if the normals of each contact point are pointing in the same hemisphere. This is too strict. Consider grabbing the object in Fig. A.3c. The two contacts' normals are pointing in the opposite direction. However, this GC is reachable since we can rotate counterclockwise around the midpoint between the two contact points.

Our heuristic searches for an instantaneous rigid motion (translation and rotation) so that all contact points simultaneously sufficiently break contact with the object. We define the

instantaneous motion of the gripper as $(\vec{v}, \vec{\omega}, \vec{c})$, where $\vec{v}$ is the instantaneous translational velocity and $\vec{\omega}$ is the instantaneous angular velocity around the rotation center $\vec{c}$. We can derive the instantaneous velocity of a single contact point as $\vec{v}_i = \vec{v} + \vec{\omega} \times (\vec{c}_i - \vec{c})$ where $\vec{c}_i$ is position of the contact point. The contact point breaks contact if $\vec{v}_i \cdot \vec{n}_i \geq 0$ where $\vec{n}_i$ is the normal direction at the contact point. We also limit the angle between $\vec{v}_i$ and $\vec{n}_i$ to $\theta_{\max}$ to avoid nearly parallel motion to the surface. Formally, if there does not exists a motion $(\vec{v}, \vec{\omega}, \vec{c})$ such that $\vec{v}_i \cdot \vec{n}_i \geq \|\vec{v}_i\| \cos(\theta_{\max})$ for all i, then the GC is *unreachable*.

Inspired by the barrier method [61], we construct a loss function that penalizes motions that violate the constraints. We then solve the following minimization problem for a valid motion using a standard gradient-based optimization:

$$\min_{(\vec{v},\vec{\omega},\vec{c})} \sum_i \left[[\cos(\theta_{\max}) - \vec{v}_i \cdot \vec{n}_i]_+ + [\|\vec{v}_i\| - 1]_+ \right]$$

where $[\cdot]_+$ denotes $\max(0, \cdot)$.

Note that we do not normalize $\vec{v}_i$ to avoid numerical instability when the value approaches zero. The angle between two vectors will not exceed $\theta_{\max}$ because we also constrain $\|\vec{v}_i\| \leq 1$. A GC is said to be *unreachable* if the loss function does not converge to zero.

A.5.3 Ranking

The final step is to produce a ranked list of candidates for the next stage. We consider two metrics.

The first metric evaluates the minimum disturbance force that causes the object to become unstable. This metric measures how stable the grasp will be after the object is picked up and experiencing the transfer motion. Inspired by the well-known minimum wrench metric, we introduce a new metric called *partial minimum wrench*, which measures the minimum additional external wrench to violate the partial force closure condition. Intuitively, this metric corresponds to the maximum tilt angle and/or acceleration that an object held by this GC can experience before falling off. A higher partial minimum wrench is better.

The second metric is the estimated finger length. If the contact points are far from the FFO, the gripper will be cumbersome and the path to reach the point will be long. We therefore estimate the finger length by finding the shortest non-colliding path from the FFO to each contact point and taking the maximum path length. A shorter length is better.

Since the two metrics can be conflicting, our ranking scheme is inspired by the non-dominated sorting criteria in multi-objective optimization [48]. We segment the candidates into multiple Pareto frontiers, and sort them by the estimated finger length within each frontier.

A.6 Trajectory Optimization

In this stage, for each GC candidate, we want to search for an insert trajectory that avoids collision. Since collisions depend both on the gripper's shape and the trajectory, we need to design them together. The fundamental challenge in the co-design of a gripper and trajectory is the complexity of the search space. The nominal search space of the gripper geometry corresponds to the resolution of the voxel grid that a 3D printer can afford, and the search space of a trajectory can be described by the degrees of freedom of a robotic arm over time. We propose a novel reduced representation of the search space to make this search tractable.

A.6.1 Gripper Abstraction

We represent a gripper design as a *skeleton* which is comprised of three *fingers*, each with multiple *joints* connecting the FFO to the three contact points (Fig. A.2c). This representation stems from the weakest constraint that the grasping points need to be connected to the FFO. We use a skeleton of infinitesimal thickness to evaluate collisions over 2D curves as opposed to volumes; we account for manufacturability by expanding the mesh by an offset that corresponds to half of the printer resolution.

The insert trajectory is represented as a linear interpolation between a list of robot states in joint space. We call these robot states the *keyframes* of the trajectory. The first keyframe defines the robot when the gripper is outside of the object's proximity, and the last keyframe

defines the robot when making contacts with the target object.

We define the gripper skeleton as $\mathcal{G} \in \mathbb{R}^{3\times m\times 3}$ where m is the number of joints in each finger and define the trajectory as $\mathcal{T} \in \mathbb{R}^{n\times d}$ where n is the number of keyframes and d is the robot's degrees of freedom. Our goal is to optimize the tuple of the gripper skeleton and the trajectory: $(\mathcal{G}(\mathbf{x}), \mathcal{T}(\mathbf{x}))$ where $\mathbf{x} \in \mathbb{R}^N$ are the adjustable parameters, namely the intermediate joint positions for every finger, and intermediate trajectory keyframes, for a total of $N := 3 \cdot (m-2) \cdot 3 + d \cdot (n-2)$ parameters. In our implementation, we set $m = 4$, $n = 4$ and $d = 6$, resulting in 30 degrees of freedom in total. We denote $(\mathcal{G}(\mathbf{0}), \mathcal{T}(\mathbf{0}))$ as the initial guess from the initialization method described in Section A.6.2. We specify appropriate ranges $\sigma \in \mathbb{R}^N$ to each of the adjustable parameters (i.e. $-\sigma_i \leq \mathbf{x}_i \leq \sigma_i$) to ensure the search space is connected and the solution remains valid (e.g. the robot does not self intersect and the skeleton maintains its overall shape). In the following discussion, we omit $\mathbf{x}$ and hence write $\mathcal{G}$ and $\mathcal{T}$ to mean $\mathcal{G}(\mathbf{x})$ and $\mathcal{T}(\mathbf{x})$.

A.6.2 Co-Optimization of Trajectory and Gripper Skeleton

To co-optimize the trajectory and the gripper skeleton, we propose an objective function with four energy terms: gripper collision energy E_g, trajectory collision energy E_t, robot collision energy E_r, and the trajectory regularizer L. The first three terms focus on collision, while the regularizer penalizes complex trajectories.

The gripper collision energy is defined as the maximum collision at any point of the trajectory measured over the whole gripper skeleton. Similarly, the trajectory collision energy is defined as the maximum collision of a single point in the gripper measured over the whole trajectory. These two metrics are illustrated in Figure A.4. We note that, in theory, either one of these metrics can individually represent the collision error we target. In practice, however, we cannot directly compute them, but must instead evaluate them over a discretization of the trajectory and skeleton. Our insight for combining these metrics is that they describe the two basis directions for the surface, making the evaluation over a discretization robust to small features.

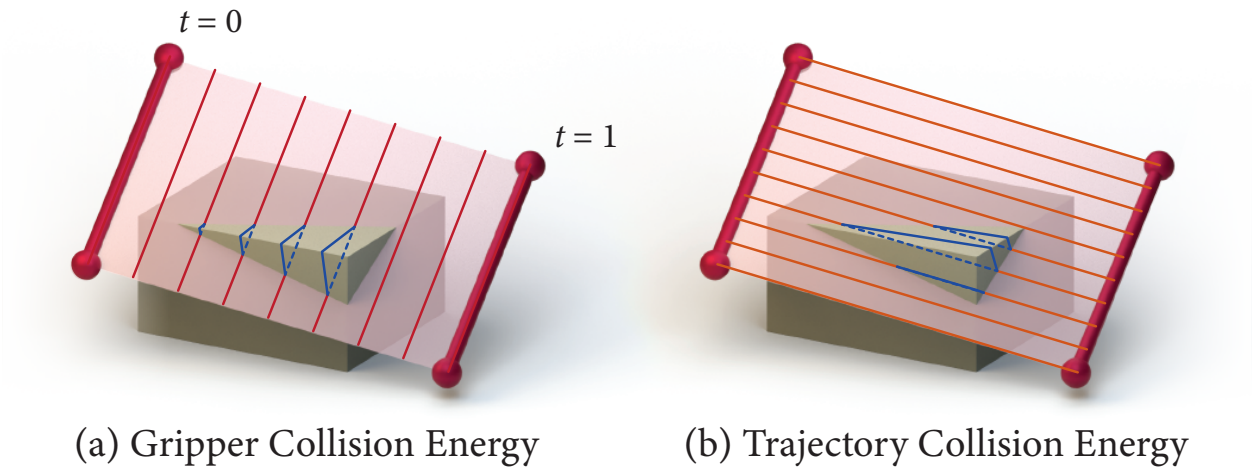

Figure A.4: Our collision energy measures the collision of the surface swept by the skeleton over trajectory shown in pink. We compute collision using path intersections along two directions: In (a), the path along the skeleton is tested at different time steps in the trajectory (shown by vertical red lines); In (b), the path along the trajectory is tested at different points on the skeleton (shown by horizontal orange lines). Collisions by the paths are shown in blue. Maximum collision of the paths in (a) defines the gripper collision energy, and likewise maximum of those in (b) defines the trajectory collision energy. Note: a simple box and a linear path is used for simplicity of the visualization.

Both metrics depend on a measurement of collision over a path: the collision of the skeleton at any point can be expressed as the sum of the collision of its fingers (piece-wise linear paths) and the collision of a point throughout the whole trajectory is measured from the path this point traces. We will describe our measurement of collision over a path later in this section.

Since the robot end-effector cannot go lower than a certain clearance height h, we introduce a robot collision energy term E_r which is the maximum penetration into the ground by FFO's position. We penalize the complexity of the trajectory with the L2 norm of the trajectory variations from the initial guess (i.e. the trajectory components in $\mathbf{x}$).

Our optimizer minimizes the following energy term:

$$\min_{\mathbf{x}} E_g(\mathcal{G}, \mathcal{T}) + E_t(\mathcal{G}, \mathcal{T}) + \lambda_1 E_r(\mathcal{T}) + \lambda_2 L(\mathcal{T})$$

where λ_1 and λ_2 are the significance of the robot collision energy and the trajectory regularizer. Since this objective is non-differentiable, we use controlled random search (CRS) with local mutation for minimizing this energy [92].

Collision Along a Path There are several approaches to compute the collision of a given path. One trivial approach is to use the length of the path that lies inside the object. We call this length the *inside distance*. However, this approach does not capture the degree of collision, as illustrated in Figure A.5. We propose to include a measurement of the shortest additional distance to make the path collision-free. We call it the *wrap-around distance* (See Fig. A.5). To measure the wrap-around distance, we compute the geodesic distance between a pair of points when the path enters and exits the object. We take the sum of the geodesics if the path enters and exits multiple times, and we do not include the geodesic if one or both endpoints are in the object. The collision of a path is defined as the sum of the inside and wrap-around distance (See Fig. A.6).

Discretization We compute E_g and E_t by sampling the trajectory and skeleton, respectively. We adaptively subdivide the trajectory so that the skeleton moves by at most some

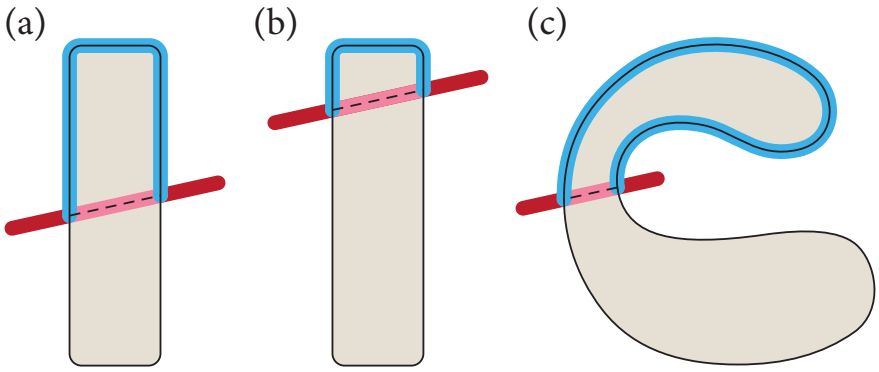

Figure A.5: Illustrations of the *inside distance* (pink) and *wrap-around distance* (cyan) of the skeleton (red) through some objects. The path in (b) is closer to a collision-free state than that in (a), but the inside distance is the same. The path in (c) has lower inside distance than (a) and (b), but it needs more work to reach a collision-free state.

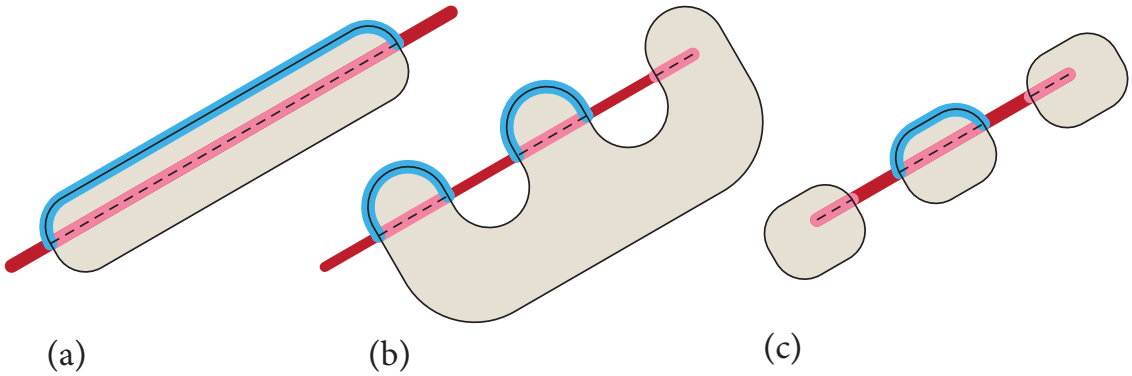

Figure A.6: The *wrap-around* distance is the sum of the geodesics (cyan) between every pair of entering and exiting intersections. The path in (a) has one such pair and in (b) has two. Some endpoints in (b) and (c) do not have a pair and therefore the geodesics are not defined.

distance d_{sub} and we adaptively subdivide the fingers by that same distance. This sampling is repeated for every iteration as lengths of individual segments can significantly change when adjustable parameters change.

To find where the path enters and exits the object, we use a raytracing algorithm to find intersections. Since the path for trajectory is not linear, we adaptively subdivide the path with some linearity tolerance d_{lin} into connected line segments.

To efficiently compute the geodesic distance between any given two points, we need to allow some accuracy trade-offs. We approximate the geodesic distance by running a standard shortest path algorithm on the vertices and edges of the triangle mesh. We use the isotropic remeshing algorithm to generate a new mesh whose edge lengths are as close to one another as possible. This makes the approximation more accurate. We precompute the shortest distance between every pair of vertices. The approximate geodesic distance for any given two points on the surface is computed as the distance of those two points to their closest vertices plus the precomputed geodesics between the two vertices.

Initialization We initialize the skeleton by computing the shortest, non-colliding curves that connect from the FFO to each contact point and then simplifying these curves to the right number of joints by discretizing the curves, expanding them by the surface normal, and removing vertices that does not contribute to collision avoidance. We initialize the trajectory to be a straight line towards the object.

A.7 Topology Optimization and Refinement

At our last step, we generate the gripper design by performing discrete topology optimization over the *collision-free* volume [9]. Since the trajectory is known, this volume can be computed as the complementary space of the swept volume of an object moving away from the gripper (See Fig. A.7). For the boundary conditions, we set the external forces to be the forces exerted by the contact points of the known GC along the normal directions and fix parts of the gripper around the FFO. In post-processing, we apply a smoothing kernel and run

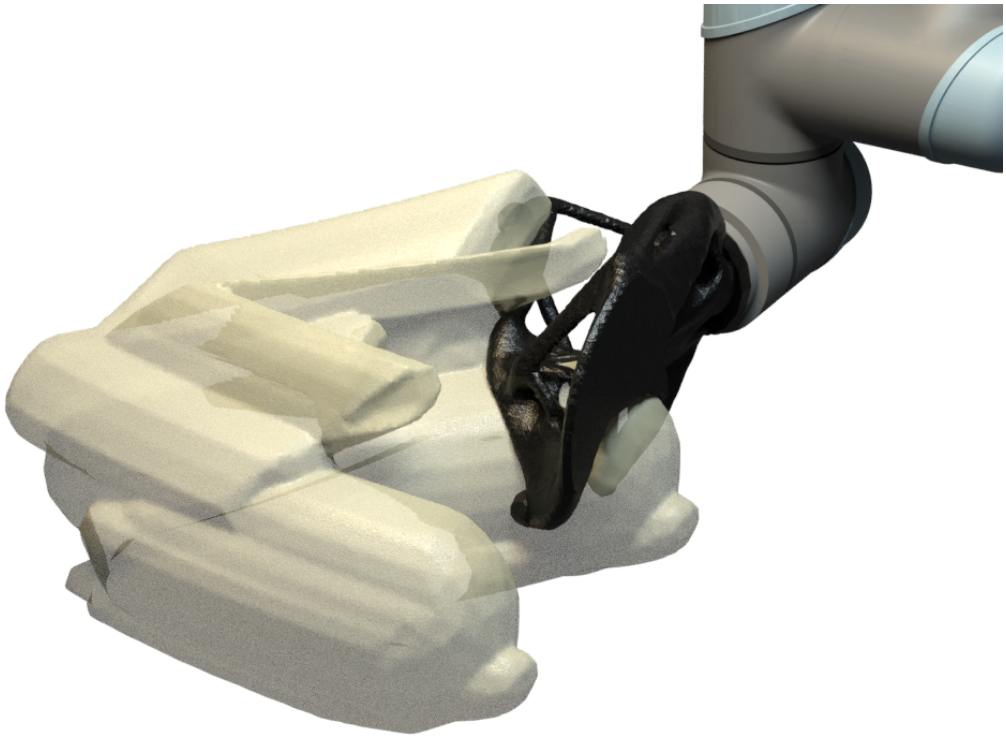

Figure A.7: In the robot's reference frame, the swept volume of the bunny (shown in white) is the space occupied by the bunny throughout the trajectory. The complementary space is the *collision-free* space for topology optimization. The topology optimized gripper is shown in black.

marching cubes to retrieve a smooth mesh. We further refine the gripper geometry by adding a small sphere at each contact point and subtracting the result with the swept volume to ensure an accurate geometry around the contact points. This increases the area of contact and improves the robustness of the grasp. Lastly, we add robot-specific mounting structures such as holes and a mounting plate for fast installation.

A.8 Results

We evaluate our algorithm on its success rate and demonstrate different designs fabricated in real. We refer the reader to the supplementary video for demonstrations of the grippers in motion.

A.8.1 Evaluation Set

We created a testing set of 22 objects (See Fig. A.8).

Five models are engineered to demonstrate the unique capabilities of the generated passive grippers. A1-A3 are designed to represent internal structures. A1 contains an L-shaped hole at the front. The pyramid (A2) contains a curved hole that requires a twist motion to insert. The *Top Key* (A3) contains a rectangular slot at the top and requires a quarter turn to insert. The pallet (A4) is designed to test if our algorithm can generate a fork-lift. The wedge (A5) is engineered to resist an antipodal grasp because of its tapered shape at all orientations. To the best of our knowledge, objects (A2) and (A5) cannot be passively picked up by any prior work.

In addition to our engineered models, we include a representative set from prior work. First, to uphold the SIGGRAPH tradition, we add the Stanford bunny (B) to our evaluation set. We choose some challenging objects (C1-C8) from the Fit2Form dataset [67] representing adversarial objects from Dex-Net 2.0 (C1,C2, C4,C6-8) [118] and objects from ShapeNet (C3, C5) [31]. We a pick a subset of YCB objects [29] that are feature-rich and contain no moving parts (D1-D8).

The input to our algorithm is the shape and its positioning. We run two experiments with (A1) using orthogonal positions: inserting from the front and from the side, resulting in a total of 23 experiments. We refer to them as *Front Key* (A1-f) and *Side Key* (A1-s).

Figure A.8: Evaluation set. A: engineered models; B: bunny; C: challenge models; D: samples from YCB dataset.

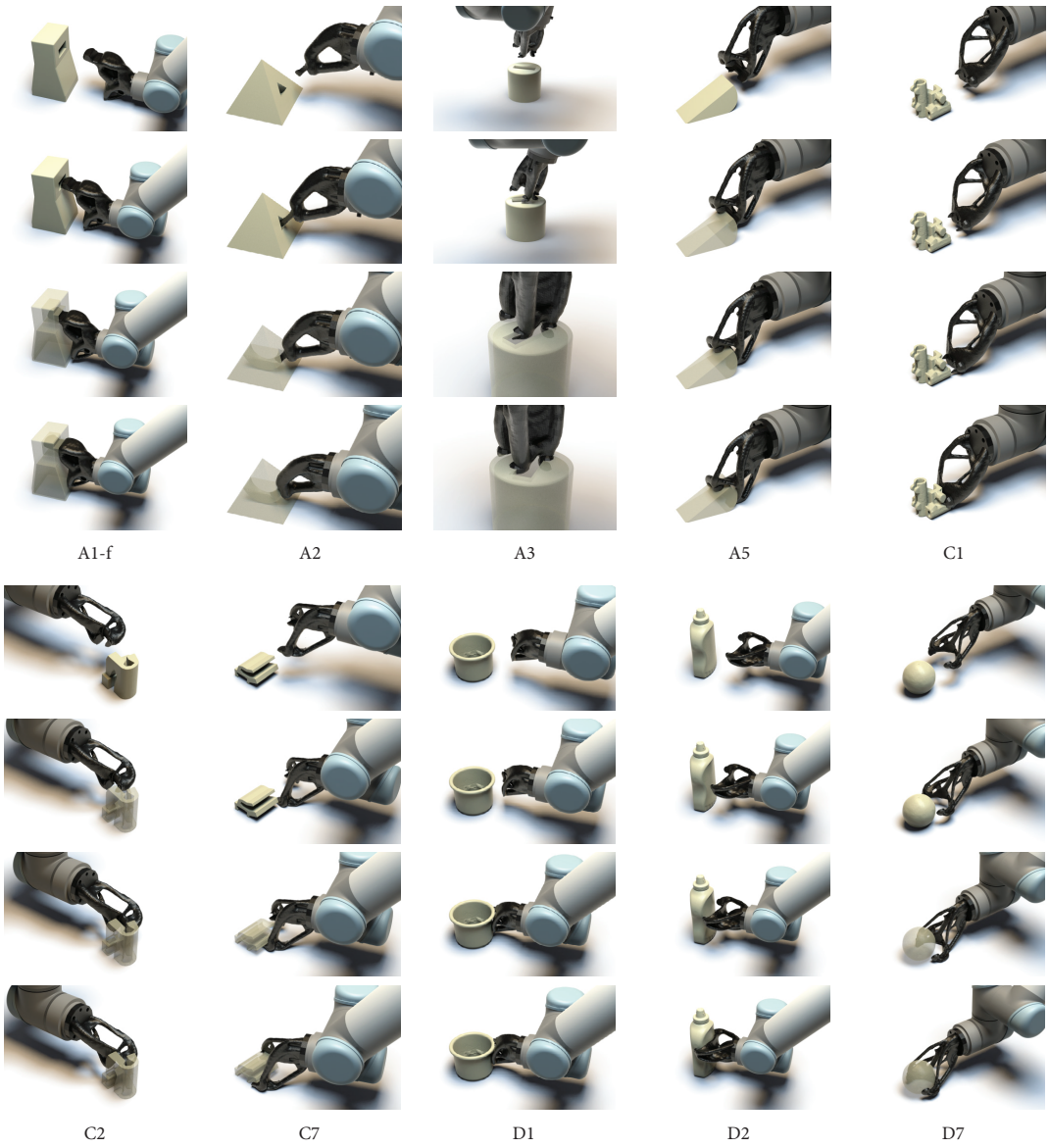

Figure A.9: Example grippers and their trajectories from objects in our dataset. Generated grippers and trajectories vary significantly across different models. These gripper designs mimic everyday mechanical tools such as wrenches (A5 and D1) and tongs (C7, D2, and D7), but are highly tailored to fit the objects. The accompanying trajectories can be classified into insert motions (A5, C2, and C7) and twist motions (A2, A3) and are nontrivial to design by hand.

A.8.2 Implementation and Experimental Setup

Our algorithm is implemented in C++, using libigl [84] and CGAL [179] for most mesh processing tasks. We use UR5 as our robot, which has six degrees of freedom. We use the code from [160] to calculate swept volume, and we use ToPy [81] to run topology optimization with the voxel size of 2 millimeters. We ran the algorithm on all 23 experiments on a cluster with 40 cores.

In our GC generation stage, we randomly sample 1,000 points on the mesh and generate 3,000 GCs. We assume the base coefficient of friction μ is 0.5 in modeling the contacts. For the reachability heuristic, we set $\theta_{\max}$ to 80°. In computing collision of a path, we set both the subdivision distance threshold (d_{sub}) and the linearity threshold of the trajectory (d_{lin}) to 1 millimeter. In computing the total objective function, we set the robot floor clearance (h), the robot energy significance (λ_1), and the regularizer significance (λ_2) to 0.05 meters, 1000, and 1e-6, respectively. In the optimization stage, we use NLopt's implementation of CRS for trajectory optimization [88] with the population size of 10,000 and relative tolerance of 1e-6. We allow the intermediate finger joints to vary within 1 centimeter, and we allow the six joints to deviate within $5°, 5°, 5°, 45°, 25°$, and 90°, respectively.

We set the robot grasping position (the last keyframe) so that the end effector is pointing forward and we place the object right in front of the end effector. This is true for all the models except for the Top Key (A3) which we point the end effector downwards. We ran the optimization stage until we were able to find three candidates that succeeded or until we ran out of grasp candidates, whichever happened first. We picked one candidate to fabricate and validate in the real world.

A.8.3 Algorithm Performance

The GC candidate generation step took less than a minute for each model. The trajectory generation took between 7 and 26 minutes, and 13 minutes on average per GC candidate per model. This step terminated after running on 5 GC candidates on average and succeeded on

at least one candidate on every model. The topology optimization took on average 1 hour and 26 minutes, but varied largely with the dimensions of the bounding box.

The whole pipeline takes on average 2 hours and 38 minutes per model, and on average 54% of the time is spent running topology optimization. While several computation steps could be sped up with straightforward implementation updates (for example, faster topology optimization [205]), our computation speed is on par with SOTA generative design systems and suitable for practical use, particularity when considering manufacturing time.

A.8.4 Qualitative Analysis

As illustrated in Figure A.9, the gripper shapes and trajectories are highly customized for each particular object. While many trajectories may seem obvious given a gripper, our algorithm can generate non-intuitive solutions. For example, it took one of the authors (who had seen all visualizations) almost two minutes to figure out how one of the grippers fits into its object. This highlights the tightly coupled nature of the problem and the need for co-optimization.

While all solutions are unique, we note that it is possible to classify gripper shapes into three categories. *Inserts* take most of the load in a single point, typically inside a cavity on the object, as is shown for examples A1-f, A2, A3, C1, and C2. *Tongs* rely on a wide separation of support from underneath, as shown in examples C7, D2, and D7. Finally *wrenches* have a narrow grasp from opposite sides that distributes the load on all three grasp points, as shown in A5 and D1. While customized to particular shapes, the designs replicate standard types of simple tools.

The trajectories most grippers follow also fall into a triadic grouping. Most objects fall into the *front insert* category where the gripper moves directly in and grabs the object from the bottom. Some examples include the front key (A1), the pallet (A4), the cup (D1), the orange (D7), and the challenge object C1. Although the trajectories may seem simple, they are not trivial to be designed by a user because they can be sensitive to approach angles and sequencing. For example, to get the orange, we need to go slightly down then insert to avoid

the convexity of the sphere, and to get the front key (A1), we need the right amount of in and up motion.

A number of designs fall into the *side insert* category where the required motion is to slide horizontally into the desired position. Some examples include our wedge (A5), our Side Key (A1-s), objects C2 and C7. Our algorithm is able to find the solution even if the required motion is not perfectly straight. In the bunny example, the robot needs to slightly turn to get around the convex part.

Our pyramid (A2) and *Top Key* (A3) fall in to the *twist insert* category. These objects are designed to only be grabbed by rotation motions which our algorithm is able to find.

Together, these results suggest that our algorithm is successful in understanding the affordances of each object. For example, object A1 is picked up with a front or side motion depending on the orientation of the cavity. Objects with bilateral symmetry are grasped on opposing sides, and objects with recesses have smooth insertion trajectories.

A.8.5 Physical Experimental Setup

We 3D print the grippers using two materials. We use a material with high coefficient of friction for the contact region (TangoBlackPlus) and a material with high stiffness and low cost for the rest of the griper (ABS). While these could be printed together in a multi-material printer, to reduce cost, we use the Stratasys J750 Digital Anatomy for the contact region and Stratasys FDM 3D Printers (Fortus 250mc, F120, F170) for the rest and assemble the two parts.

All objects and printed grippers were tested on the UR5 arm in moveJ mode with the trajectories specified by our algorithm. We tested object pick up as well as resistance to dropping once the object was correctly seated in the gripper. This involved rotating clockwise, counterclockwise, and a forward roll until the object fully fell out of the gripper and can be seen in Fig.A.10. For the *Top Key* we roll in the opposite direction due to joint limitations in the UR5 at this position. We repeat every test 10 times per object.

Table A.2: The number of successful pickups and maximum roll and pitch angles before the object falls out of the gripper with ten tests per category per object. For roll and pitch, the object was correctly loaded into the gripper to represent stability once an object was successfully picked up. Some objects (A3, C1, C3, C4, C6, D7) demonstrated multiple falling modes where an object could find additional regions of stability, resulting in large standard deviations.

Object	Pickups	CW (deg)		CCW (deg)		Fwd Tilt (deg)	
		mean	sd	mean	sd	mean	sd
A1-f	10	170	3	-162	6	68	9
A1-s	10	34	6	-23	7	30	4
A2	10	360	0	-360	0	53	23
A3	10	360	0	-359	3	-292	144
A4	10	237	3	-28	3	25	2
A5	10	52	6	-59	12	34	4
B	10	60	3	-194	1	145	3
C1	10	341	34	-246	41	118	15
C2	10	38	11	-238	5	276	10
C3	10	242	65	-189	5	83	3
C4	10	360	0	-332	59	316	72
C5	2	149	12	-14	4	9	2
C6	6	308	113	-358	4	28	69
C7	10	255	22	-66	5	34	9
D1	10	62	16	-107	44	68	16
D2	10	92	2	-101	2	26	5
D3	9	27	2	-21	4	19	5
D5	10	127	15	-59	3	14	2
D6	10	101	8	-89	4	69	33
D7	8	97	6	-178	102	40	7
D8	10	50	9	-104	10	30	2

Figure A.10: Post-grasp stability test for the bunny. We measure the maximum roll angle both CW and CCW (left) and forward tilt angle (right) before the bunny falls.

A.8.6 Real World Validation

Of the 23 experiments, 21 lead to successful pickups and the results are shown in Table A.2. 17 of these experiments had 100% success rate and only two had success rates below 80%. These results, and the following analysis of the failure cases, show that our method is able to successfully bridge the virtual-to-reality gap and displays high grasp reliability in real experiments. Visualization of these results are shown in Figure A.1 and our supplemental video.

The two failure cases (D4 and C8, not shown on the table) had significant discrepancies in their virtual representations. Since our gripper and trajectory were computed over the wrong input, the results were not well suited in practice. The 3D mesh we used to represent the bowl (D4) is thinner than the actual bowl, causing the gripper to collide during insertion. The challenge model (C8) was not oriented in its rest position causing inaccuracies during

stability analysis. We note that the two models that had 80-90% success rates had similar discrepancies, but those affected our gripper to a lesser extent because of symmetries in the models and the locations where the discrepancies happened.

The two models with marginal stability (C5 and C6) were examples from the adversarial dataset, which are notoriously challenging to grasp. These failed because the grasp locations we chose did not leave much room for misalignment. The grasp location must be robust to errors in the gripper fabrication (order of 0.5mm), the motion of the robot (order of 0.1mm) and human positioning the object (order of 0.5mm in the best case scenario). This uncertainty was not accounted for by our algorithm that evaluates the stability of a grasp configuration (Section A.5.1). We highlight, however, that our system was robust to these errors in all but these two adversarial examples, which shows the effectiveness of our approach.

A.8.7 Limitations and Future Work

The most evident direction for improvement is stability evaluation for selecting the grasp configurations. This would make our method more robust to errors in object placement and gripper trajectory encountered in real experiments. As discussed in Section A.3, the SOTA algorithms for evaluating the quality of a grasp configuration in active grippers use machine learning approaches, but these results cannot be directly applied for passive gripper design. The results in this work invites new avenues of research in this direction. Future work should also consider modeling external forces that may occur during pickup, for example when picking up an object from a bin.

On the algorithmic side, while the random sampling of GC candidates shows numerous successes, they may be sub-optimal in terms of robustness. Future work should employ a better sampling algorithm for maximal robustness and diversity. Further analysis on the collision avoidance objective should also be done to find the optimal trade-off between computational time and convergence as we vary the significance of each cost component and reduce the sampling resolution. In particular, we observed that dropping the trajectory col-

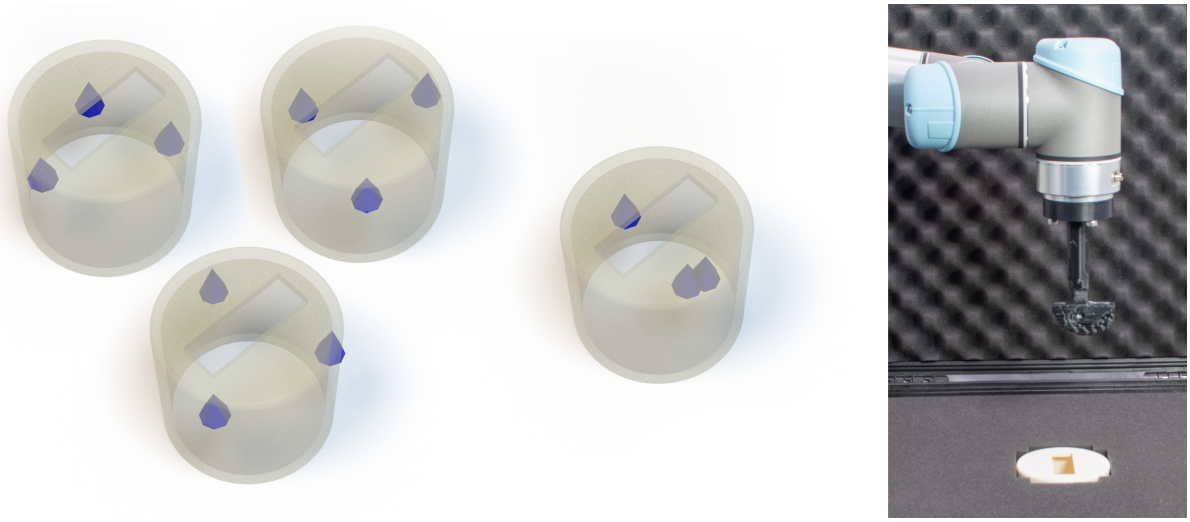

Figure A.11: While our algorithm is able to grasp A3 with wrench and twist motion (see Fig. A.9), it cannot find a solution with insert and twist motion. In this experiment, we restricted the contact point to lie inside the object, and the only GCs found (see examples on the left) have no feasible solution since the algorithm prioritizes stability without knowing the shape of the slot. Given a manually specified GC (middle), our algorithm is able to find the solution (see example that has been validated in reality with 100% reliability on the right). This example illustrates avenues of future work on GC and trajectory co-design.

lision energy and the wrap-around distance achieves better convergence when the trajectory samples are sufficiently high. However, adding these components to the cost function is important for convergence with sparse samples.

It would be interesting to investigate alternatives to jointly optimize the contact point selection and trajectory optimization which cannot be completely decoupled (see Fig. A.11). One other challenge is that the trajectory optimization can get stuck in a local minimum and not find a collision-free trajectory for a GC even if one exists. When this happens, the algorithm will choose a lower ranked GC. Additional freedom in object placement could also be achieved by optimizing robot's state in the grasping position.

Future work should also investigate different post-grasp trajectories. By assuming a vertical motion, we are unable to grasp objects with no bottom support such as a cylinder or a cone. Such objects can be handled by incorporating complex grasping strategies, such as rotating the object after being grasped [127, 128].

Finally, while we argue that customization for a single input has important practical applications, it would be interesting to relax some of the assumptions on our input. For example, we improve grasp reliability by considering random deviations of the object's position and geometry. Another interest direction for future work is to build on our optimization techniques to handle two or more input shapes or classes of shapes.

A.9 Conclusion

This work introduces a novel application for a generative design that has a high potential for impact in industrial applications of robotics. Robotic systems in industrial settings are highly inflexible—any change requires expensive re-design of autonomous components. The true cost of this rigidity has been particularly apparent during recent changes in demand during the COVID-19 crisis. Our algorithm addresses these challenges by establishing a new framework for creating robotic systems that can easily adapt to different scenarios without requiring additional dexterity, programming, or system complexity. Our key insight is that we can achieve this flexibility through re-design of passive grippers. We address the challenges of exploring the complex design space of passive grippers with novel insights on representation abstractions and co-design. We validate our findings with extensive physical experiments and discuss limitations, paving the way to exciting avenues of future work in this domain.

Appendix B

KINEMATIC MODELING OF HANDED SHEARING AUXETICS VIA PIECEWISE CONSTANT CURVATURE

B.1 Summary

Handed Shearing Auxetics (HSA) are a promising technique for making motor-driven, soft, continuum robots. Many potential applications from inspection tasks to solar tracking require accurate kinematic models to predict the position and orientation of these structures. Currently there are no models for HSA based continuum platforms. To address this gap we propose to adapt Piecewise Constant Curvature (PCC) Models using a length change coupling matrix. This models the interaction of HSA structures in a 2x2 array. The coupling matrix maps the change in motor angles to length changes and defines the configuration space in our modified PCC Model. We evaluate our model on a composite movement encompassing bending, extension and compression behavior. Our model achieves a positional accuracy with mean error of 5.5mm or 4.5% body length and standard deviation of 1.72mm. Further, we achieve an angular accuracy with mean error of -2.8° and standard deviation of 1.9°.

B.2 Introduction

The ability to orient robotic arms in space is critical to a wide range of applications. In inspection tools the ability to point cameras and other sensors ensure our critical infrastructure is well maintained and objects we purchase are fabricated properly. Satellite communication systems require accurate angular tracking to ensure connections are not lost [6] [1]. In energy systems it enables sun tracking for solar panels and solar thermal systems [126] [152]. All of these applications necessitate that they are resilient to contact with their environments

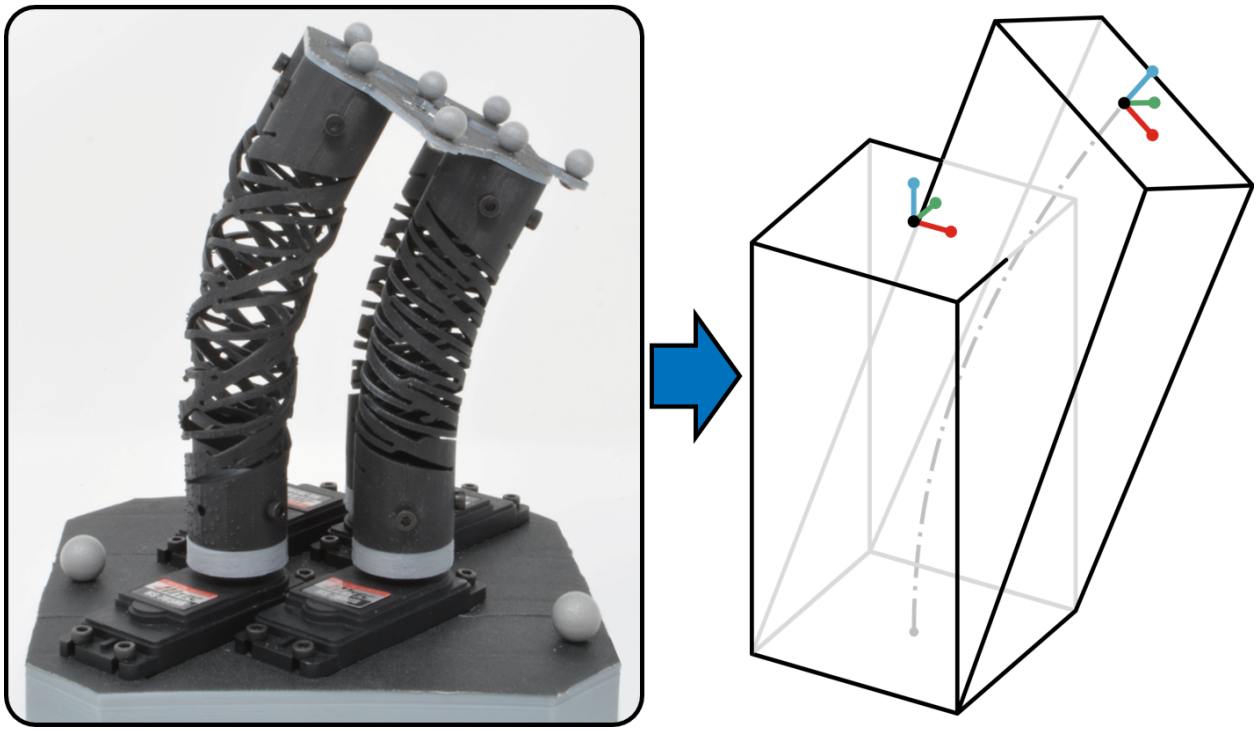

Figure B.1: Modeling a 2x2 HSA platform with Extended Piecewise Constant Curvature

which is a strength of soft robotics [138] [15] [154]. An electrically driven soft robot able to accurately point would be of broad utility.

Current research on electrically driven soft actuators has shown that handed shearing auxetics (HSAs) have proven very promising [112]. They are capable of linear expansion, and have distributed compliance like pneunets [124], but are driven by motor torques rather than fluid flows. Recent research has focused on applying HSAs to gripping tasks [37] [38], sensorization [41] [40] and mechanical characterization [182], but there have been no proposed control methods that describe the actuation of HSAs.

We use a common design of two sets of opposite handed HSAs to form a 2x2 HSA platform [112] as seen in Fig.B.1. Its simple design makes it an ideal section for a soft robotic inspection arm, while its large platform area makes a single section ideal for used as a pointer for solar panels or communication equipment. Despite the simplicity and utility of the design, without a model it cannot be of use or properly controlled.

We therefore look to adapt the existing soft robotics literature on control and apply them to HSA systems in order to enable electric soft robotic pointing systems and future multi-segment arms. We look to a common soft robot modeling method, Piecewise Constant Curvature (PCC) [89] [147]. PCC models assume that arms can be modeled as composites of rods that bend at a programmable radius and length that rotate relative to each other. Typically this bending is induced by differential pressure on chambers [94]. Because HSAs are extensible and compliant, we needed to develop a constant curvature model that captures this behavior. Extensible PCC models capture the arc length changes of the segments as they are actuated.

Our work maps the actuation space to segment lengths and accounts for inter-segment coupling with 5 parameters in a coupling matrix. We demonstrate that the PCC is more predictive than simple kinematic models with and without coupling. We evaluate this model on a composite movement to combine bending, extension and compression of the HSAs. Our proposed model achieves a positional accuracy with mean error of 5.5mm or 4.5% body length and standard deviation of 1.72mm. For the orientation, we achieve an angular accuracy with

mean error of -2.8° and standard deviation of 1.9°.

In this paper we:

- Model the interactions between individual HSAs on a platform.
- Adapt the Piecewise Constant Curvature model to a HSA driven platform with 4 lengths.
- Validate the modified PCC model through experiments on a HSA platform.

B.3 Background and Related Work

Soft robots have been usually driven by variable length tendons and pneumatic actuation and more recently, electroactive polymers [165].Handed shearing auxetics (HSAs) are a new category of material that enables electric soft robots. HSAs couple auxetic expansion with shear as a result of their periodic links and joints structure [112]. Auxetic metamaterials normally have a symmetric point in their trajectory, enabling them to transition from one handedness to another. This symmetry is purposely broken in HSAs, resulting in a single chiral shear motion. In order to create a HSA of opposite handedness, a simple reflection of the periodic pattern is sufficient [182]. When tiled on a cylinder, the HSA patterns couple global shearing from twisting to expansion along the axis of rotation [36]. These structures are compliant by nature, allowing for spring like responses to impacts or other disturbances. Their responsiveness to twisting allows for them to form linear compliant actuators driven directly by motor torques when placed in pairs [112]. Most applications of HSAs have been in grippers, since they require no model to be able to grasp successfully [37] [38] [41] [40].

Modelling the motion of soft robots is challenging due to their inherent infinite degrees of freedom.Various research works have shown that finite element methods and other numerical techniques can be used to describe the behaviour [202] [57]. But their inability to provide a closed form solution limits their adoption. An alternate approach - piecewise constant curvature models have been found to be more effective in defining the behaviour, where the

robotic structure is broken into continuous segments with constant curvatures providing an easy way to model a system which is differentiable everywhere [95] [191]. PCC modelling includes two mappings - 1) From actuator space to the configuration space (s,κ,ϕ) which describes the curvature produced by the continuum robot and 2) from configuration space to pose which defines the position and orientation of the end-effector.

The first mapping is unique to the type of robotic system such as pneumatic or tendon actuated arms [144] [174]. The second mapping is a standard kinematic transformation from the arc parameters to the coordinate system of the task space. This transformation can be achieved through different conventions and definitions [69]. One of those techniques uses the modified Denavit-Hartenberg (D-H) approach to define a transformation matrix that maps the configuration space to the task space.In this modified D-H method, the continuum robot is defined as a virtual rigid-link robot allowing for convenient closed form calculations [89].

At first glance, one might be inclined to use a parallel manipulator model for the kinematics of HSA based robotic section, since both HSAs and Stewart platforms rely on a change of length [47]. However, unlike links in a Stewart platform HSAs are always perpendicular to their base. This is most similar to traditional pneunet based structures which have been modeled using PCC [51].

B.4 HSA model and Platform Design

HSAs are not conventional linear actuators but do extend when the connected motor is activated. The extension of a single HSA is a function of the motor's angle of rotation θ. To establish mapping between angles and HSA length we conducted a force vs. displacement test using an Instron Universal Testing Machine at step angles of 30^o from 0^o to 180^o. We made our HSAs on a Carbon M1 out of FPU50 with a inner diameter of 22.98 mm and thickness of 2 mm. At each step we observed the length at which the force was zero. We observed that the extension is approximately linearly dependent on the angle, which is shown in Fig.B.5. As a result, the length of an actuator can be modeled as linear function of the

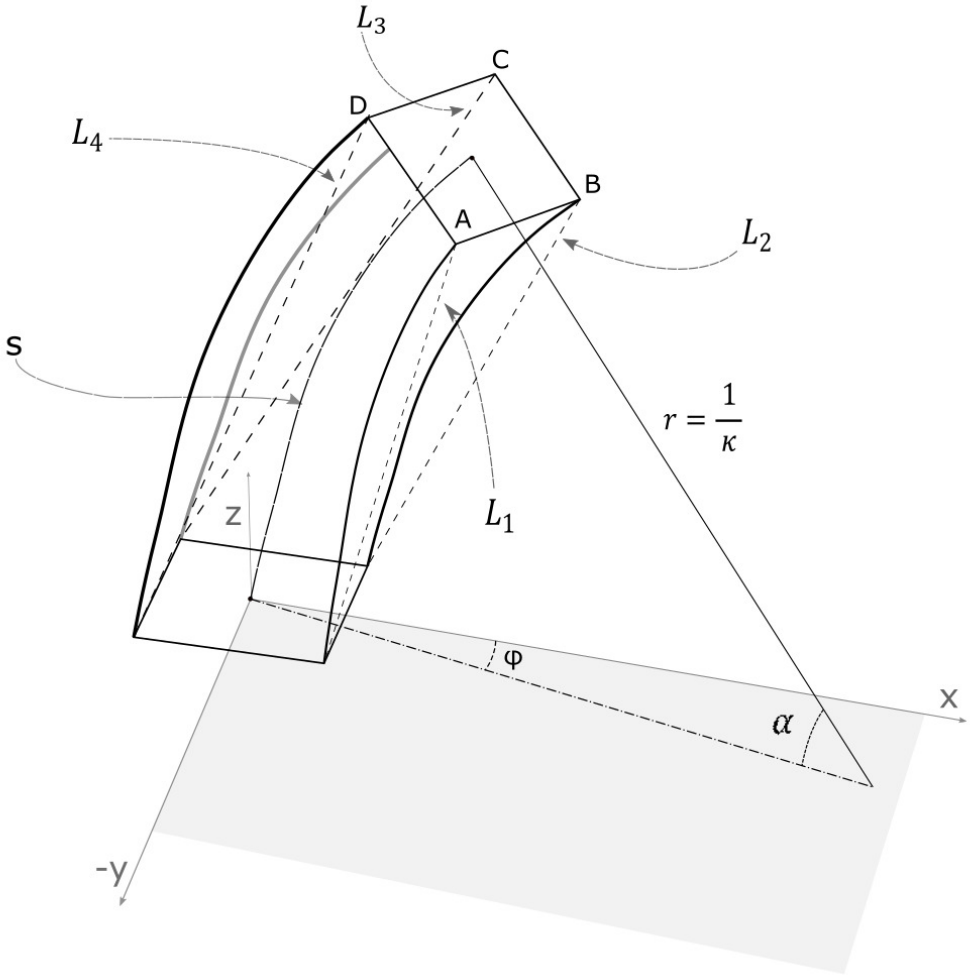

Figure B.2: Configuration parameters for the PCC model

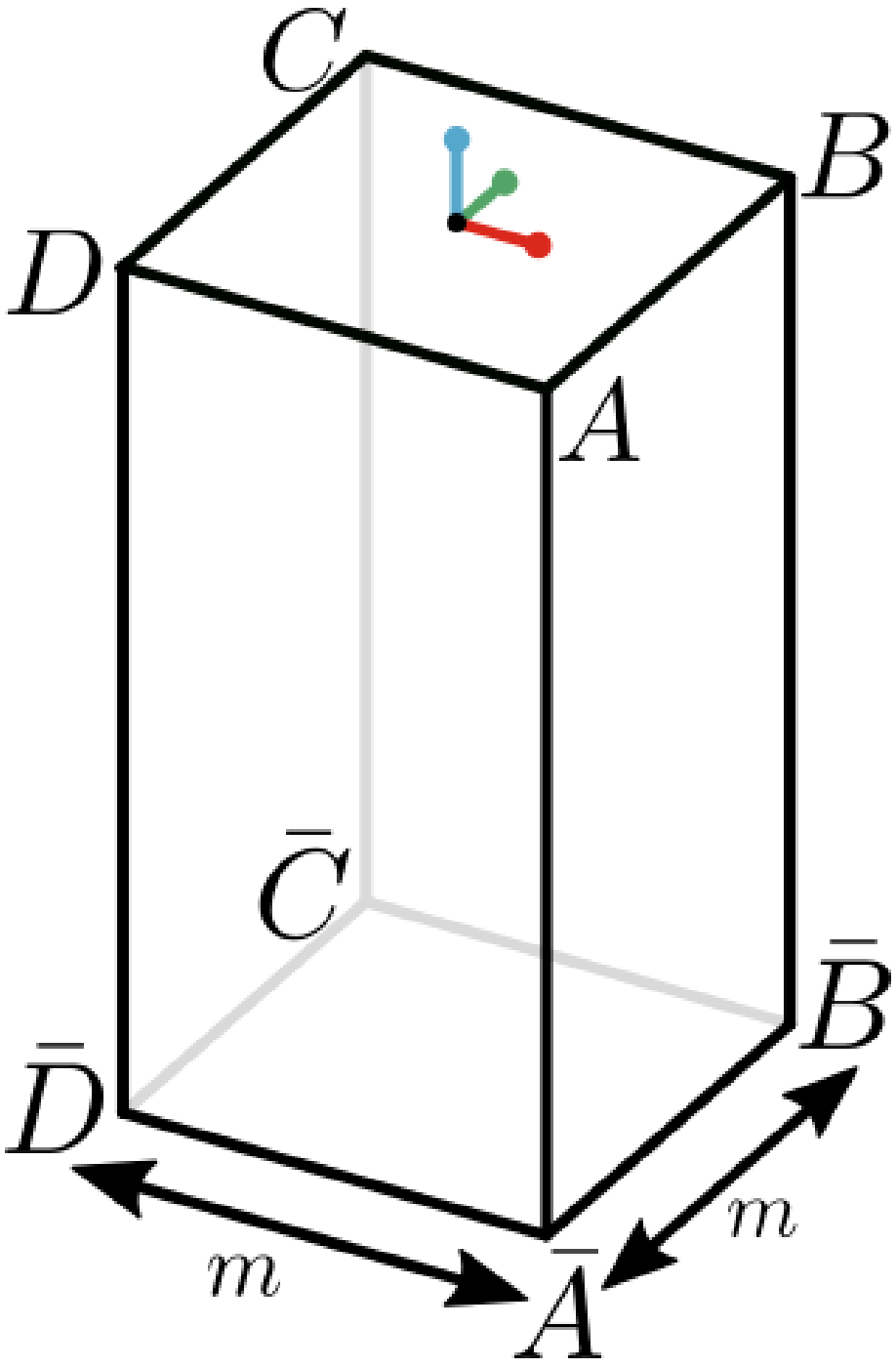

Figure B.3: Assembly at rest.

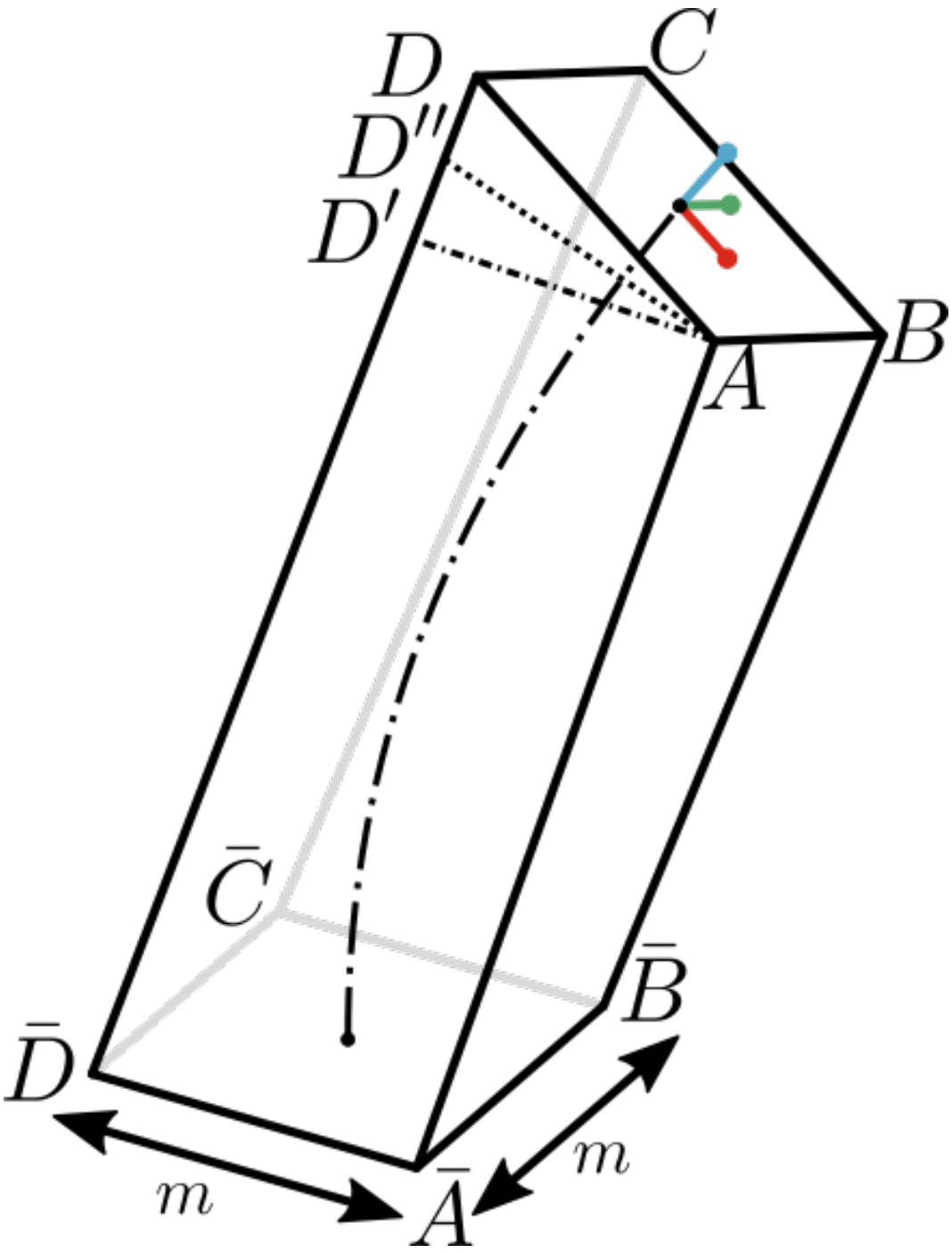

Figure B.4: Assembly after actuation.

angle of the servo motor. We found an equation of the form $L = \alpha_0 * \theta + \alpha_1$ with $\alpha_0 = 0.124$, $\alpha_1 = 0.119$ fit the data with an $R^2 = 0.99$.

B.4.1 The 2x2 Platform

A 2x2 HSA platform, as shown in Fig. B.6, was designed, 3D printed, and assembled. It has four independent HS-785HB servos in the base connected to to four vertical HSAs. The HSAs are attached together to a ridged platform on top. The servos are controlled via a Pololu Mini Maestro 12-Channel USB servo micro controller unit (MCU) and are powered with 6V and the system draws up to 3 watts during testing. The servos are mounted to the base in an angled pattern at 42°. This arrangement allows for a 43.68 mm center to center distance between HSAs. A key feature of the actuator assembly is the presence of opposite handed HSAs. In order to balance the net torque on the top platform produced from the independent rotation of each HSA, each handed pair of actuators are arranged diagonally in the 2x2 grid as shown in the top right corner of Fig.B.6. Thus, two of the servos rotate clockwise and two rotate counterclockwise to extend each HSA. Therefore there is no need for a strain constraint layer or a solid core in the structure. This allows the platform to change in length and extend in the Z direction in addition to bending. The resulting workspace of a single structure can be seen in Fig B.7.

B.5 Kinematic Models

B.5.1 Mapping θ to Length

In the 2x2 HSA platform, all the actuators are fixed in position at the base and coupled together with the top platform acting as a second common link between them. If HSA actuators were rigid length change actuators, the system would appear to be over constrained since only 3 heights relative to one plane are needed to define another. HSAs however are compliant, with the ability to compress and extend in response to external forces in addition to twist driven length changes. This means that the length of any of the actuators at any

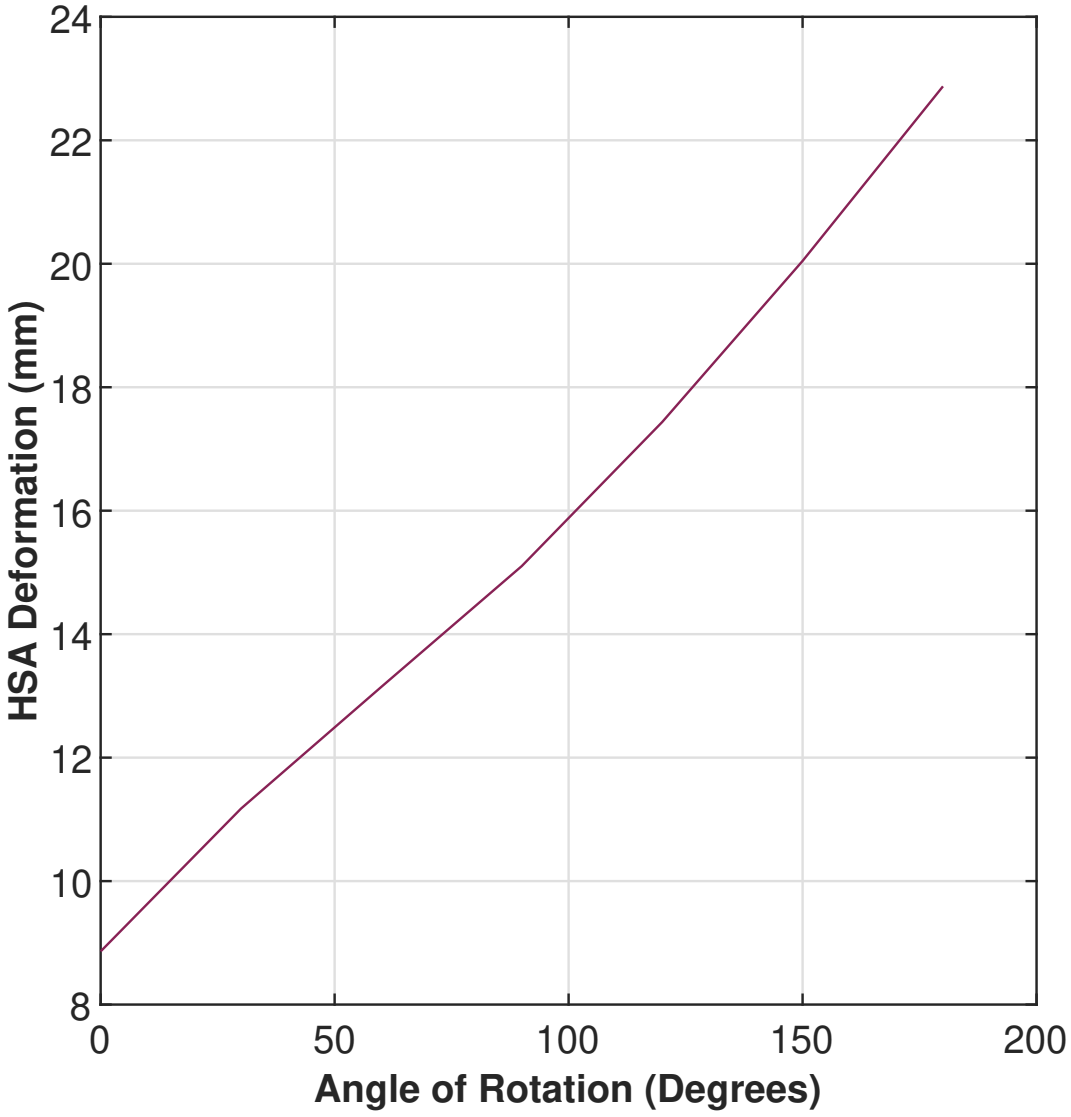

Figure B.5: Plot of HSA axial deformation against angular rotation with 5.2N applied force.

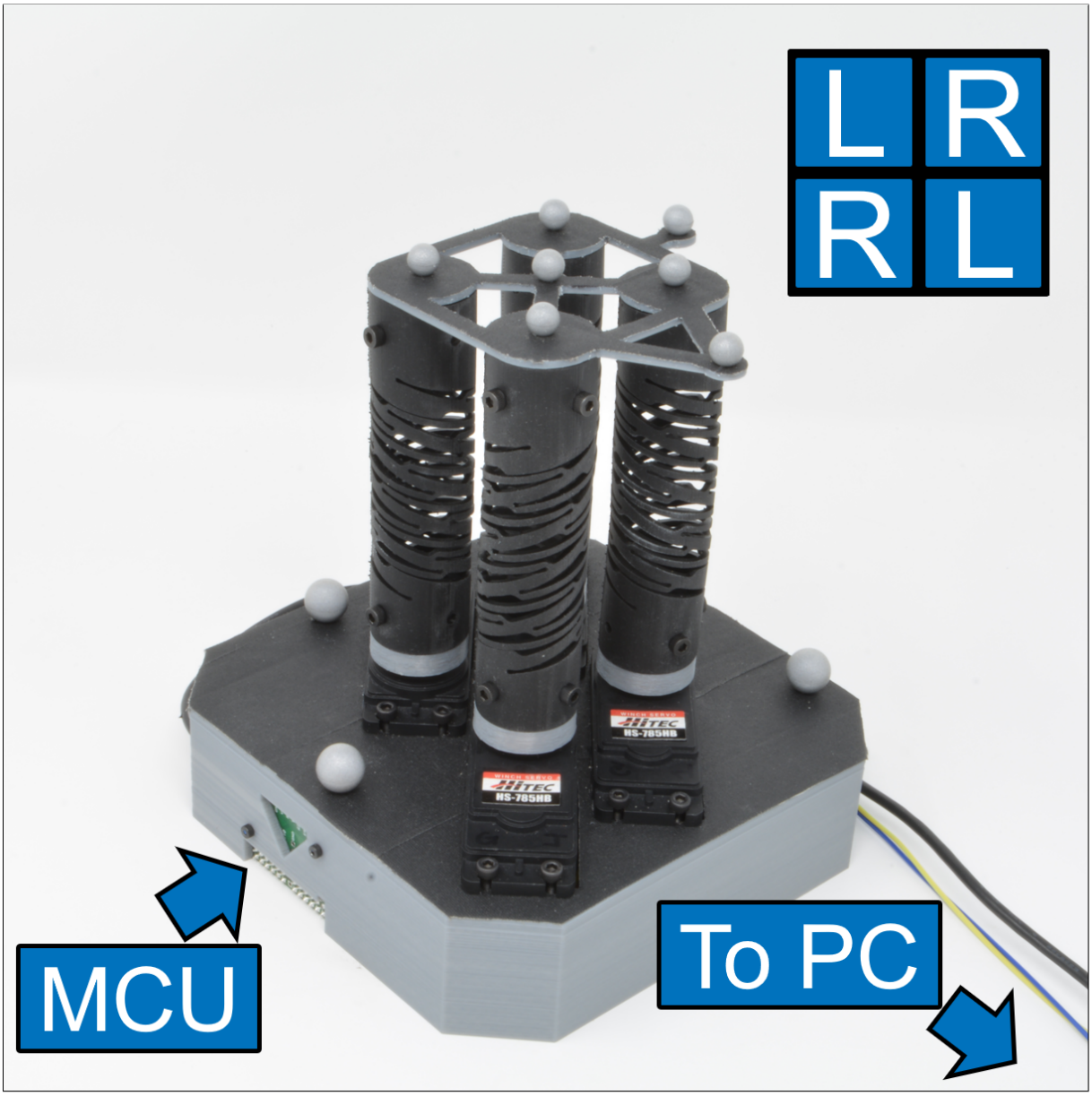

Figure B.6: The 2x2 HSA test platform. The top figure indicates the handedness of each HSA in the platform.

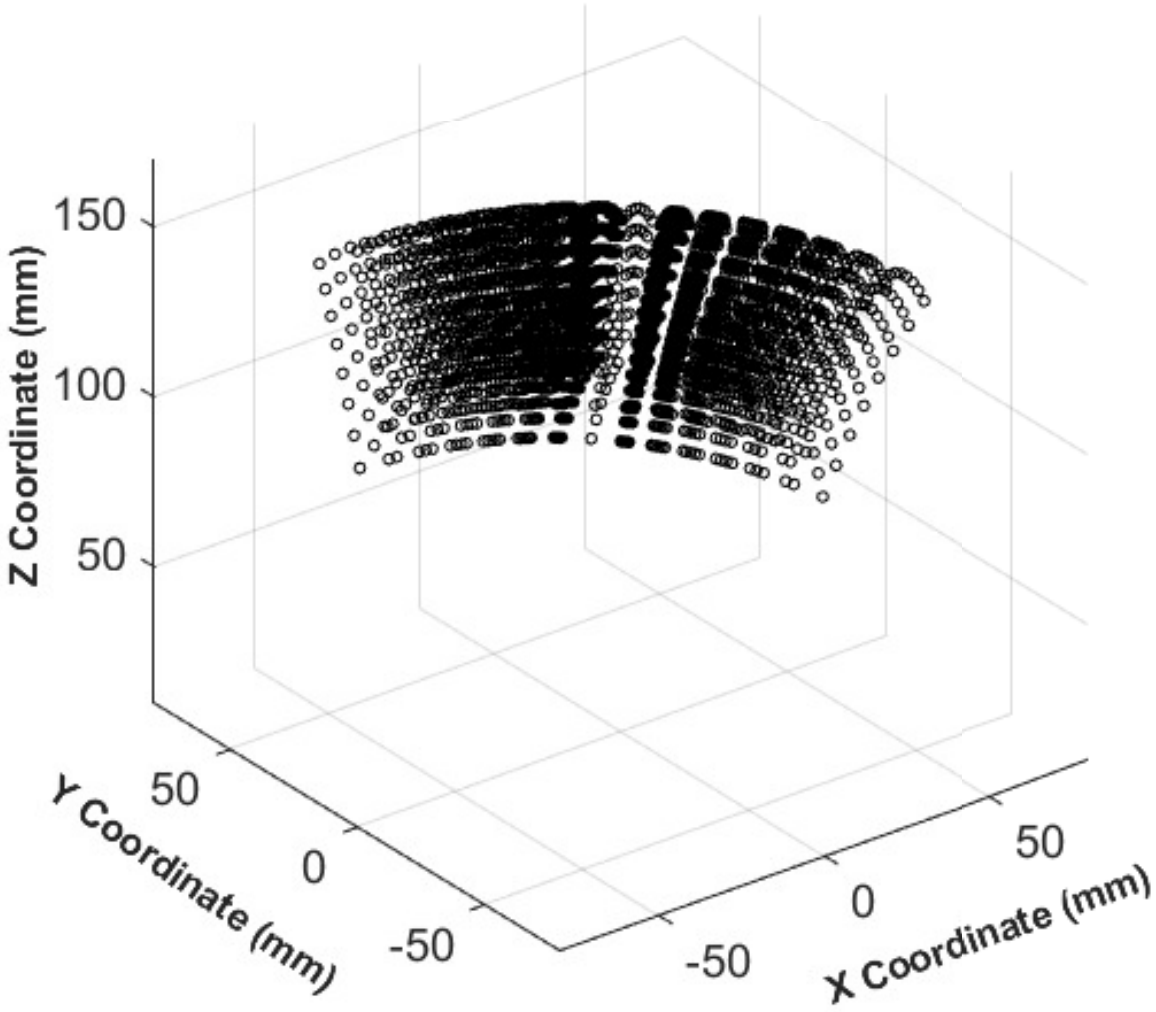

Figure B.7: Workspace of the HSA platform

time is dependent on length of other actuators (and by extension their theta states). We use our previous observation to model the length of actuators as linearly dependent on theta values of all actuators. If $\vec{L}$ represents the lengths of the actuators then we can write $\vec{L}$ as

$$\vec{L} = \bar{\beta_0} \cdot \vec{\theta} + \vec{\beta_1}.$$

The β_0 matrix establishes the extent of coupling between the actuators and $\vec{\theta}$ and β_1 vector establishes their height at rest. Consequently, any change in the dimensions of HSA would affect the coupling. For this reason we determine β_0 and β_1 for our chosen design through regression modelling.

Since, all the actuators in our experiment are similar in design, shape and geometry, we expect a symmetric matrix for a cross-linked system produced by them.The $\beta_{0,\text{regression}}$ matrix does not result in a perfectly symmetric matrix due to imperfections involved during system assembly and experimental set-up. To enforce symmetry we break the β_0 matrix up into two components, $\beta_{0,\text{symmetric}}$ and $\beta_{0,\text{deviation}}$ such that $\beta_{0,\text{symmetric}} + \beta_{0,\text{deviation}} = \beta_{0,\text{regression}}$. The $\beta_{0,\text{symmetric}}$ matrix is then found by taking the mean of the diagonals, making a circulant matrix. We then use $\beta_{0,\text{symmetric}}$ as β_0. Further, we average out the terms in β_1 to build a measure of the height of the actuators at rest.

B.5.2 Piecewise Constant Curvature approximation of HSAs

We choose the central point between all HSAs to be the distal end of our constant curvature rod as seen in Fig. B.4. From there, we define the origin to be the point between the bottom of all the HSAs. In order to model the HSA assembly we first establish the straight lines connecting the ends of the HSAs. Fig. B.3 shows the HSA assembly represented as two square, rigid bodies of the same dimension m, with corners $P = \{A, B, C, D\}$ and $\bar{P} = \{\bar{A}, \bar{B}, \bar{C}, \bar{D}\}$ called the "platform" and "base" respectively. We also initially constrain all points in P to lie in the same plane $\mathcal{P}$ and all points in $\bar{P}$ to lie in the plane $\mathcal{B}$. The platform and base are separated by the set of rigid links with lengths $L = \{L_1, L_2, L_3, L_4\} \equiv \{l_A, l_B, l_C, l_D\}$ where $l_J = \|\bar{J}J\|_2$ for $J \in P$ and have geometric centers. We note that due

to this geometry the distance l_S from the center of the platform to the origin i.e. the center of the base is given by:

$$l_S = \frac{l_A + l_C}{2} = \frac{l_B + l_D}{2} \tag{B.1}$$

$$\kappa_A = \frac{l_C - l_A}{d(l_A + l_C)} \tag{B.2}$$

$$\kappa_B = \frac{l_D - l_B}{d(l_B + l_D)} \kappa_C = \frac{l_A - l_C}{d(l_A + l_C)} = -\kappa_A \kappa_D = \frac{l_B - l_D}{d(l_B + l_D)} = -\kappa_B \tag{B.3}$$

Though we can calculate these lengths for each individual actuator, more significant is their arc length subtended during it's motion. Given the dependence of the platform's pose on angles and curvatures subtended by actuators, we follow the piecewise and extensible constant curvature approach to model the position and orientation as a function of their lengths.

B.5.3 Calculation of κ, ϕ, and s

To determine κ, ϕ, and s for our system, we extend the previous work on PCC models and determine the following relationships while referring to Figure B.2.

$$\kappa = \frac{1}{d} \sqrt{\frac{(l_C - l_A)^2}{(l_C + l_A)^2} + \frac{(l_D - l_B)^2}{(l_D + l_B)^2}} \tag{B.4}$$

The angle of rotation about the z-axis ϕ is derived as

$$\phi = tan^{-1} \left(\frac{l_B l_C - l_A l_D}{l_C l_D - l_A l_B} \right) \tag{B.5}$$

Finally the arc length s is proportional to the angle ϕ by the curvature κ,

$$s = \frac{2}{\kappa} sin^{-1} \left(\kappa \frac{l_S}{2} \right). \tag{B.6}$$

It is worth noting that

$$\lim_{\kappa \to 0} s(\kappa, l_S) = l_S$$
$$\lim_{\kappa_x \to 0^{\pm}} \phi(\kappa_y, \kappa_x) = \pm \frac{\pi}{2}$$

which are the cases for when the platform is in its rest position and when there is curvature only in the YZ plane respectively in this particular instance.

B.5.4 Calculation of position and orientation

With the center of the top platform represented in arc parameters (s, κ, ϕ), we use a D-H formulation for transformation to X ,Y, Z coordinates of the center of the top platform. We approach the forward kinematics from the base as a virtual revolute-revolute-prismatic (RRP) transformation as previously stated in [147]. This approach defines our transformation matrix shown in (B.7).

$$T = \begin{bmatrix} \cos\phi\cos\kappa s & -\sin\phi & \cos\phi\sin\kappa s & \frac{\cos\phi(1-\cos\kappa s)}{\kappa} \\ \sin\phi\cos\kappa s & \cos\phi & \sin\phi\sin\kappa s & \frac{\sin\phi(1-\cos\kappa s)}{\kappa} \\ -\sin\kappa s & 0 & \cos\kappa s & \frac{\sin\kappa s}{\kappa} \\ 0 & 0 & 0 & 1 \end{bmatrix} \tag{B.7}$$

The base coordinates of the system are defined in our system as -

$$B = [0; 0; 0; 1] \tag{B.8}$$

The position coordinates of the center point of the top platform would then be given by:

$$P = \begin{bmatrix} x \\ y \\ z \\ 1 \end{bmatrix} = T * B \tag{B.9}$$

Further, the orientation is defined by two angles:

$$\begin{bmatrix} \alpha \\ \phi \end{bmatrix} = \begin{bmatrix} s\kappa \\ tan^{-1}(\frac{l_B l_C - l_A l_D}{l_C l_D - l_A l_B}) \end{bmatrix} \tag{B.10}$$

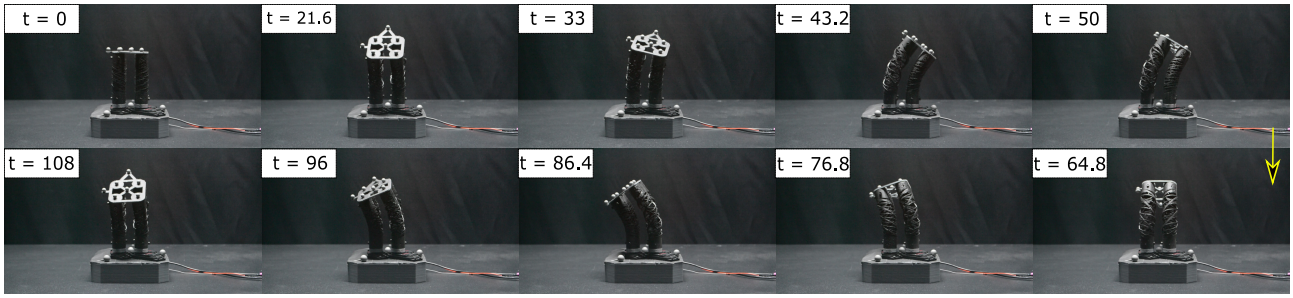

Figure B.8: Sequence of operations with the platform for experimental validation where each frame represents the state of the platform at time = t seconds.

B.6 Experimental Setup

Calibration is required to map between PWM values in Pololu's software to angular displacement on each individual servo for precise and accurate control. This was done by attaching an approximately 10 in rod to the end of each servo and rotating 90 degrees to determine a conversion between PWM values and servo's angle of rotation.An OptiTrack system made from four Flex 13 cameras was used to track changes in the 2x2 HSA platform. The four cameras were located in top corners of a 1 cubic meter test volume and pointed at the platform. Two rigid bodies were defined representing the dynamic top platform and the static bottom platform. 3D position and quaternion data were saved for each rigid body. We gathered all permutations on the HSAs from 0° to 180° in 30° increments. This resulted in 2401 unique states. These states were used to determine the coupling matrix β_0 and vector β_1.

For validation , we performed a composite rotation of the platform as shown in Fig B.8.This ensured that all the possible positions - extension, compression, bending &

rotation were combined within one single sweep. We performed this sweep for the full range of speeds the servos could generate (between 0.15 RPM and 30 RPM)

B.7 Results and Discussion

B.7.1 Mapping θ to length

The basis of our model is the mapping between inputs $\vec{\theta}$ and lengths. In section B.4 we found the linear relationship between θ and the length l of an HSA at which there is no more extensional force. As a first approximation, we use these results in an uncoupled linear model for estimating lengths of the actuators and observe significant errors against measured lengths from OptiTrack. The analysis for it is shown in Fig. B.9A where the average error in length estimation is 4.78mm with a standard deviation of 4.7mm and a range of -9 to 16mm. This was not unexpected as the above model considers the actuators as behaving independently within a coupled system but the 2x2 HSA platform acts as a common linkage between the four actuators producing a coupled model with interconnected links. This leads the naive model to over estimate the length of the segments and produces a wide range of errors.

By contrast when we integrate the two observations in our Coupled Length Estimation Model, as explained in the modeling section, we correct the bias and reduce the range and variance of the errors as seen in Figure B.9. The resulting error in actuator length prediction reduces to a mean of 0.25mm with a standard deviation of 1.6mm with a range of -4 to 6 mm. Since the errors in length propagate through the model we must examine the effects on predicting position and state through the trajectory.

In Figure B.11A we see the inputs to the sequence seen in Fig B.8. The lengths of the actuators predicted and measured are seen in Figure B.11C. As we can see, when the actuator is moving, we see the most agreement between the model and measurement. The greatest disagreement occurs when an actuator is meant to be held still. This is likely a result of an relationship not captured in the beta matrix. We suspect that the driving actuators, acting

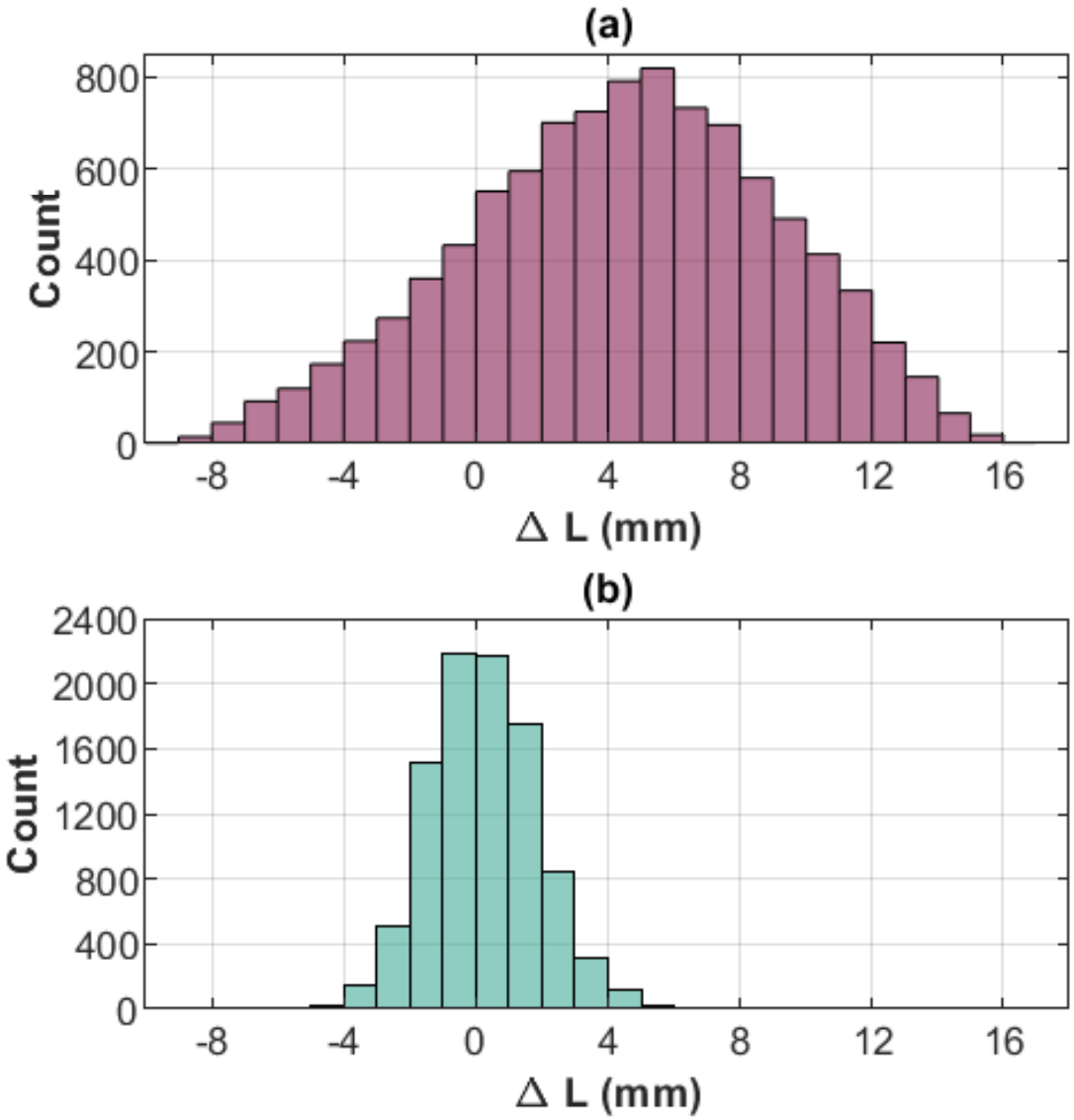

Figure B.9: (a) Error between the estimated and observed actuator length when using uncoupled mapping ; (b) Error between estimated and observed actuator length when using coupled mapping

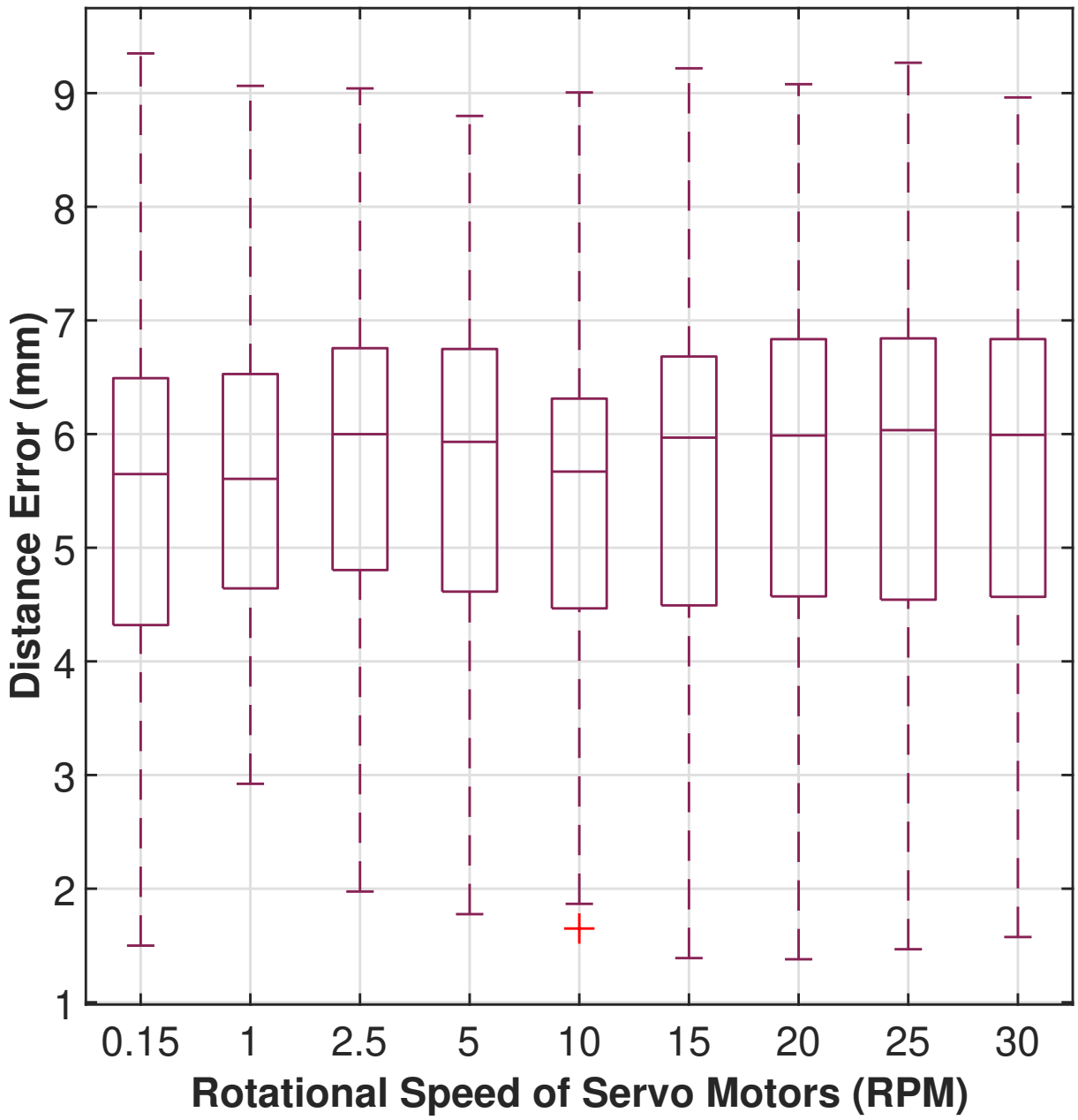

Figure B.10: Position error with change in velocity

as a force generator are compressing the held actuators, which then are pulled or pushed. An alternative explanation where the limits of extension are the source of errors is less likely to be true since L2 and L1 have large errors at their rest state.

B.7.2 Piecewise Constant Curvature Model

Figure B.11B and D show the error propagation through the model. We cannot observe the full state of the PCC section model, but we can observe the value of ϕ from the Optitrack data since its merely the angle between the plane that contains the center point and the Z axis, with the XZ plane. In Figure B.11D we see that ϕ is accurately captured by the model. The error of ϕ is between -3.4° and 3.7° with an average of -1.5°.

We can also observe α, the angle subtended by the arc section which is a combined metric of κ and s. α and ϕ encode the orientation of the platform. We observe that κ is well predicted from the kinematic model with a range of error between -5.85° and 0.2° and an average error of -2.8°. Therefore the model can reasonably capture the orientation of the platform.

We compare the Cartesian coordinate of the center point with the one predicted from the model in Figure B.11B. The result is a model which can predict the position with minimal error. When we repeat it's motion at various speeds as seen in Figure B.10 we see that for these motors, the model does not have an appreciable change in error. The figure shows the distribution of errors in the distance between the center of the platform observed and predicted. As the speed varies the mean error goes from a minimum of 5.5mm to a maximum of 5.7mm with no meaningful correlation with speed. Therefore we can conclude that for these motors and mass, the inertial effects can be ignored and a kinematic model such as ours is sufficient.

B.8 Conclusion and Future Work

In this paper we established that Piecewise Constant Curvature models (PCC) are good forward kinematic models for a 2x2 handed shearing auxetic platform when interaction be-

tween HSAs is modeled for a coupled system. This is the first model of HSA platforms and demonstrates that soft robotics modeling techniques can be adapted to HSA systems.In comparison with a naive approach, coupled model is found to be more accurate for predicting the lengths of the actuators. These can then be mapped into position and orientation of the HSA assembly's top platform. Over the complete range of Servo motor actuation, this model shows no degradation with increased speed.

Now that HSA platforms can be modeled they can be used more fully in robotic applications beyond gripping.We believe there is potential to further decrease the positional and angular error by expanding the interaction of HSAs in the coupled system as non-linear terms. Future work includes developing a dynamic model based on the kinematic model proposed in this paper and integrating it with a control framework for specific applications. Additionally, the platforms we have designed have only constituted a single link in the PCC framework. Extending this to a multi segment robotic arm made from HSAs is a logical next step.

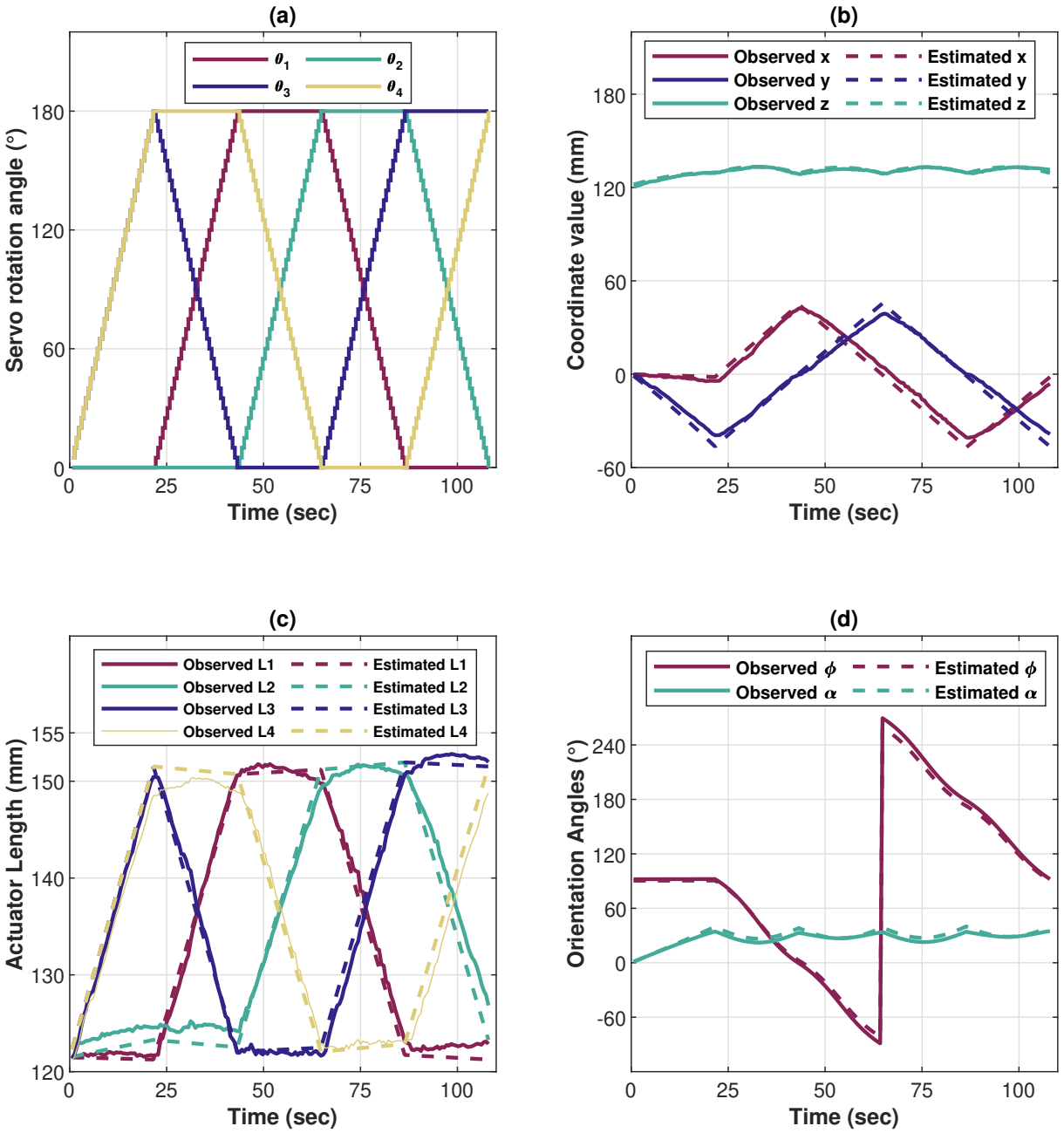

Figure B.11: (a) Shows the variation of servo motor angle(input) with time; (b) Shows comparison of Observed vs Estimated position of the center of the top platform; (c) Shows a comparison of Observed vs Estimated lengths of the actuators; (d) Shows a comparison of Observed vs Estimated orientation angles of the platform.